Doctorate Dissertation

博士論文

Precise Neutron Lifetime Measurement Using Pulsed Neutron Beams

(パルス中性子ビームを用いた中性子寿命の精密測定)

A Dissertation Submitted for Degree of Doctor of Philosophy
December 2018

平成30年12月博士（理学）申請

Department of Physics, Graduate School of Science,
The University of Tokyo

東京大学大学院理学系研究科物理学専攻

Naoki Nagakura

長倉　直樹

Abstract

The neutron beta-decay lifetime ($\sim$ 880 s) is an important parameter in the weak interaction of the Standard Model, cosmology, and astrophysics. For example, the neutron lifetime is a parameter which can be used to determine the $V_{\rm ud}$ parameter of the Cabibbo-Kobayashi-Maskawa quark mixing matrix. The neutron lifetime is also one of the input parameters for the Big Bang Nucleosynthesis, which predicts light element synthesis in the early universe.

The neutron lifetime has been previously measured by mainly two independent methods. One is to measure the number of protons from neutron beta-decay, and the other is to store ultra cold neutrons (UCNs) and count the number of remaining UCNs after a certain period of time. However, experimental measurements of the two methods are significantly different (4.0σ or 8.4 s). Therefore, we conduct a new type of experiment to resolve this problem. We set our eventual goal precision as 1 second on the neutron lifetime, which is comparable to the current best precision measurement.

The experiment is carried out at the polarized beam branch of beamline five, Materials and Life Science Experimental Facility, Japan Proton Accelerator Research Complex. The polarization beam branch enters a spin flip chopper (SFC), which is composed of radio-frequency coils and magnetic super mirrors. The magnetic super mirror can selectively reflect neutrons depending on the neutron polarization direction, which makes it possible to create a neutron bunch with arbitrary length.

A time projection chamber (TPC) made of polyether ether ketone was developed for a beta-decay counter to realize low background condition. Furthermore, the inside walls are completely covered by lithium fluoride plates to absorb scattered neutrons without prompt γ-ray emission. A small amount of ^{3}He gas, which typically amounts to 100 mPa pressure, is injected into the TPC. The neutron flux can be evaluated by counting the number of $^3\mathrm{He}(n,\ p)^3\mathrm{H}$ events in the TPC. Since the length of each neutron bunch is about half of the TPC length, the TPC can detect both the beta-decays and $^3\mathrm{He}(n,\ p)^3\mathrm{H}$ reactions with a 4π solid angle acceptance and the good signal-to-noise ratio.

The detector response was simulated using the Geant4-based Monte Carlo simulation software. The result is used to evaluate the signal selection efficiencies and expected background amount in the signal region. The full detector setup is implemented in the system. Using the simulation result, the difference of the signal selection efficiencies between beta-decay and $^3\mathrm{He}(n,\ p)^3\mathrm{H}$ was corrected. We started data acquisition in May 2014, and we have continuously taken the data every year by 2018. During the data acquisition, 6.0×10^{11} neutrons entered the TPC in total, and the all-combined data gives a statistical error of about a few seconds on the neutron lifetime. The analysis result for the data taken through March 2018 was $898.8 \pm 4.7\ (\mathrm{stat.})\ ^{+7.7}_{-8.9}\ (\mathrm{sys.})$ s. Several

upgrade plans to reduce both the statistical and systematic uncertainties are ongoing, such as SFC upgrade and low-pressure TPC operation.

Contents

List of Figures

List of Tables

Chapter 1

Introduction

A free neutron decays into a proton, an electron, and an anti-neutrino through the beta-decay process. The experiment to measure the neutron decay lifetime (τ_n) is conducted at Japan Proton Accelerator Research Complex (J-PARC). This chapter describes the research background and the motivation to precisely measure τ_n.

1.1 Physics motivation

Neutron beta-decay process can be described as the transformation of a d quark to a u quark. It is one of the fundamental processes in the weak interaction because of its simplicity. The experimental measurement of the decay lifetime has an crucial impact on particle physics, astrophysics, and cosmology. In this section, the physics motivation to measure τ_n is discussed.

1.1.1 Light element production in Big Bang Nucleosynthesis model

According to the Big Bang Nucleosynthesis (BBN) model, nucleosynthesis processes is known to have taken place between about 10 s and 20 min after the Big Bang. Light elements, such as hydrogen, helium, and lithium, were created during the BBN process. Elements heavier than lithium have not yet formed at this stage. There is currently good agreement between the observed and the theoretically calculated values of the light element abundance, which is one of the strong evidences supporting the Big Bang model. For example, the helium-to-proton ratio can be calculated using the baryon-to-photon ratio and the neutron lifetime. The predicted abundance agrees well with the observed value by Peimbert $et\ al.$ in 2016 as shown in Figure 1.1.

According to the BBN theory, time development of the light element composition after the Big Bang can be calculated as shown in Figure 1.2 [1]. From the perspective of nucleosynthesis, the time development of each stage in the early universe is described as below.

- $t <$1 s, $T \sim$ a few MeV
  The energies of nuclei were high and the proton and neutron ratio was maintained in a thermal equilibrium state as follows.
  $$p + e^{-} \leftrightarrow n + \nu_e, \tag{1.1}$$

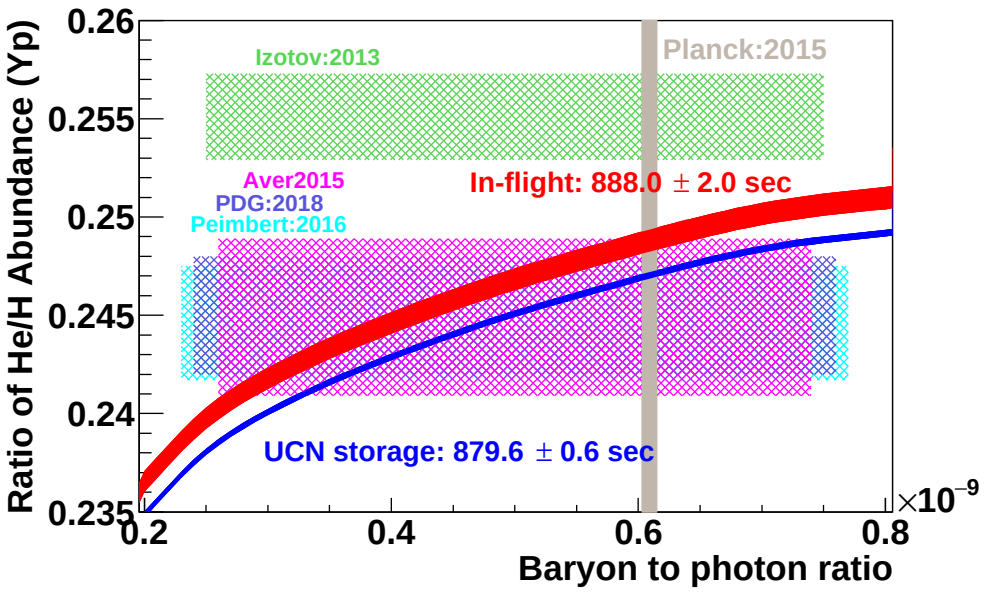

Figure 1.1: Baryon-to-photon ratio v.s. He/H abundance (Y_p) with in-flight and UCN lifetime results. Y_p result comes from Peimbert2016 [2], Aver2015 [3], and Izotov2014 [4]. Baryon-to-photon ratio was observed by Planck2015 [5]. The BBN prediction band shows one standard deviation uncertainty [6]. The two types of methods of τ_n measurement are described in Section 1.2.

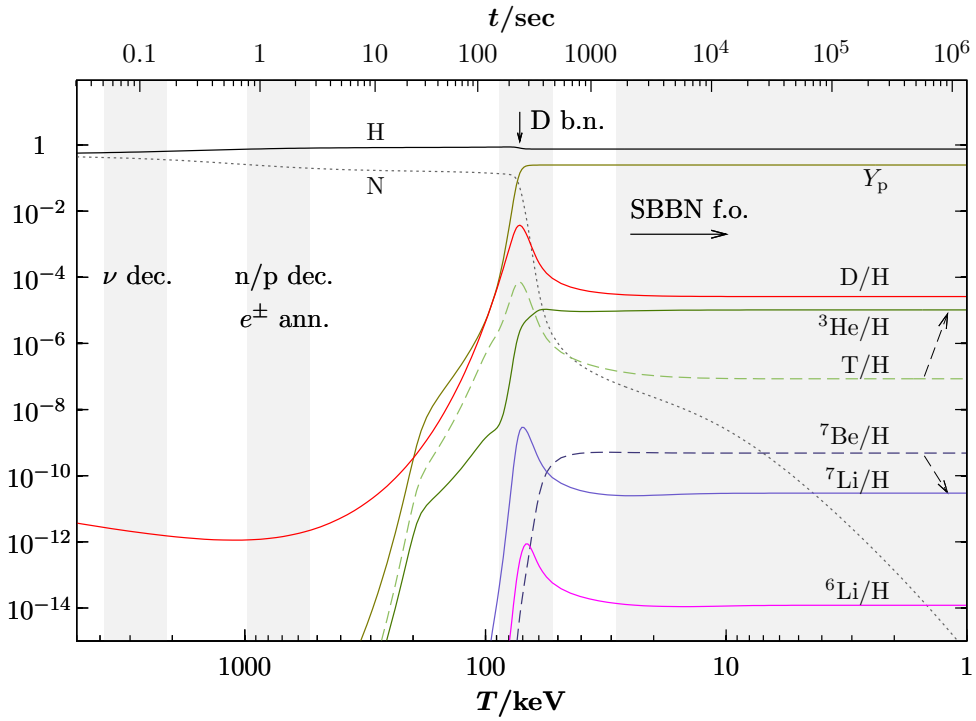

Figure 1.2: Abundance of light elements after the Big Bang according to the standard big bang nucleosynthesis by M. Pospelov and J. Pradler in 2010 [1]. The vertical axis represents the fraction of total mass.

$$p + \overline{\nu}_e \leftrightarrow n + e^+. \tag{1.2}$$

Protons and neutrons at this stage followed the Boltzmann probability distribution which can be expressed as

$$f(E) \sim \exp\left(-\frac{E-\mu}{k_B T}\right), \tag{1.3}$$

where E is the particle energy, μ is the chemical potential, k_B is the Boltzmann constant, and T is the temperature of the state. The chemical potentials of a proton and a neutron are cancelled out with each other. The ratio of the numbers of neutrons to protons (N_n/N_p) becomes

$$\frac{N_n}{N_p} \sim \exp\left(-\frac{m_n - m_p}{k_B T}\right) \sim 1, \tag{1.4}$$

where m_n and m_p represent the neutron and proton masses, respectively. Since the energy at this stage was still much higher than the mass difference between a neutron and a proton, their numbers were maintained to be almost the same.

- $t \sim$1 s, $T \sim$1 MeV
  The reactions of Eq. (1.1) and (1.2) ceased to occur. At this moment, the N_n/N_p ratio was fixed by the freeze-out temperature $T_{\rm fr} \sim 1$ MeV as follows.

$$\frac{N_n}{N_p} \sim \exp\left(-\frac{m_n - m_p}{k_B T_{\rm fr}}\right) \sim \frac{1}{6}. \tag{1.5}$$

- 1$< t <$100 s, 0.1 MeV$< T <$1 MeV
  During this stage, a fraction of the neutron decayed into a proton through the beta-decay process as expressed in Eq. (1.6), which was the only reaction to affect the N_n/N_p ratio. At the end of this stage, the ratio decreased to 1/7.

$$n \rightarrow p + e^- + \overline{\nu}_e. \tag{1.6}$$

- 100 s $< t <$1000 s, 0.05 MeV$< T <$0.1 MeV
  Protons and neutrons lost kinetic energies and were bound with each other to create deutrons or heavier nuclei based on the chain processes described in Figure 1.3. Since there exists no stable nuclei with mass numbers of 5 and 8, nuclei heavier than lithium were not created in the BBN process.

- $t \sim$1000 s, T$\sim$ a few tens of keV
  The nucleosynthesis process ceased to occur at this stage, and the nuclei ratio became constant except for free neutrons. Remaining neutrons underwent beta-decays and turned into protons.

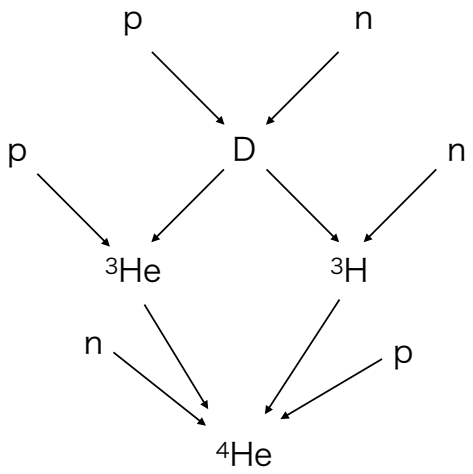

Figure 1.3: Nucleosynthesis process creating $^4\mathrm{He}$ nuclei from protons and neutrons.

1.1.2 V_{ud} determination for testing the CKM matrix unitarity

In the Standard Model, the Cabibbo-Kobayashi-Maskawa (CKM) matrix plays a crucial role to describe the quark mixing. The matrix is written as

$$V_{\mathrm{CKM}} = \begin{pmatrix} V_{\mathrm{ud}} & V_{\mathrm{us}} & V_{\mathrm{ub}} \\ V_{\mathrm{cd}} & V_{\mathrm{cs}} & V_{\mathrm{cb}} \\ V_{\mathrm{td}} & V_{\mathrm{ts}} & V_{\mathrm{tb}} \end{pmatrix} \quad . \tag{1.7}$$

This matrix has four free real parameters, and is unitary according to the Standard Model. Therefore, the experimental measurement to check the unitarity of the matrix is one of the fundamental tests of the Standard Model. At present experimental results are consistent with the matrix being unitarity. For example, the unitarity test of the first quark generation is confirmed with a precision of 0.06% as

$$1 - (|V_{\mathrm{ud}}|^2 + |V_{\mathrm{us}}|^2 + |V_{\mathrm{ub}}|^2) = (6.1 \pm 6.4) \times 10^{-4}. \tag{1.8}$$

The uncertainty is dominated by the experimental accuracy of the V_{ud} measurement. Thus it is required to improve the precision of the V_{ud} measurement for further sensitivity.

There are several independent methods to obtain V_{ud}. The method with nuclear super-allowed beta-decay reactions gives the best precision of $|V_{\mathrm{ud}}| = 0.97420(21)$ [7]. However, the method has theoretical uncertainties originating from the nuclear structure. On the other hand, V_{ud} can be also determined using neutron beta-decays. It is the simplest beta-decay reaction, and there is no theoretical uncertainty originating from the nuclear structure when determining V_{ud}. To evaluate V_{ud} using neutron beta-decays, the ratio of axial vector to vector coupling constant λ is needed, in addition to τ_n. The equation is expressed as

$$\frac{1}{\tau_n} = \frac{G_\mu^2 |V_{\mathrm{ud}}|^2}{2\pi^3} m_e^5 (1 + 3\lambda^2)(1 + \Delta_{\mathrm{RC}}) f, \tag{1.9}$$

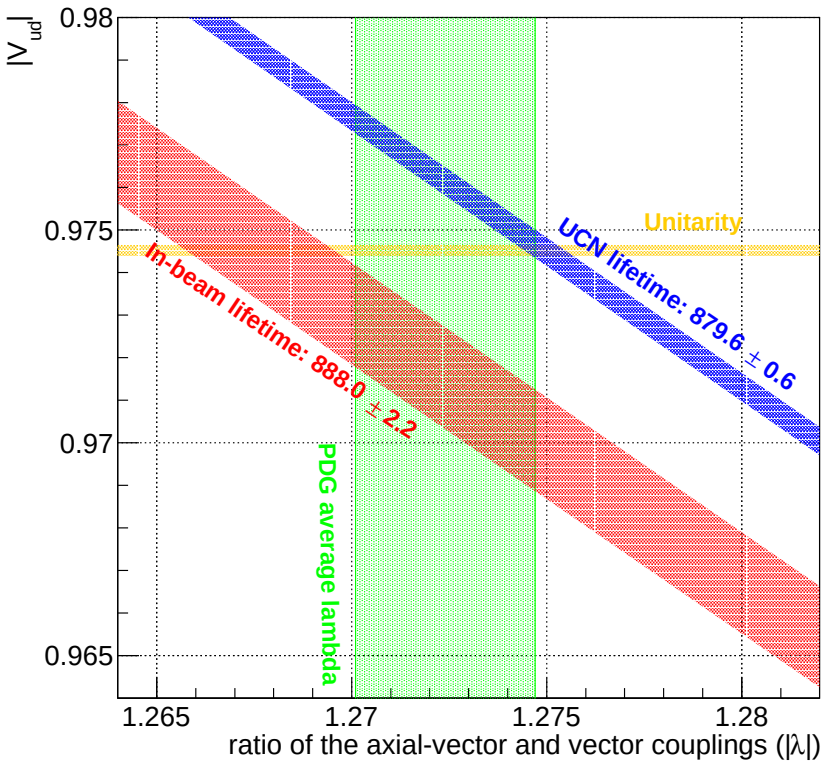

Figure 1.4: Relation between the $|V_{\rm ud}|$ value and the ratio of the axial vector to vector couplings constant (λ) as computed using the neutron lifetime result. The result of $\lambda = -0.12724 \pm 0.00023$ [6] and the unitarity line of $V_{\rm ud}$ [6] are also shown.

where $f = 1.6887$ is a phase space factor, $\Delta_{\rm RC}$ is the electroweak radiative corrections, $G_\mu = 1.16637(1) \times 10^{-5}$ GeV is the Fermi constant evaluated by muon decay [8]. The current $V_{\rm ud}$ value obtained by τ_n and λ is shown in Figure 1.4, which is $0.9700 < |V_{\rm ud}| < 0.9760$ [7]. The result takes into account the discrepancy of the results of neutron beta-decay lifetime (see Section 1.2). The precision is significantly limited by the experimental uncertainties of both τ_n and λ. By improving the experimental precision of τ_n, we open the prospect for a more precise determination of the $V_{\rm ud}$ element.

1.2 Previous neutron lifetime measurements

Since the discovery of a neutron by J. Chadwick in 1932 [9], various experiments have been conducted to measure its decay lifetime. Figure 1.5 shows the experimental results of the lifetime used by the Particle Data Group [6]. The lifetime has been measured mainly by two independent methods: (1) the UCN storage method, and (2) the in-flight method. The average result of the UCN method gives (879.6 ± 0.6) s, while that of the in-flight method gives (888.0 ± 2.0) s. There exists

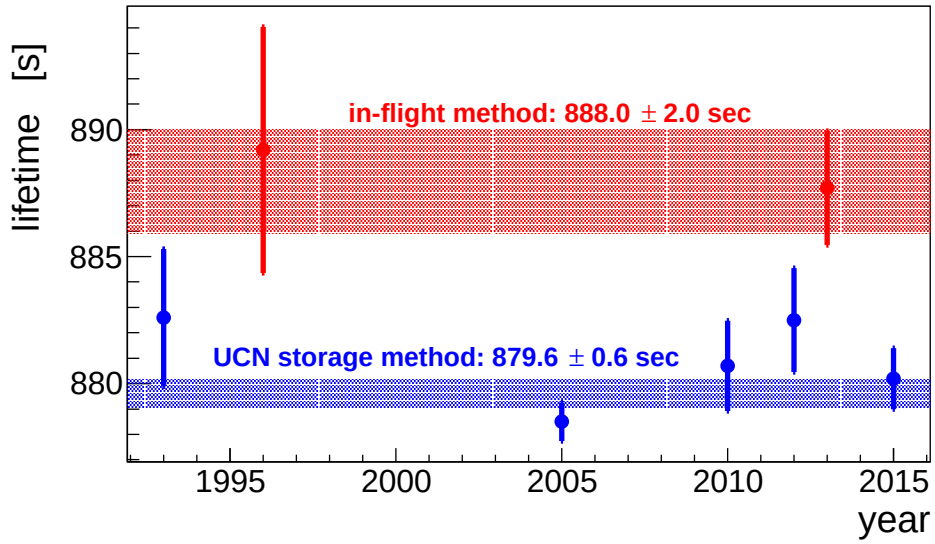

Figure 1.5: Results of previous neutron lifetime measurements [6]. The average of the in-flight method (red) is (888.0 ± 2.2) s, while that of the UCN storage method (blue) is (879.6 ± 0.6) s. There exists a 8.4 s (4.0σ) discrepancy between the results of the two methods.

a significant discrepancy of 8.4 s (corresponding to 4.0σ) between the results of the two methods. This may shake the confidence of the BBN theory, and prevent the further precise unitarity test of the CKM matrix. As a result, the discrepancy becomes one of the serious issues not only in particle physics but in astrophysics and cosmology. In order to resolve this problem, it is desired to evaluate the result using a different experimental method as well as to improve the measurement accuracy.

1.2.1 UCN storage method

In the UCN storage method, neutrons are cooled down into ultra cold neutrons (UCNs), which have velocities of a few m/s and the energies of a few hundred neV. One important characteristic of UCNs is that it feels an averaged potential (the Fermi potential) from the material of the storage chamber and can be reflected, thus allowing UCNs to be stored. The neutron lifetime can be evaluated by counting the number of surviving UCNs after a certain amount of time. One of the experiments using this principle was conducted between 2008 and 2010 in Institut Laue-Langevin by S. Arzumanov [10]. The schematic drawing of the experimental setup is shown in Figure 1.6.

In this setup, UCNs were stored in a stainless steel chamber. The UCN decay rate ($\lambda_{\rm tot}$) came from both beta-decays (λ_β) and the wall loss effect due to the interaction between UCNs and the wall material ($\lambda_{\rm loss}$):

$$\lambda_{\rm tot} = \lambda_\beta + \lambda_{\rm loss}. \tag{1.10}$$

The total decay rate $\lambda_{\rm tot}$ was measured by a proportional gas counter containing ^{3}He gas. In the experiment mentioned above, $\lambda_{\rm tot}$ was measured in two different geometries, for the purpose of changing the UCN collision frequency with the chamber wall. The total decay rate of each geometry

is expressed as

$$\lambda_{\rm tot}^{(1)} = \lambda_\beta + \lambda_{\rm loss}^{(1)} = \frac{\log N_i^{(1)} - \log N_f^{(1)}}{T_f - T_i}, \tag{1.11}$$

$$\lambda_{\rm tot}^{(2)} = \lambda_\beta + \lambda_{\rm loss}^{(2)} = \frac{\log N_i^{(2)} - \log N_f^{(2)}}{T_f - T_i}, \tag{1.12}$$

where the superscript (1) and (2) represent the two geometries of the chamber. The wall loss effect can be estimated using the counts of the thermal neutron detector J as

$$\frac{\lambda_{\rm loss}^{(1)}}{\lambda_{\rm tot}^{(1)}} = \frac{\left(\frac{J^{(1)}}{\varepsilon_{th}}\right)}{\left(\frac{N_i^{(1)} - N_f^{(1)}}{\varepsilon_{\rm ucn}}\right)} \times \frac{\sigma_{\rm ie} + \sigma_{\rm cap}}{\sigma_{\rm ie}}, \tag{1.13}$$

$$\frac{\lambda_{\rm loss}^{(2)}}{\lambda_{\rm tot}^{(2)}} = \frac{\left(\frac{J^{(2)}}{\varepsilon_{th}}\right)}{\left(\frac{N_i^{(2)} - N_f^{(2)}}{\varepsilon_{\rm ucn}}\right)} \times \frac{\sigma_{\rm ie} + \sigma_{\rm cap}}{\sigma_{\rm ie}}. \tag{1.14}$$

In these equations, $\varepsilon_{\rm th}$ and $\varepsilon_{\rm ucn}$ are the detection efficiencies of the thermal neutron counter and the UCN counter, respectively. $\sigma_{\rm ie}$ and $\sigma_{\rm cap}$ are neutron cross sections of the chamber material for inelastic scattering and capturing, respectively. Taking the ratio,

$$\xi \equiv \frac{\lambda_{\rm loss}^{(2)}}{\lambda_{\rm loss}^{(1)}} = \frac{J^{(2)}\lambda_{\rm tot}^{(2)}(N_i^{(2)} - N_f^{(2)})}{J^{(1)}\lambda_{\rm tot}^{(1)}(N_i^{(1)} - N_f^{(1)})}. \tag{1.15}$$

Finally, τ_n can be expressed as

$$\tau_n = \frac{1}{\lambda_\beta} = \frac{\xi - 1}{\xi\lambda_{\rm tot}^{(1)} - \lambda_{\rm tot}^{(2)}}. \tag{1.16}$$

The recent measurement of this method gives the result of (880.2 ± 1.2) s [10].

1.2.2 In-flight method (proton counting)

In this method, a neutron beam entered a decay volume, and protons from the neutron beta-decays were trapped in the volume using a Penning trap technique. After the neutron beam irradiation, the trapped protons were guided into the proton detector and the number is counted. The experiment using this method was conducted by A. T. Yue *et al.* at National Institute of Standards and Technology Center for Neutron Research (NCNR) [11]. The experimental setup is shown in Figure 1.7.

The number of detected protons (N_p) is

$$N_p = \frac{\varepsilon_p L}{\tau_n} \int_A da \int I(v)\frac{dv}{v}, \tag{1.17}$$

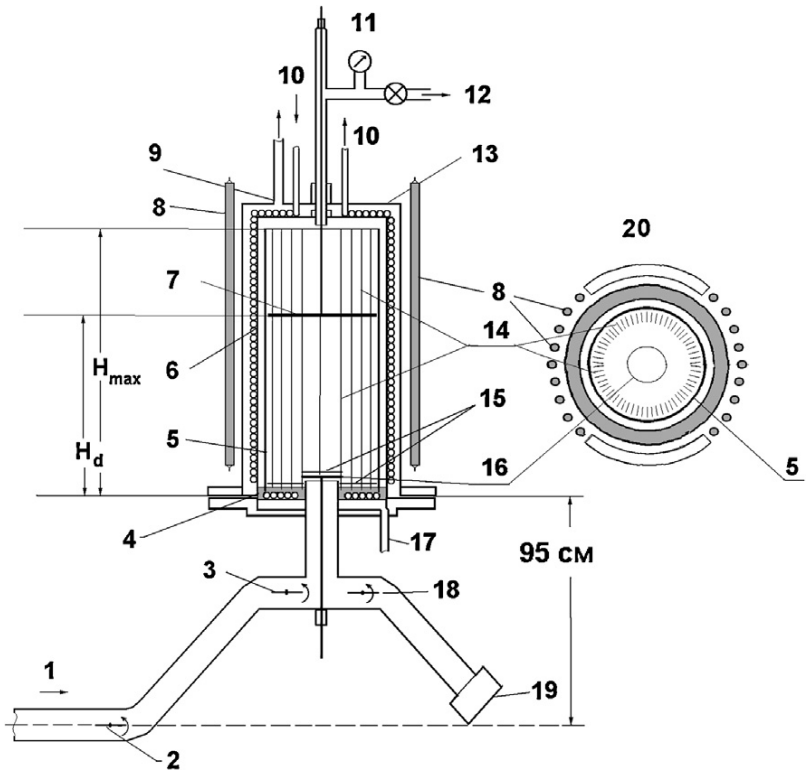

Figure 1.6: Schematic drawing of the experimental setup for the UCN storage method conducted by S. Arzumanov *et al.* in 2015 [10]. UCNs were stored in the stainless steel trap which was installed in the copper cylinder (5). The number of remaining UCNs were counted by the UCN detector (19).

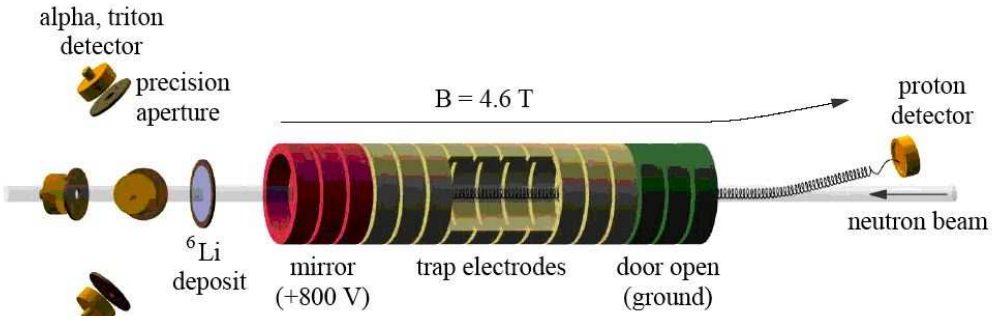

Figure 1.7: Schematic drawing of the experimental setup for the in-flight method conducted by A. T. Yue in 2005 [11]. Protons from neutron beta-decays were trapped in the electrodes and guided towards the proton detector. The neutron beam flux was measured by counting the $^6\mathrm{Li}(n,\ \alpha)^3\mathrm{H}$ events.

where A is the cross section of the decay volume, $I(v)$ is the total neutron fluence for a neutron velocity v, L is the decay volume length, and ε_p is the detection efficiency of the proton detector. On the other hand, the neutron fluence in the decay volume can be estimated by counting the $^6\mathrm{Li}(n,\ \alpha)^3\mathrm{H}$ reaction using a different detector

$$N_{\mathrm{neutron}} = \int_A da \int_{dv} \varepsilon_{\mathrm{neutron}}(v)\sigma(v)I(v)dv \tag{1.18}$$

$$= \varepsilon_{\mathrm{ion}}(v_0)v_0 \int_A da \int_{dv} \sigma(v_0)I(v)\frac{dv}{v}, \tag{1.19}$$

where $\sigma(v_0)$ is the cross section of $^6\mathrm{Li}(n,\ \alpha)^3\mathrm{H}$ at neutron velocity of $v_0 = 2200$ m/s. The detection efficiency of ions from $^6\mathrm{Li}(n,\ \alpha)^3\mathrm{H}$ can be evaluated as

$$\varepsilon_{\mathrm{ion}}(v_0) = 2\sigma(v_0) \int\int dx\ dy \frac{\Omega(x,y)}{4\pi}\rho(x,y)\phi(x,y), \tag{1.20}$$

where $\Omega(x,y)$, $\rho(x,y)$, and $\phi(x,y)$ respectively represent the solid angle of the detector, the $^6\mathrm{Li}$ number density, and the neutron fluence distribution in the plane perpendicular to the beam axis. Finally, τ_n can be expressed as the ratio of the number of these two kinds of events as

$$\tau_n = \frac{\varepsilon_{\mathrm{ion}}(v_0)v_0}{\varepsilon_{\mathrm{proton}}L}\frac{N_{\mathrm{neutron}}}{N_{\mathrm{proton}}}, \tag{1.21}$$

and the result was $\tau_n = (887.7 \pm 1.2\ (\mathrm{stat.}) \pm 1.9\ (\mathrm{sys.}))$ s [12].

1.2.3 In-flight method (electron counting)

In 1989, Kossakowski *et al.* conducted a lifetime measurement at Institut Laue-Langevin reactor using a different method from those described above [13]. The schematic view of the experimental setup is shown in Figure 1.8. The neutron beam was formed into bunches by a rotating drum and a

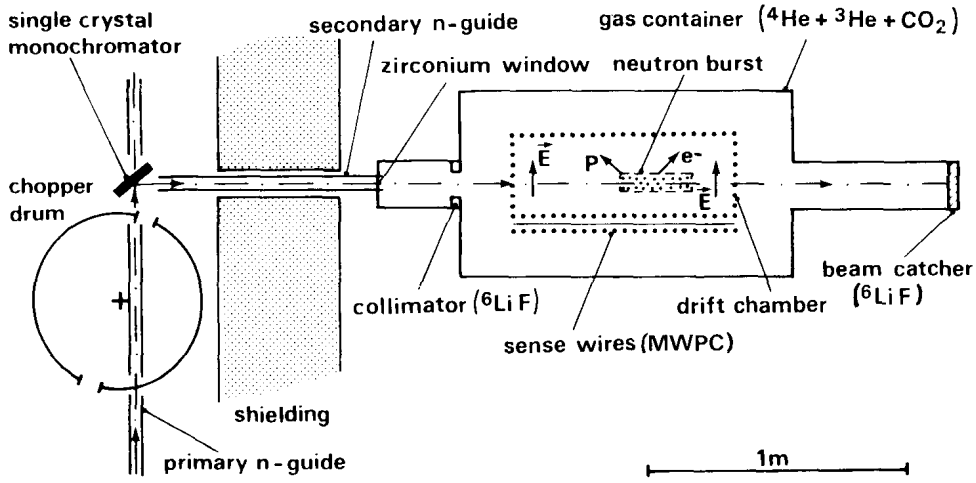

Figure 1.8: Schematic view of the Kossakowski *et al.* experiment in 1989 [13]. The neutron beam was formed into bunches by the rotating chopper drum and the crystal monochromator. The electrons from neutron beta-decays were detected by the TPC.

crystal monochromator, and electrons from neutron beta-decays were detected by a TPC filled with He and CO_2 gas. The number of beta-decay events S_β is expressed as

$$S_\beta = N(1 - \exp(-t/\tau_n)) \tag{1.22}$$

$$\sim N\frac{t}{\tau_n}, \tag{1.23}$$

where N is the number of total neutrons passing through the TPC and t is the time during which a neutron bunch exists in the TPC sensitive volume. A small amount of ^{3}He gas was also injected inside the TPC for the neutron flux measurement. The number of $^3\mathrm{He}(n,\ p)^3\mathrm{H}$ events in the TPC can be expressed using the cross section σ and the ^{3}He density ρ as

$$S_{^3\mathrm{He}} = N(1 - \exp(-\rho\sigma v t)), \tag{1.24}$$

$$\sim N\rho\sigma v t \tag{1.25}$$

where v is the neutron velocity. As a result, τ_n is obtained as the ratio of beta-decay events and $^3\mathrm{He}(n,\ p)^3\mathrm{H}$ events in the TPC with the selection efficiency correction (ε_β and $\varepsilon_{^3\mathrm{He}}$) as

$$\tau_n = \frac{1}{\rho\sigma v}\frac{S_{^3\mathrm{He}}/\varepsilon_{^3\mathrm{He}}}{S_\beta/\varepsilon_\beta}. \tag{1.26}$$

The result of this experiment was $\tau_n = (878 \pm 27(\mathrm{stat.}) \pm 14(\mathrm{sys.}))$ s [13]. The main uncertainty comes from low statistics of the beta-decay events. The result is not currently used to determine the average of the neutron lifetime by the Particle Data Group [6].

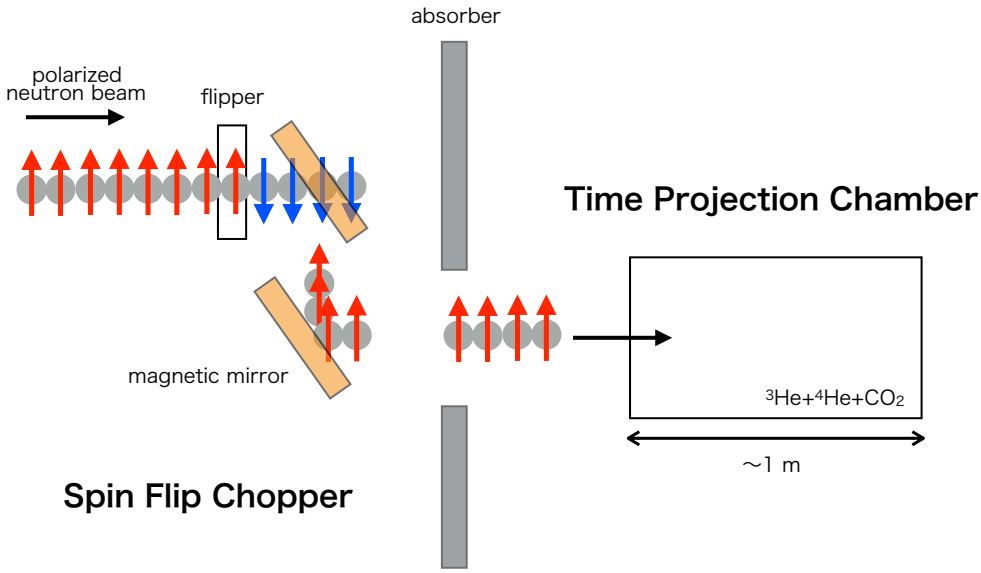

Figure 1.9: Principle of this experiment. The polarized neutron beams are formed into bunches by the SFC, and the number of beta-decay and the $^3\mathrm{He}(n,\ p)^3\mathrm{H}$ events are counted by the TPC.

1.3 This experiment

As described in the previous section, there is a significant discrepancy of the neutron lifetime between the results of the UCN storage method and the in-flight method. An independent τ_n measurement using a different technique is a crucial key to resolve this problem. Therefore, we are conducting the neutron lifetime experiment at J-PARC using the electron-counting method.

1.3.1 Principle

The principle of this experiment is shown in Figure 1.9. This experiment utilizes pulsed neutron beams in the beamline 5 (BL05), at Materials and Life Science Experimental Facility (MLF) of J-PARC. A polarized neutron beam at the beamline first enters a spin flip chopper (SFC), and the neutron beam is formed into bunches. The bunched neutron beams enter the TPC, and the numbers of both beta-decays and $^3\mathrm{He}(n,\ p)^3\mathrm{H}$ events are counted simultaneously. As described in Section 1.2.3, τ_n can be expressed as Eq. (1.26). Here, it is assumed that σ is inversely proportional to the neutron velocity ($1/v$ law) [14], thus $\sigma v = \sigma_0 v_0$, where σ_0=(5333 $\pm$ 7) barn is the $^3\mathrm{He}(n,\ p)^3\mathrm{H}$ cross section for a neutron with a velocity of $v_0 = 2200$ m/s [15]. Using this relation,

$$\tau_n = \frac{1}{\rho\sigma_0 v_0}\frac{S_{^3\mathrm{He}}/\varepsilon_{^3\mathrm{He}}}{S_\beta/\varepsilon_\beta}. \tag{1.27}$$

The advantages of our experiment compared to previous types of measurements can be summarized as follows.

- Forming neutron bunches by the SFC

Table 1.1: Comparison of our experiment and the Kossakowski $et\ al.$ experiment [13] [16]. The values with * will be improved in the future.

	Kossakowski $et\ al.$ experiment	our experiment
Year	1989	2014∼
Facility	Institut Laue-Langevin	J-PARC
Neutron source	reactor	accelerator
Neutron wavelength	4.73 Å	2∼8 Å
Neutron flux at detector [n/s]	2×10^5	1×10^5 *
Beta-decay event rate	0.1 cps	0.08 cps *
Pulse repetition rate	110 Hz	25 Hz
Beam size	ϕ20∼30 mm × 230 mm	ϕ20∼30 mm × 400 mm
TPC dimension	190 mm × 190 mm × 700 mm	300 mm × 300 mm × 960 mm
TPC operation gas (^{4}He:CO_2:^{3}He)	88 kPa : 7 kPa : 10 mPa	85 kPa : 15 kPa : ∼100 mPa
Data acquisition time	34 hours	4×10^3 hours *
Statistical uncertainty	3.1%	0.49% *

- Utilizing the intense pulsed neutron beams at J-PARC
- Measuring the neutron fluence within the same detector

In this experiment, the pulsed neutron beam is formed into bunches, and the signal event is counted only in the time window when each of neutron bunches is completely inside the TPC sensitive region. This eliminates the uncertainty coming from neutron interaction with the material, which currently becomes one of the main uncertainties in the UCN storage type of measurement. For the bunch formation, the high-intensity pulsed neutron beam is entirely favorable from the perspective of beam flux. Moreover, the neutron fluence and neutron beta-decays can be measured simultaneously by a single detector (TPC). As a result, the interdetector calibration between the beta-decay counter and the flux monitor does not produce any systematic uncertainties. This is a great advantage of our experiment compared to the previous proton-counting measurement.

The previous neutron lifetime measurement by Kossakowski $et\ al.$ utilized the same experimental principle as ours. However, the precision was significantly limited due to the low statistics of the beta-decay events. Since the pulsed neutron beams are used, our experiment has sufficient potential to exceed the measurement precision of the previous experiment. Table 1.1 compares our experiment and Kossakowski $et\ al.$ experiment. After the SFC upgrade as described in Section 7.2, 100-days data taking is expected to yield 1 second statistical uncertainty at the design MLF operation power of 1 MW.

Outline of this thesis

Chapter 1 gives an introduction of the neutron lifetime experiment. The physics motivation for the lifetime measurement are discussed in this section. In addition, the advantage of our experiment compared to the previous lifetime measurements are also introduced in this section. Chapter 2 describes the experimental setup of the beamline. The performance and the calibration method as

well as its specification are described. In Chapter 3, the acquired data set, the data acquisition cycle, and the data quality are explained. The detail of the Monte Carlo simulation is described in Chapter 4. In the particle simulation section, detail processes of the simulated events are discussed. In the detector simulation section, the physics model implementation to reproduce the detector output is introduced. Chapter 5 explains the data analysis algorithm. This chapter mainly focuses on the background subtraction method to evaluate the signal events. At last, the $^3\mathrm{He}$ number density measurement is also discussed. The Results of the data analysis are shown in Chapter 6. The systematic uncertainties of the neutron lifetime is also listed in this section. Finally, Chapter 7 summarizes our experiment, with some upgrade plans for improving the measurement precision in the future.

Contribution to this experiment

From the time I joined the lifetime experiment at J-PARC in 2015, I have significantly contributed to both hardware and software work, in addition to taking the physics data. From the perspective of hardware, I developed a helium control gas sample, whose $^3\mathrm{He}$ to $^4\mathrm{He}$ ratio was precisely controlled, using the gas handling system at J-PARC, which resulted in reducing the systematic uncertainty of the neutron lifetime. I also developed a small prototype TPC and constructed a general energy calibration model using the Tandem accelerator at the University of Tsukuba. The model is currently implemented in the Monte Carlo simulation. Regarding the software, based on the careful observation of the TPC event display, I discovered a new type of background which had not been taken into account at the time. I also invented a novel track detection algorithm using the image recognition technique, which greatly reduced the uncertainty related to the pileup event. Moreover, I implemented several physics processes in the Monte Carlo simulation to reproduce the experimental distribution.

With the contribution described above, I have led my collaboration group since 2016, and played a central role in analyzing the data from 2014 to 2018.

Chapter 2

Experimental setup

This chapter describes the experimental setup of the neutron lifetime measurement at Japan Proton Accelerator Research Complex (J-PARC). The detailed experimental setup for each gas fill data is discussed in Section 3.3.

2.1 Facilities and experimental setup

2.1.1 J-PARC facilities

J-PARC is a high-intensity proton accelerator facilities at Tokai, Ibaraki Prefecture, which is jointly managed by JAEA (Japan Atomic Energy Agency) and KEK (High Energy Accelerator Research Organization). A proton beam is accelerated by three types of accelerators, up to 400 MeV by the Linac, 3 GeV by the Rapid Cycle Synchrotron, and 50 GeV by the Main Ring. Figure 2.1 shows a bird's eye view of J-PARC with the three accelerators emphasized. A fraction of the proton beam from the Rapid Cycle Synchrotron enters the Materials and Life Science Experimental Facility (MLF). Here, proton beams with a current of 333 μA interact with carbon graphite and mercury targets to produce pulsed muons and neutrons, respectively, as a result of nuclear spallation reaction. The repetition frequency of the spallation is 25 Hz. The resulting neutrons are cooled down to a few tens of meV by a liquid-hydrogen moderator surrounding the mercury target.

The neutron lifetime experiment is conducted at the BL05 Neutron Optics and Fundamental Physics beamline (NOP beamline), which is out of the 21 neutron beamlines at MLF. This beamline is constructed for precise measurements of fundamental physics using pulsed neutron beams. In addition to the lifetime experiment, measurements of neutron scattering and interference are undergoing at this beamline.

2.1.2 Polarized beam branch

Neutron beams at BL05 are divided by super mirrors into three beam branches: polarized, non-polarized, and low-divergence beam branches. The specifications of the three beam branches are listed in Table 2.1. The neutron lifetime experiment is conducted using the polarized beam branch in order to form a neutron bunch from the polarized neuron pulse beam (see Section 2.2).

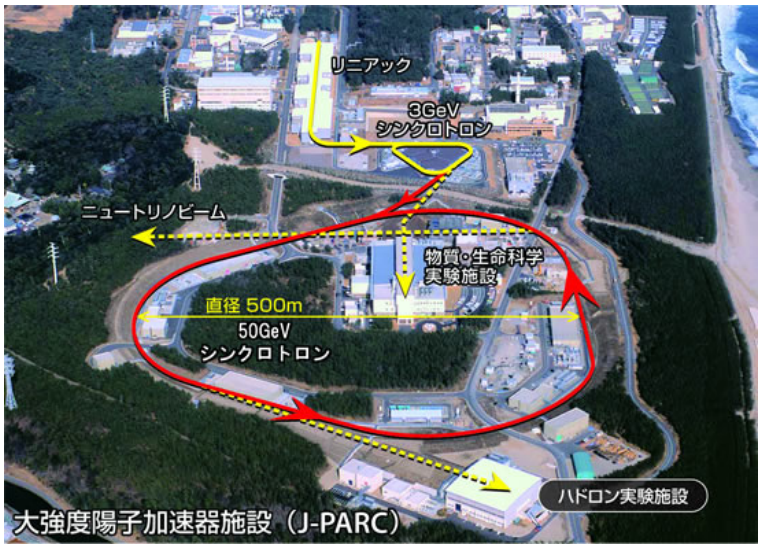

Figure 2.1: Bird's eye view of J-PARC [17]. Proton beams are accelerated by three types of accelerators: 400 MeV linear accelerator, 3 GeV rapid cycle synchrotron, 50 GeV main ring.

Table 2.1: The characteristics of the three beam branches in the BL05 at the design power of MLF (1 MW) [18] [19].

Branch name	Beam size (ver.× hor.[mm^2])	Beam flux [n/(cm^2 · s)]	Divergence (ver.×hor.[mrad^2])	Luminance (n/(cm^2 · str · s))	Polarization ratio
Non-polarized	50×40	$(3.8 \pm 0.3) \times 10^8$	m=2	—	—
Polarized	120×60	$(4.0 \pm 0.3) \times 10^7$	23 × 9.4	$(1.8 \pm 0.1) \times 10^{11}$	0.94∼0.97
Low-divergence	80×40	$(5.4 \pm 0.5) \times 10^4$	0.23×0.23	$(1.0 \pm 0.1) \times 10^{12}$	—

The magnetic super mirrors selectively guide neutrons to the beam branch depending on their polarization direction, and the polarization is 94∼97% [18]. The neutron flux is expected to be $(4.0 \pm 0.3) \times 10^7$ neutrons/(cm^2·s) at the designed MLF operation power of 1 MW [19].

2.1.3 Beamline setup

Figure 2.2 shows a schematic view of the polarized beam branch. The z-axis is defined as the neutron momentum direction, y-axis as the vertical direction, and the x-axis to satisfy the right-handed system. The pulsed neutron beams at this beam branch first enter the SFC. Here, each neutron pulse is formed into five bunches. A TPC filled with He and CO_2 gas is located at about 20 m downstream from the neutron source. It detects both neutron beta-decays and $^3\mathrm{He}(n,\ p)^3\mathrm{H}$ reaction simultaneously. Iron and lead shields surrounding the TPC significantly suppress the event rate of environmental background inside the TPC. The TPC is also surrounded by 14 sets of plastic scintillators, thus almost every cosmic ray event passing through the TPC can be identified and rejected from the beta-decay event. The neutron beam can be switched on and off by a 5 mm-thick LiF plate.

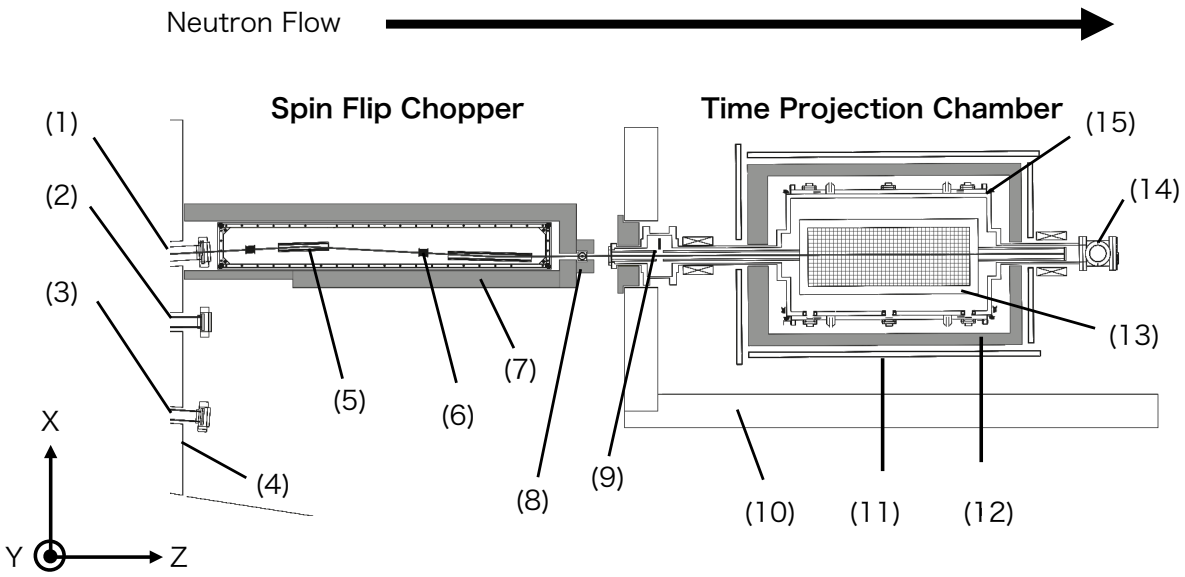

Figure 2.2: Schematic view of the polarized beam branch [20]: (1) exit of polarized beam branch, (2) exit of non-polarized beam branch, (3) exit of low-divergence beam branch, (4) lead shield, (5) magnetic super mirror, (6) radio-frequency coil, (7) (8) lead shield, (9) neutron shutter (5 mm-thick LiF), (10) iron shield, (11) plastic scintillator, (12) lead shield, (13) TPC, (14) beam dump, (15) vacuum chamber.

2.2 Spin flip chopper

In this experiment, the SFC is utilized to form neutron bunches from a polarized neutron beam. It is composed of two radio-frequency (RF) coils and three magnetic super mirrors, surrounded by a lead shield. A magnetic field of 1 mT is applied in the vertical direction throughout the SFC to maintain the neutron polarization. The polarization direction can be flipped after passing through each of the RF coil when an alternative current is applied. At the magnetic super mirror, only a non-flipped neutron can be reflected and guided downstream. By controlling the applied current of the two RF coils, as described in Figure 2.3, a neutron bunch with an arbitrary length can be formed from the neutron pulse.

2.2.1 Radio-frequency coil

Figure 2.4 shows the picture of a radio-frequency coil. It has a 50 mm diameter and a 40 mm length in total. A guide magnetic field B_y is applied in the vertical direction. The coil gives an alternating magnetic field in the z direction, the amplitude of which is expressed as B_z. The neutron polarized in the y direction starts a precessional motion in the RF coil due to the alternating magnetic field.

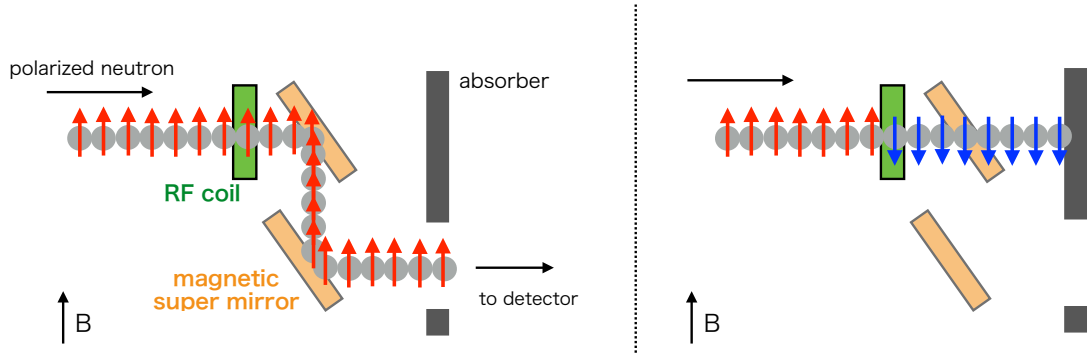

Figure 2.3: Principle of the SFC operation. The neutron beam can pass through the SFC when no current is applied at the RF coil (left), and is absorbed when an alternative current is applied (right).

The flipping probability of the neutron polarization direction P can be expressed as

$$P = \frac{B_z^2}{B_z^2 + \left(B_y - \frac{\hbar w}{2|\mu_n|}\right)^2} \sin^2 \left[\frac{|\mu_n|}{\hbar} \sqrt{B_z^2 + \left(B_y - \frac{\hbar w}{2|\mu_n|}\right)^2}\, t \right], \tag{2.1}$$

where $\hbar$ is a Planck's constant, μ_n is a magnetic moment of a neutron, and ω is an angular speed of the alternating magnetic field. The parameter t is the time in which a neutron exists in the RF coil, which is typically 10 μs at this beamline. One of the resonance conditions, at which the flipping probability becomes one, is expressed as

$$B_y = \frac{\hbar\omega}{2|\mu_n|}, \tag{2.2}$$

$$\frac{|\mu_n|}{\hbar} B_z t = \left(n + \frac{1}{2}\right)\pi. \tag{2.3}$$

This condition is realized at B_y= 1 mT, B_z= 0.3 mT, and $\omega = 2\pi \times 29$ kHz.

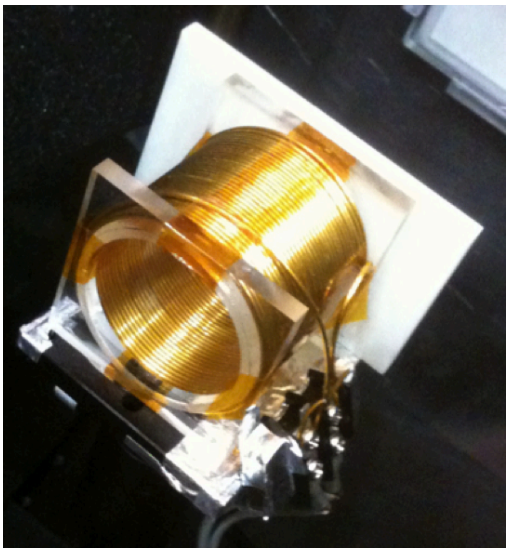

Figure 2.4: Picture of the radio-frequency coil [21].

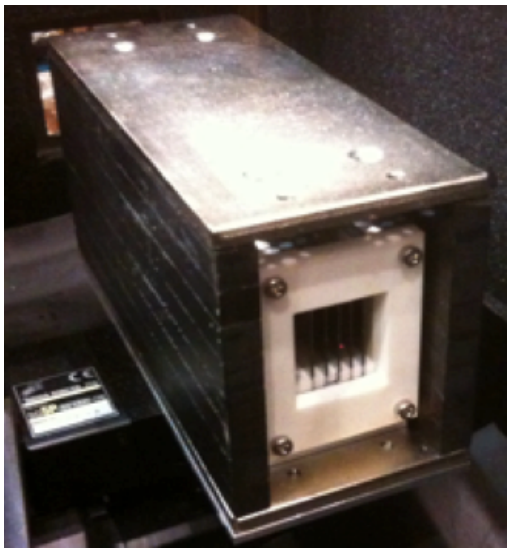

Figure 2.5: Picture of the magnetic super mirror [21].

2.2.2 Magnetic super mirror

Cold neutrons at the polarized beam branch have a de Brogile wavelength of a few angstrom on average, which is the same order of an atomic distance. Cold neutrons therefore feel an average potential from a material. Nickel, which is known to have a large potential, can reflect a cold neutron with an incident angle smaller than about 0.1°. A super mirror is developed to achieve a larger reflection angle, and has recently been widely used in many applications. It is composed of two kinds of substances with different potential, typically Ni and Ti. They are alternately stacked, the thicknesses of which are gradually changed. This realizes reflection of a neutron with a large incident angle due to Bragg reflection.

A magnetic super mirror is composed of many layers of ferromagnetic and non-ferromagnetic substances. Since a magnetic field is applied, the potential a neutron feels in the ferromagnetic substance changes. Therefore, only neutrons with a certain polarization direction can be selectively reflected at the mirror. This means the magnetic super mirror works as a spin polarizer for a neutron. A picture and a specification of the mirror used in this experiment is shown in Figure 2.5 and Table 2.2. The mirror reflects a neutron with its incident angle up to 5 times larger than a pure Ni material (m value is 5).

2.2.3 Neutron time-of-flight distribution

During a normal operation of the SFC, the current applied to the two RF coils is adjusted to form 5 neutron bunches per pulse. The length of each bunch is about 40 cm, which is much shorter than that of the TPC in the z direction ($\sim$ 100 cm). The distribution of time of flight (TOF), defined as the time length from the neutron pulse generation to the trigger timing of the TPC, is shown in

Table 2.2: Specification of the magnetic super mirror in the SFC [21].

Ferromagnetic substance	Fe
Non-ferromagnetic substance	$SiGe_3$
Magnetic field	35 mT
Dimensions	140 mm × 35 mm × 0.7 mm
Number of layers	7445
m value	5

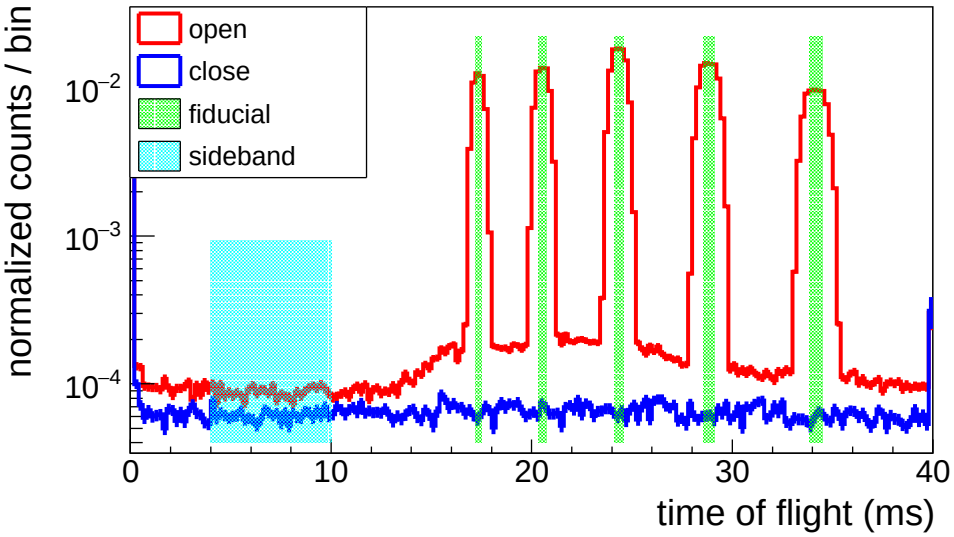

Figure 2.6: Time-of-flight distribution of $^3\mathrm{He}(n,\ p)^3\mathrm{H}$ events in the TPC. The red and blue histograms represent the shutter-open and shutter-closed data, respectively. Each of the five green bands represents the fiducial time, in which a neutron bunch is completely inside the TPC sensitive region. The light blue band represents the sideband region, during which no neutron bunch is inside the TPC.

Figure 2.6 for $^3\mathrm{He}(n,\ p)^3\mathrm{H}$ events. Five peaks originating from the neutron bunches are clearly seen in the figure. The "fiducial time" is defined as the time during which each neutron bunch is crossing on the center line of the TPC, as described in Fig 2.7. During the fiducial time, since all neutrons in a bunch are completely contained in the TPC, 4π solid angle acceptances for both beta-decays and $^3\mathrm{He}(n,\ p)^3\mathrm{H}$ are guaranteed. The fiducial times are expressed as green bands in the figure. The sum of the five fiducial times is 2.35 ms per pulse, corresponding to 5.8% of the total measuring time. The "sideband time", during which no neutron bunches exist inside the TPC, is determined as $4\ \mathrm{ms} \leqq \mathrm{TOF} \leqq 10\ \mathrm{ms}$, corresponding to 15% of the total measuring time.

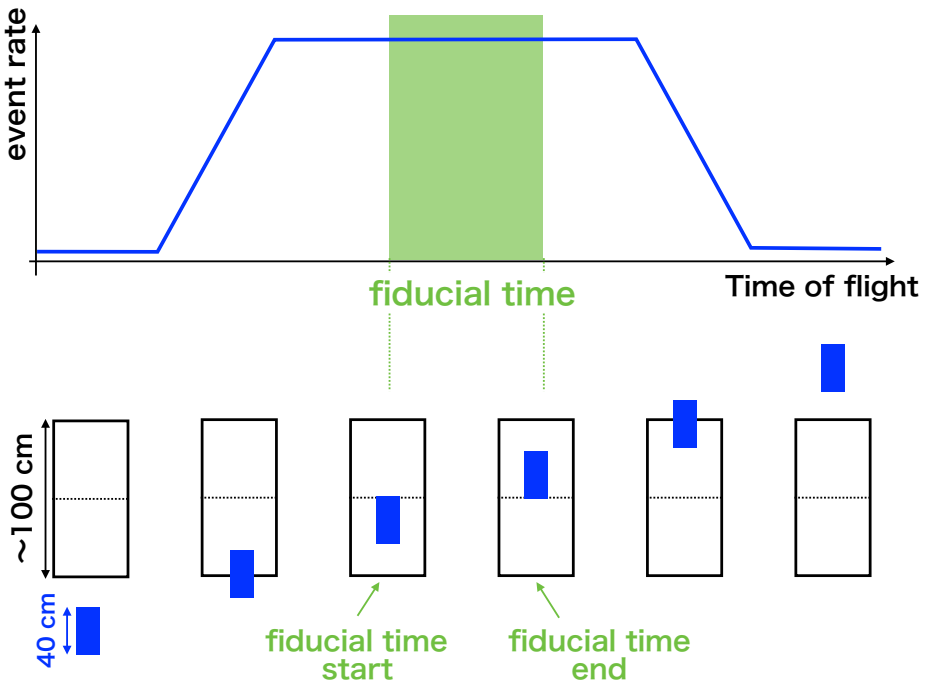

Figure 2.7: Definition of the fiducial time along with the positional relation of a neutron bunch in the TPC. The fiducial time is defined as the time during which the neutron bunch crossing on the center line of the TPC.

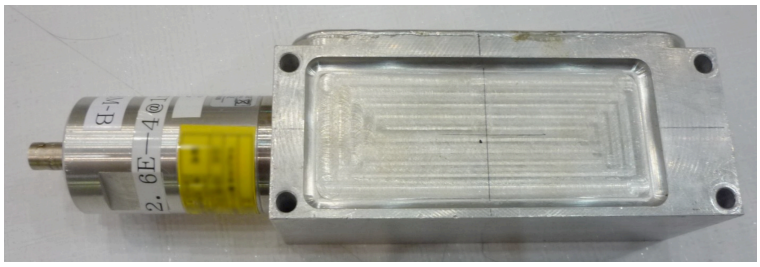

Figure 2.8: Picture of the neutron beam monitor [22].

2.3 Beam flux monitor

A neutron flux monitor manufactured by CANBERRA is set at the exit of the SFC. A picture of the flux monitor is shown in Figure 2.8. Argon, methane, and a small amount of $^3\mathrm{He}$ gas are contained in the monitor, and the $^3\mathrm{He}(n,\ p)^3\mathrm{H}$ event inside the monitor is detected. An area of the sensitive region is 10 cm $\times$ 4.2 cm, and its detection efficiency is measured to be about 10^{-5} for a thermal neutron. The stability of the monitor against temperature and high voltage shifting was previously studied [22], and it was found to satisfy our requirement of monitoring the neutron flux with a precision of 0.1%.

The output pulse height of the beam monitor is taken by an ADC throughout the lifetime measurement. The pulse height distribution is shown in Figure 2.9. A threshold level is set at 66% of the energy peak position, which is indicated as a red line in the figure. The number of events at the beam monitor is used to correct for the beam flux fluctuation at the beam line. The algorithm to correct for the flux fluctuation is described in Section 5.3.1.

2.4 Neutron beam shutter

A neutron shutter, composed of 5 mm-thick LiF plate, is set just upstream of the TPC in the vacuum chamber. The suppression ratio of this shutter is estimated to be 5×10^{-4}. The shutter can be switched on and off by a remote control system; thus both the shutter-open and shutter-closed data can be obtained. Figure 2.10 shows a mechanism to control the neutron shutter. Two 60 mm $\times$ 60 mm LiF plates are attached on a plastic plate, which can be rotated by a rotary stage. The right one is used to stop the neutron beam in the shutter-closed mode, while the right one, with a 30 mm $\times$ 30 mm hole, in the shutter-open mode.

In the lifetime measurement, the shutter-open and shutter-closed data is taken alternately, in order to estimate the background event rate in the TPC. For the calibration measurement, the neutron shutter is set at the closed mode. The detail of the algorithm to subtract the background event in the TPC is introduced in Section 5.3.1

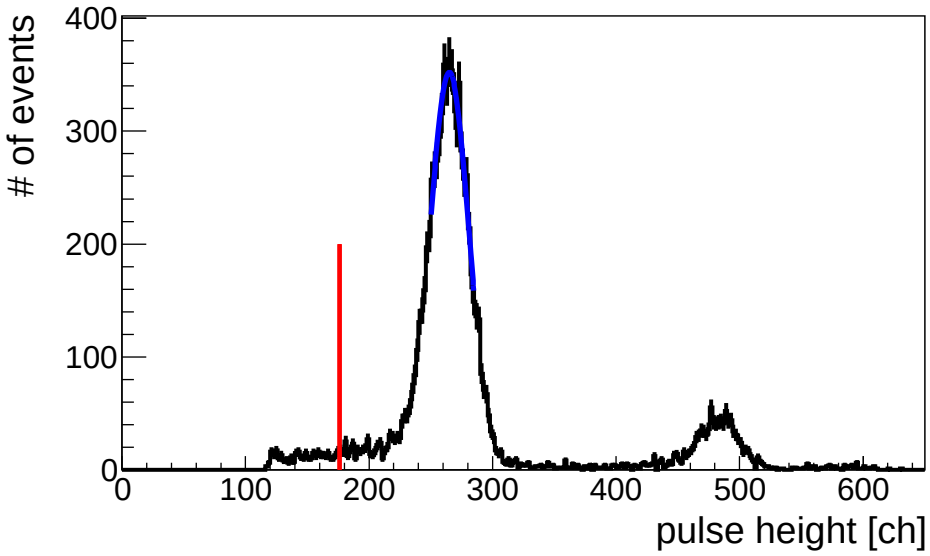

Figure 2.9: Pulse height distribution of the beam monitor. The main peak is fit by a gaussian function, and the energy threshold is set at 66% of the peak position (drawn as a red line in the figure). The small peak at 500 ch comes from the pileup event. The small peak at around 500 ch comes from neutron capturing process by boron nuclei ($^{10}\mathrm{B}(n,\ \alpha)^{7}\mathrm{Li}$), which are expected to be contained in the inner wall of the beam monitor.

2.5 Veto counter

In order to identify cosmic rays event in the TPC, 12 mm-thick plastic scintillators are installed around the TPC. Every scintillation light is converted into an electric signal by a photomultiplier and read out independently. As shown in Figure 2.11, each side of the TPC, except for the bottom side, is surrounded by two superposed scintillation counters. Furthermore, one more set of counters are used in the front and back sides to avoid neutron beam ports of the TPC. Fourteen scintillation counters are installed in total, and a cosmic ray trigger is produced when any of the 7 sets of counters coincide. The event rate of the cosmic ray trigger is about 1 kcps, while that of the coincidence of the cosmic ray trigger and any of the 24 anode wires is about 50 cps. The detection efficiency for a cosmic ray event was measured to be 96% [20].

2.6 Shield

A vacuum chamber containing the TPC is completely surrounded by a lead shield as shown in Figure 2.12. The lead shield is put into an iron case, and the thickness is 10 cm for the front side and 5 cm for the other five sides, respectively. It is installed to suppress environmental γ-rays and prompt γ-rays mainly originating from the SFC and the neutron target. The performance of the shield is measured by a NaI scintillation counter; with this shield, the event rate of environmental γ-rays is measured to be decreased by 2% [20].

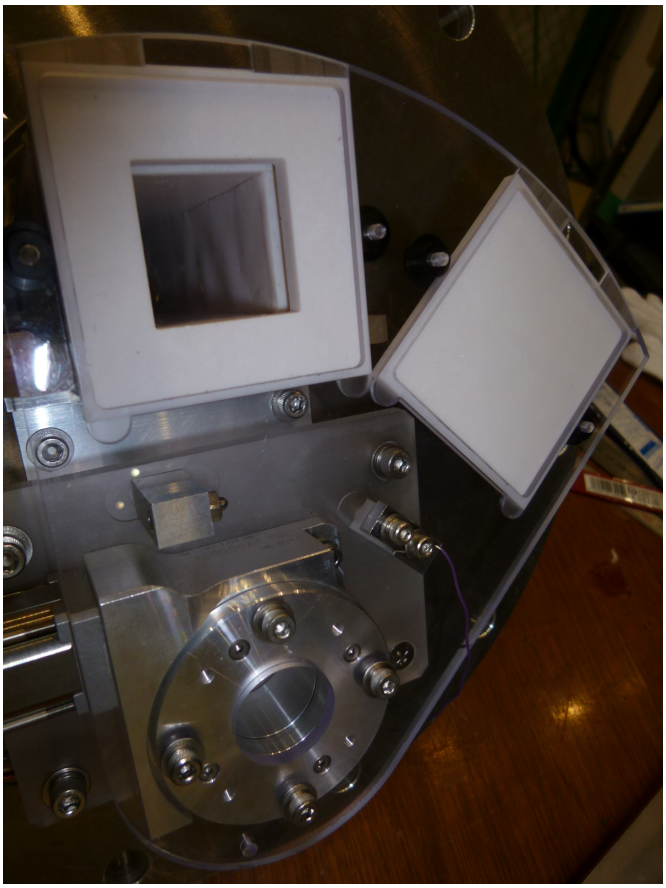

Figure 2.10: Picture of a neutron shutter system. Two LiF plates, the size of which is 60 mm $\times$ 60 mm $\times$ 5 mm, are attached to a rotary stage. The left plate has a 30 mm $\times$ 30 mm hole, which is used in the shutter-open mode. The right plate is used in the shutter-closed mode. The two states can be switchable from the remote control system by rotating a plastic plate.

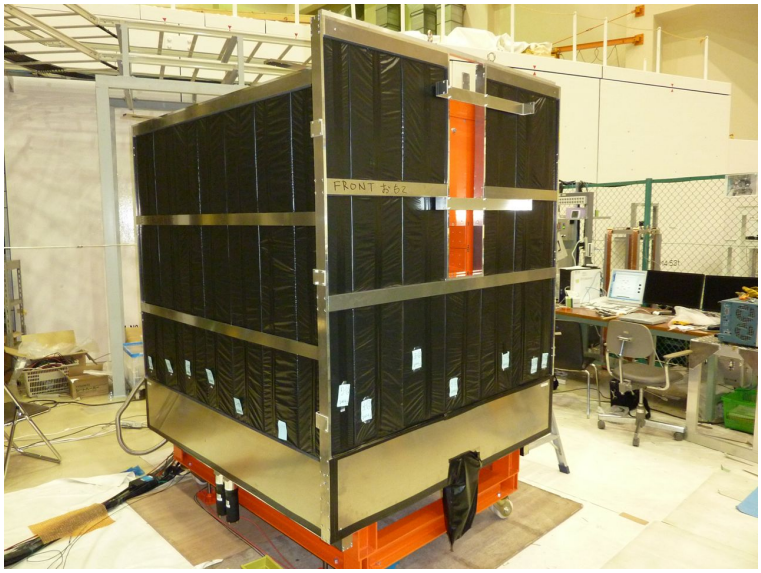

Figure 2.11: Picture of the cosmic rays veto counters [21]. Fourteen plastic scintillators (shown as black plates in the figure) cover the TPC except for the bottom side.

Figure 2.12: Picture of lead shield surrounding the TPC [21]. The thickness is 10 cm for the front side and 5 cm for the other five sides, respectively.

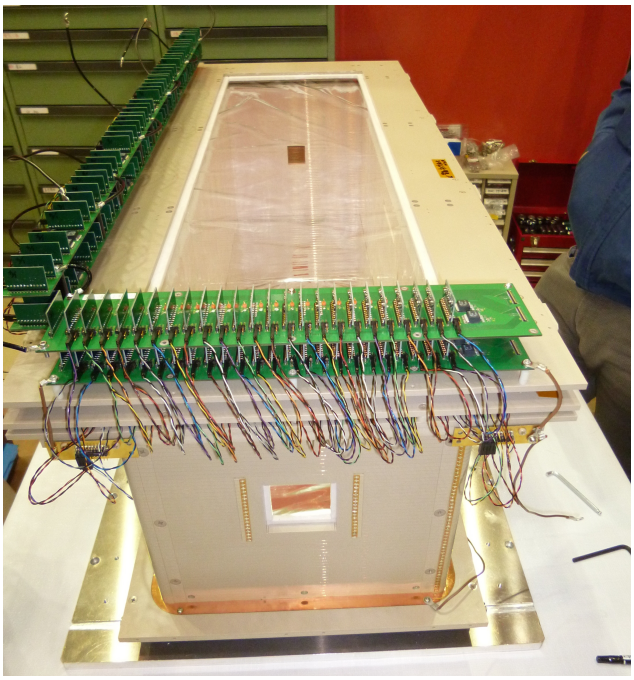

Figure 2.13: Picture of the TPC taken from the downstream side.

2.7 Time projection chamber

In this experiment, a TPC with a two-dimensional multi wire proportional chamber (MWPC) is specially developed to detect both neutron beta-decays and $^3\mathrm{He}(n,\ p)^3\mathrm{H}$. A picture of the TPC is shown in Figure 2.13. The dimensions are 30 cm $\times$ 30 cm $\times$ 100 cm, and He and CO_2 gases are filled as operation gas. The detailed specifications of the TPC are listed in Table 2.3. Ionized electrons from beta-decays or $^3\mathrm{He}(n,\ p)^3\mathrm{H}$ reaction drift upwards by a uniform electric field of 300 V/cm, and it causes an avalanche multiplication at the MWPC region located at the top of the TPC. The MWPC is composed of three wire layers, and the geometrical structure is shown in Figure 2.14. In the middle layer, 24 anode wires having 20 μm diameters and 24 field wires having 50 μm diameters are aligned alternately with a interval of 6 mm. In the above and below layers, 162 cathode wires having 50 μm-diameters are aligned perpendicular to the anode and field wires, and every 4 cathode wires in the same layer are electrically connected and read out as a single channel. The equipotential lines of the TPC and MWPC calculated by Garfield software [23] are shown in Figure 2.15 and 2.16, respectively.

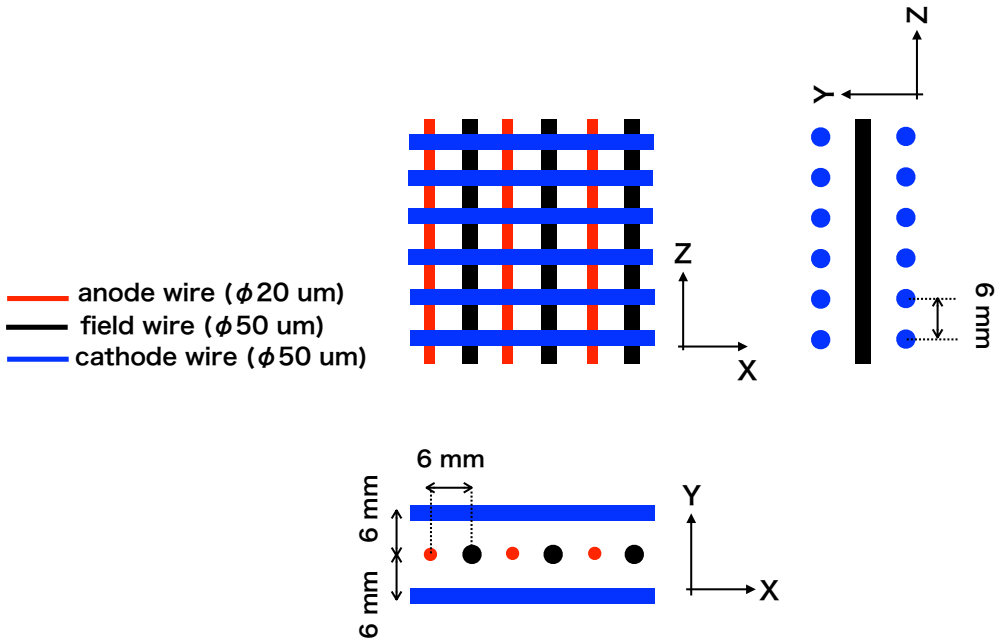

Figure 2.14: Wire structure of the MWPC. The diameter of anode wires, field wires, and cathode wires are 20 μm, 50 μm, and 50 μm, respectively. Cathode wires are aligned in the top and bottom layers, and anode and field wires are aligned alternately at 6 mm intervals in the middle layers.

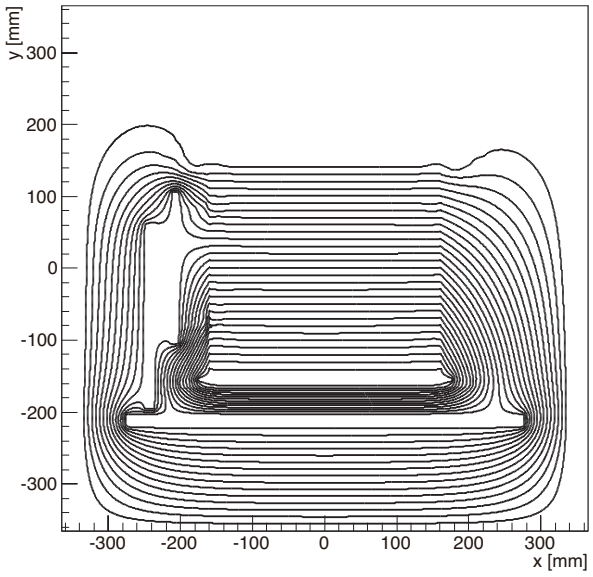

Figure 2.15: Equipotential lines of the TPC in the x-y plane calculated by Garfield software [23]. The figure is taken from H. Otono's Ph.D. dissertation [21].

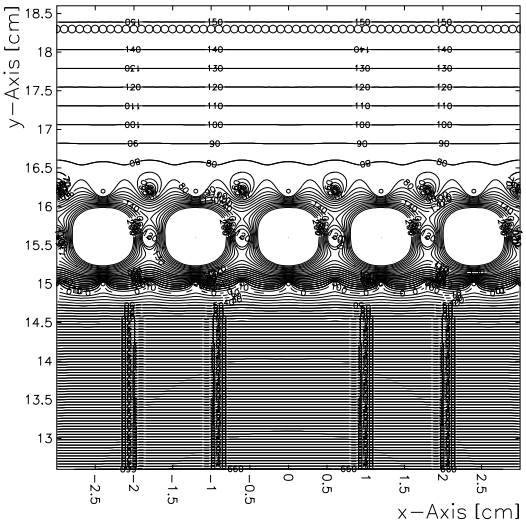

Figure 2.16: Equipotential lines of the MWPC in the x-y plane calculated by Garfield software [23].

Table 2.3: Basic parameters of the TPC [20].

Dimensions	$300\ \mathrm{mm} \times 300\ \mathrm{mm} \times 960\ \mathrm{mm}$
Anode wire (24 ch)	$\phi 20\ \mu\mathrm{m}$, $1720\ \mathrm{V}$
Field wire (24 ch)	$\phi 50\ \mu\mathrm{m}$, $0\ \mathrm{V}$
Cathode wire (40 ch$\times$ 2)	$\phi 50\ \mu\mathrm{m}$, $0\ \mathrm{V}$
Electric field	$300\ \mathrm{V/cm}$ (vertical direction)
Drift velocity	$1.0\ \mu/\mathrm{s}$
Multiplication factor	5×10^4
Gas composition	^{4}He (85 kPa), CO_2 (15 kPa), ^{3}He (100 mPa)

The TPC has the following characteristics specialized for this experiment.

- Low background condition
  Since the probability for a neutron to undergo beta-decays inside the TPC is about 10^{-6}, the event rate of neutron beta-decays corresponds to only 1 cps at 200 kW operation. The event rate of background events, such as cosmic rays, environmental radiation, and prompt γ-ray emission from neutron capture reaction, should be significantly suppressed to realize extremely low background condition for counting neutron beta-decays. It is shielded by lead and iron shields, and plastic scintillators surrounding the TPC are used to identify a cosmic ray event passing through the TPC. Furthermore, the material used to construct the TPC are carefully selected to reduce the environmental radiation.

- ^{3}He density control
  In this experiment, an incident neutron flux is evaluated by counting $^3\mathrm{He}(n,\ p)^3\mathrm{H}$ events in the TPC. Since the ^{3}He number density is used for this evaluation, the ^{3}He pressure in the TPC is required to be precisely controlled during the measurement. Once operation gas is injected in the TPC, therefore, it is kept sealed during the measurement. The TPC condition gradually changes, such as the deterioration of the multiplication factor and the increase of an attenuation effect for drift electrons. The time transition of these effects should be monitored throughout the measurement.

- No magnetic field
  The TPC in this experiment does not need to measure the momentum of a charged particle, as is often the case with a TPC used in a collider-type experiment. As a result, no magnetic field is applied in the TPC.

- Low scattering cross section for neutrons
  A neutron scattered by operation gas molecules causes interaction with a TPC wall material to produce prompt γ-rays. Because such a process becomes a background for beta-decays, the operation gas is selected to make the scattering probability in the TPC as low as possible. In addition, the inside walls of the TPC are covered by the LiF plates. ^{6}Li nuclei in the plate can capture neutrons without almost no prompt γ-rays emission, which greatly contributes to reducing the background event for neutron beta-decays.

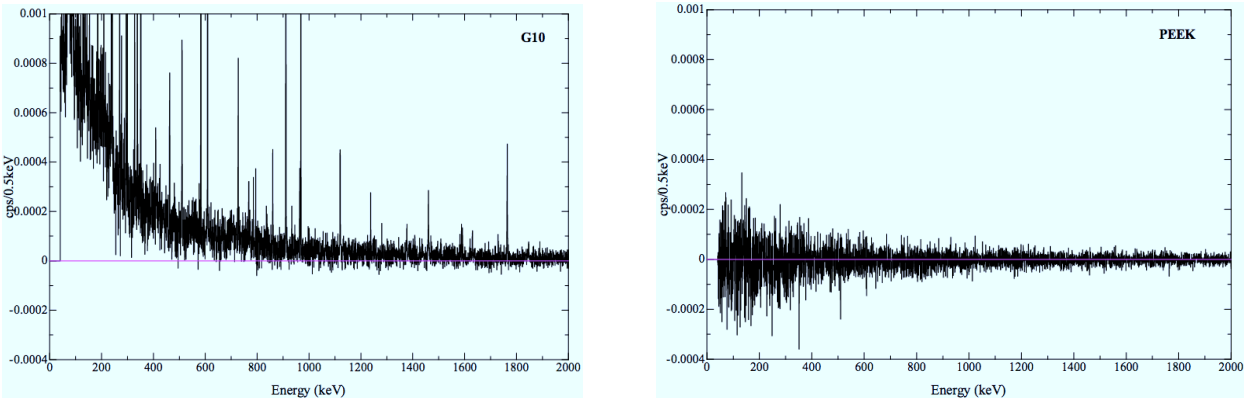

Figure 2.17: Background-subtracted energy spectra for G10 (left) and PEEK (right) measured by a Germanium detector. The vertical axis is normalized by the measuring time. The two figures are taken from H. Otono's Ph.D. dissertation [21].

Table 2.4: Physical properties of PEEK [24] [25].

Density	1.3 g/cm^3
Melting point	335 °C
Water absorption after 24 hours at 40% relative humidity	0.15%
Flexural modulus	3.8 GPa
Heat distortion temperature	165°C
Volume resistivity	$> 10^{16}\ \Omega \cdot \mathrm{cm}$

2.7.1 Material selection for low-background condition

Material constructing the TPC is required to have small amount of radioactive sources in order to suppress the background flux for beta-decay. Polyethel ethel ketone (PEEK), polyphenylene sulfide, phenol formaldehyde resin (PF), epoxy glass laminate (G10), and Alumina, were listed as candidates for the TPC material. An energy spectrum of γ-rays from each material was measured by a Germanium detector. The spectra for G10 and PEEK are shown in Figure 2.17. Since PEEK is an organic thermoplastic polymer, no natural impurities are contained and has little radioactive sources. In addition to radioactivity, the cost, the water-absorbing ratio, the bending modulus, and other factors were carefully investigated, and as a result PEEK is selected as the material of the TPC [21]. The detailed physical properties of PEEK are listed in Table 2.4. The event rate of radioactivity from the TPC made of PEEK is estimated to be (2.2 ± 1.5) cps [20].

2.7.2 Operation gas

As operation gas of the TPC, He and $\mathrm{CO_2}$ are used as ionization gas and quenching gas, respectively. The two gases are known to have relatively small scattering and capture cross sections for a neutron as listed in Table 2.5. Helium gas of 85 kPa and $\mathrm{CO_2}$ gas of 15 kPa are injected in the TPC as the operation gas. A small amount of $^3\mathrm{He}$ gas, ranging from 50 mPa to 200 mPa, is also added to the

Table 2.5: Scattering and capture cross section for a neutron with a nucleus in the TPC operation gas. [26]. The absorption cross section is expressed for a 2200 m/s neutron.

Isotope	Natural abundance	Scattering [barn]	Absorption [barn]
^{3}He	1.4×10^{-6}	6	5333(7)
^{4}He	0.9999986	1.34	0
^{12}C	0.989	5.559	0.00353
^{13}C	0.011	4.84	0.00137
^{16}O	0.99762	4.232	0.0001
^{17}O	0.00038	4.2	0.236
^{18}O	0.002	4.29	0.00016

operation gas for the flux measurement by counting the $^{3}\mathrm{He}(n,\ p)^{3}\mathrm{H}$ events in the TPC.

2.7.3 LiF plate covering

According to the cross section calculation, neutrons in the TPC are scattered by gas molecules with a probability of the order of 1%. Scattered neutrons cause interaction with the TPC wall and produces prompt γ-rays. The γ-rays generate a Compton electrons inside the TPC sensitive region with a probability of about 0.1%. As a result, this background is expected to occur for every 10^{5} incident neutrons in the TPC, which is larger than the neutron beta decay probability ($L/v/\tau_n = 1\ \mathrm{m}/1000\ \mathrm{m/s}/1000\ \mathrm{s} = 10^{-6}$). For suppressing this background, the internal walls of the TPC are completely surrounded by LiF plates, so that no other material can capture scattered neutrons. It is created by mixing LiF and polytetra fluoro ethylene (PTFE) as a sintered body, with the weight composition of 30% and 70%, respectively. ^{6}Li-enriched (90% type and 95% type) Li is used in order to capture a neutron through $^{6}\mathrm{Li}(n,\ \alpha)^{3}\mathrm{H}$ reaction. More than 99.99% of the cold neutron captured by the LiF plate causes this reaction, thus no γ-rays are emitted, although about 0.01% of them are captured with prompt γ-rays. A 200 μm-thick PTFE sheet is attached on the surface of the LiF plates to prevent α rays or tritium ions from emitting inside the TPC sensitive region. With these plates surrounding the TPC wall, the prompt γ-ray production can be suppressed to 10^{-4}. The background amount decreased, therefore, to an order of 10^{-3} for the beta-decay event.

2.7.4 Basic performance of the TPC

The basic performance of the TPC was previously studied using the calibration data [20]. Figure 2.18 shows the avalanche multiplication factor of the TPC as a function of the anode wire voltage. The multiplication factor of about 10^{4} can be obtained in the 50 kPa, 75 kPa, and 100 kPa operation gas pressure. The drift velocity in the TPC is measured using the cosmic rays events passing vertically through the TPC as described in Figure 2.19. The trigger efficiencies of the anode wires were also evaluated by the cosmic rays events. A trigger efficiency of 97% is achieved around the TPC center in the 100 kPa operation gas condition. Because of the non-uniformity of the electric field around the anode wires, the deterioration of the trigger efficiencies near the TPC edges is observed.

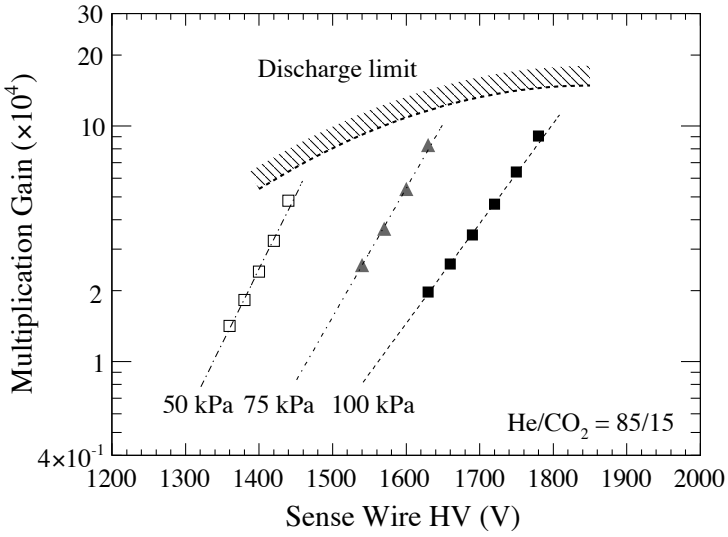

Figure 2.18: Avalanche multiplication factor as a function of the anode wire voltage [20]. The results with an operation gas pressure of 50 kPa, 75 kPa, and 100 kPa are plotted while the gas composition is maintained as He:CO_2=85:15. The discharge limit line is empirically obtained.

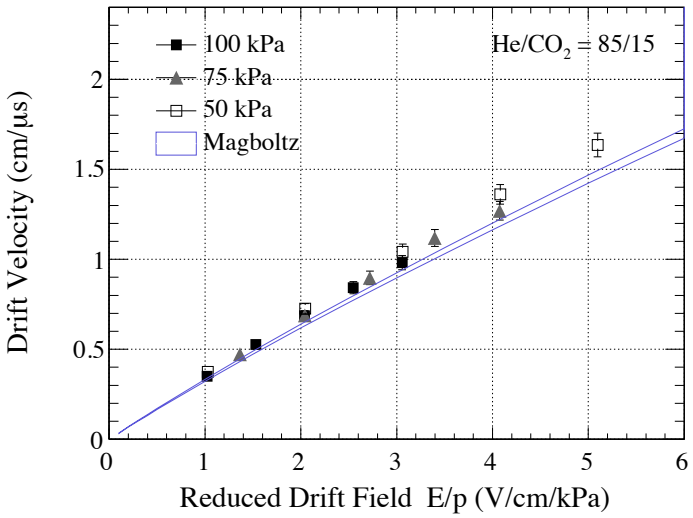

Figure 2.19: Drift velocity of electrons in the TPC as a function of the reduced drift field strength [20]. The velocity calculated by the Magboltz software [27] is also drawn.

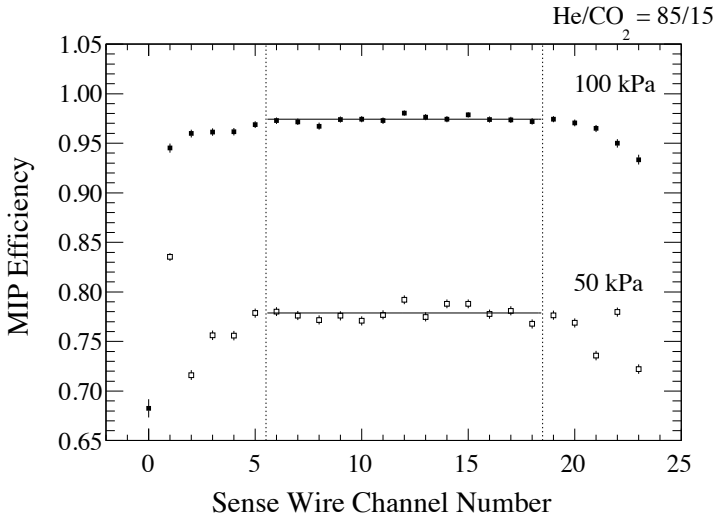

Figure 2.20: Anode wire trigger efficiency for the minimum ionization particles [20]. Under the 100 kPa gas condition, the averaged wire efficiency of 97% is achieved in the TPC center region.

The three dimensional charged track in the TPC can be reconstructed using the anode and cathode wire waveforms. The typical event displays of the beta-decay and $^3\mathrm{He}(n,\ p)^3\mathrm{H}$ events are shown in Figure 2.21. The energy deposit distributions in the three planes (x-y, y-z, and z-x planes) are drawn. Note that the absolute y position of the track cannot be determined because the trigger timing is not recorded. The clear track can be seen for the beta-decay events, while the large energy deposit is localized for the $^3\mathrm{He}(n,\ p)^3\mathrm{H}$ events.

2.8 Preamplifier

Every waveform of anode, field, and cathode wires, is amplified by a charge-sensitive preamplifier shown in Figure 2.22. All of the preamplifiers are installed at the top of the TPC. The circuit diagram of the preamplifier is shown in Figure 2.23. The amplification factor can be varied by changing the R_0 and R_1 resistances. Two types of preamplifiers with different amplification factors are used in this experiment. For cathode wires in the low plane and anode wires, $R_0 = \infty$ (disconnected) and $R_1 = 0\ \Omega$, and the amplification factor is observed to be 1.3 V/pC. For cathode wires in the high plane and field wires, $R_0 = 300\ \Omega$ and $R_1 = 1\ \mathrm{k}\Omega$, and the amplification factor is observed to be 0.23 V/pC. The linearity of the preamplifier output with respect to the input charge is confirmed up to an output voltage of 3.3 V. A typical output waveform of the preamplifier is shown in Figure 2.24.

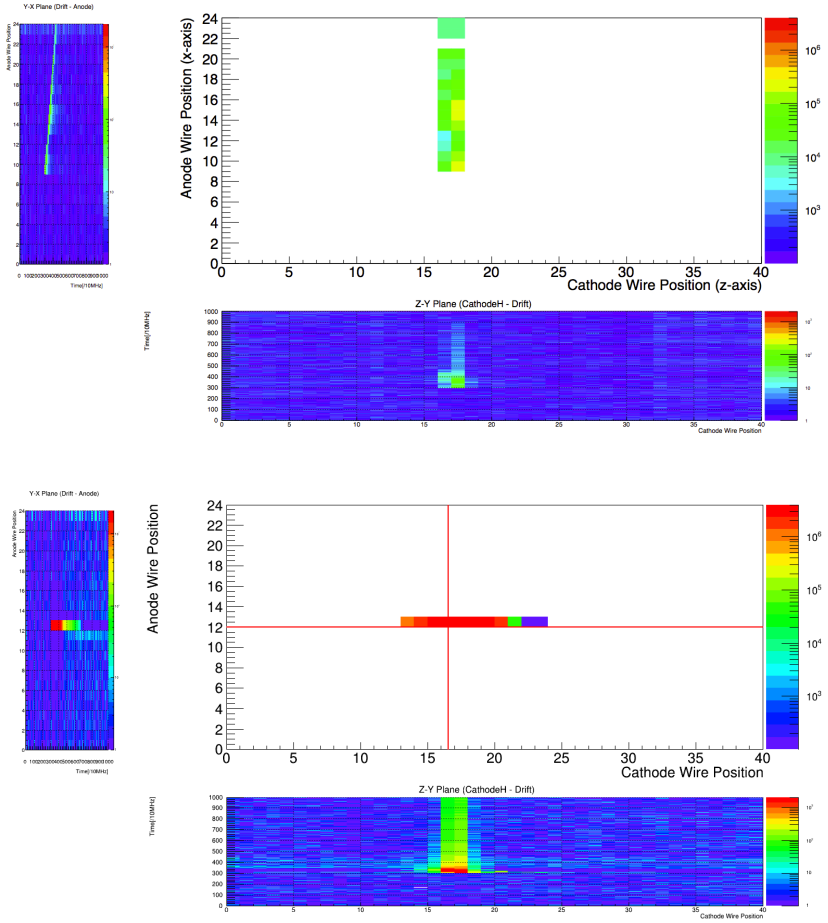

Figure 2.21: Typical event display of the beta-decay (top) and $^{3}\mathrm{He}(n,\ p)^{3}\mathrm{H}$ (bottom) events.

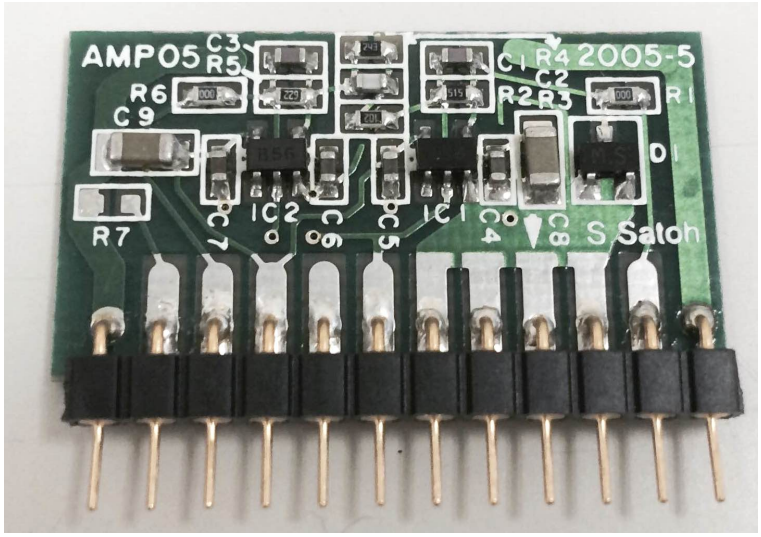

Figure 2.22: Picture of a preamplifier [21].

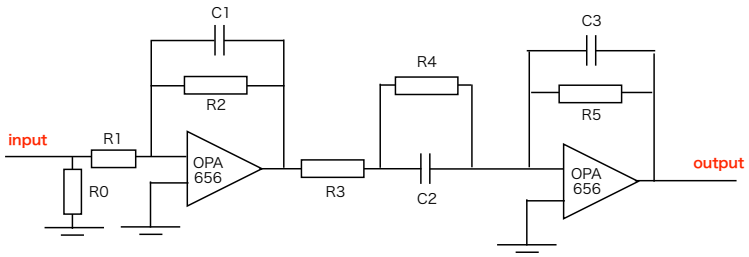

Figure 2.23: Preamplifier circuit. The multiplication factor is adjustable by changing R_0 and R_1 values.

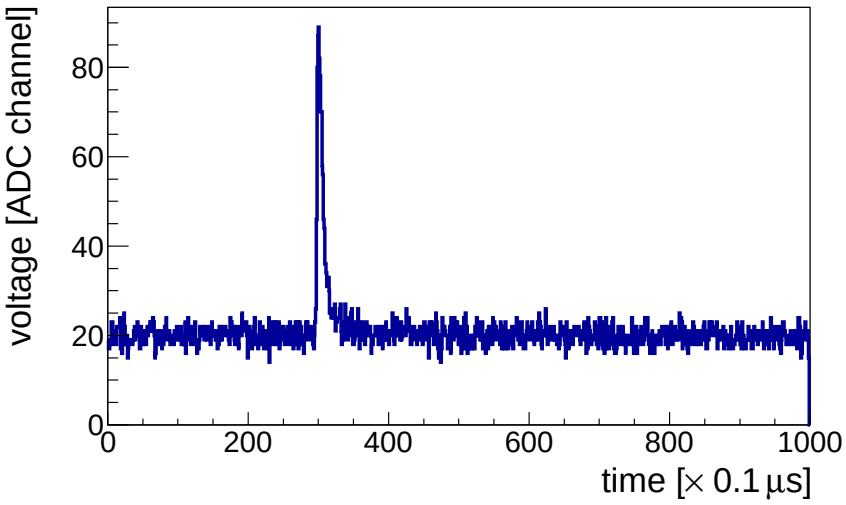

Figure 2.24: Typical preamplifier output waveform. The trigger timing is adjusted to be 30 μs in the time window.

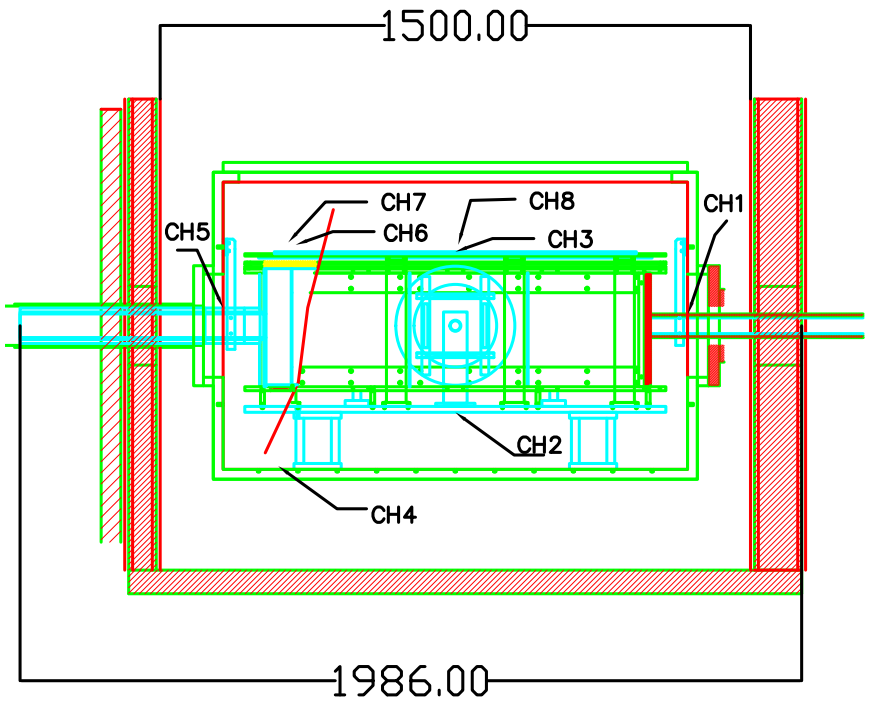

Figure 2.25: Installing position of the eight LakeShore thermometers inside the vacuum chamber.

2.9 Temperature monitoring

The temperature around the TPC is monitored by platinum thermometers, by measuring the resistivity of the platinum using a four-terminal method. Fourteen thermometers with two different types of systems, manufactured by Automatic Systems Laboratories and LakeShore, are used to monitor the TPC temperature. Their measuring uncertainties are 60 mK at 298 K and 105 mk at 300 K, respectively. The detailed specifications of the two types of thermometer systems are listed in Appendix B. Figure 2.25 shows the position of the eight LakeShore thermometers inside the vacuum chamber. As shown in Figure 2.26, the temperature inside the TPC during the lifetime measurement increases with the elapsed time. This is due to the heat produced by the preamplifiers, and a temperature increase of typically 5 to 10 degrees is observed.

2.10 Data acquisition system

The schematic diagram of the fast data (TPC signal, veto counters, kicker pulse signal) acquisition system in this experiment is shown in Figure 2.27. Signals of the TPC and the cosmic ray veto counters are recorded by the Front-end INstrumentation Entity for Sub-detector Specific Electronics (FINESSE) modules in the COmmon Pipelined Platform for Electronics Readout (COPPER) Lite system [28]. On 5 COPPER Lite boards, 16 FINESSE ADC modules and 2 FINESSE TDC modules are implemented. The detailed specifications of the ADC and TDC modules are listed in Table

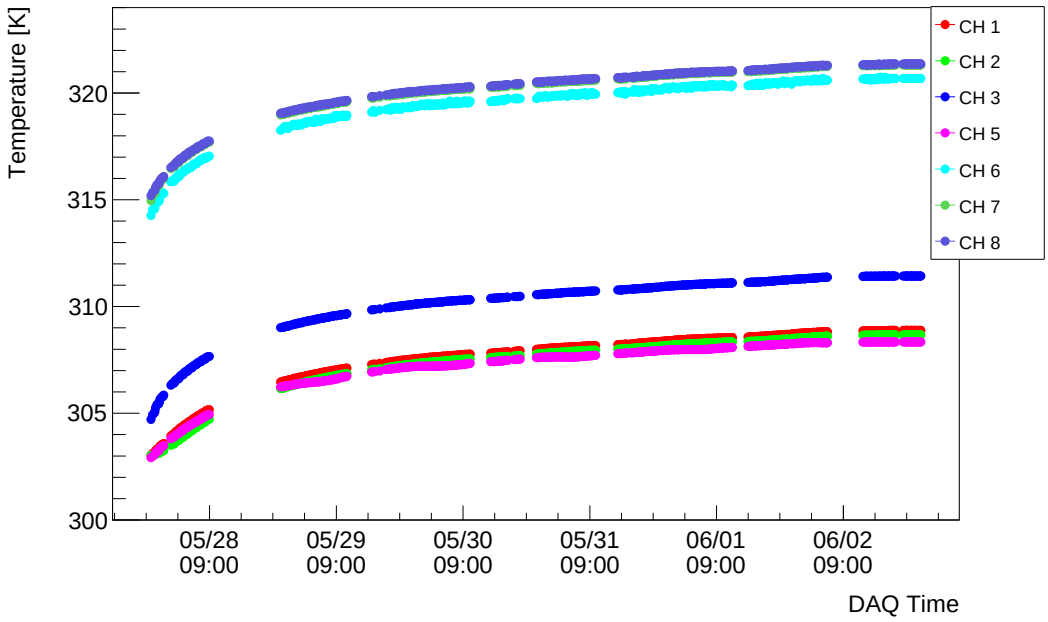

Figure 2.26: Temperature inside the TPC during the lifetime measurement. CH6, CH7, and CH8 thermometers are installed close to the preamplifiers, which shows higher temperatures than others.

2.6 and 2.7, respectively. Waveforms of 24 anode wires, 24 field wires, 40×2 cathode wires are digitized by the ADC module. The signal timing of TPC wires, veto counters, and a kicker pulse, which represents the time of producing the neutron beam, are respectively digitized by the TDC modules. The digitized data by the ADC and TDC is sent to a computer through ethernet cables.

The trigger signal for taking the fast data is sent to the five COPPER Lite boards when any of 24 anode wires in the TPC exceeds a threshold voltage of 20 mV. The threshold level corresponds to a 200 eV energy deposit in the TPC. Once a trigger signal is accepted, each of the five COPPER Lite boards independently sends all of the digitized data to the computer. During the data transfer time, which is typically 100 μs, the COPPER Lite modules output a busy signal and additional trigger signal is rejected. The trigger signal is also vetoed for 70 μs when any of 7 sets veto counters coincided with the TPC signal, in order to avoid triggering cosmic ray events. At the 300 kW accelerator operation, the typical trigger event rates are 10 cps in the shutter-open mode, and 5 cps in the shutter-closed mode, respectively. For the drift velocity calibration, cosmic rays data is taken as a data acquisition cycle, in which the coincidence of TPC signal and any of 7 sets veto counters signal is required as a data acquisition trigger (see Section 3.2 for the data acquisition cycle and its trigger rate).

Aside from fast data acquisition, the TPC condition, such as gas pressure, temperature, and wire and electrode voltages are monitored on a continuous basis during the lifetime measurement. The TPC gas pressure is measured every 7 seconds by a transducer pressure gauge (Mensor gauge) with an accuracy of 0.01%. As described in Section 2.9, the TPC temperature is monitored by fourteen thermometers, whose data is recorded and sent to a computer every 11 seconds. The high voltages applied for the anode wires and the drift field electrode are also monitored during the measurement,

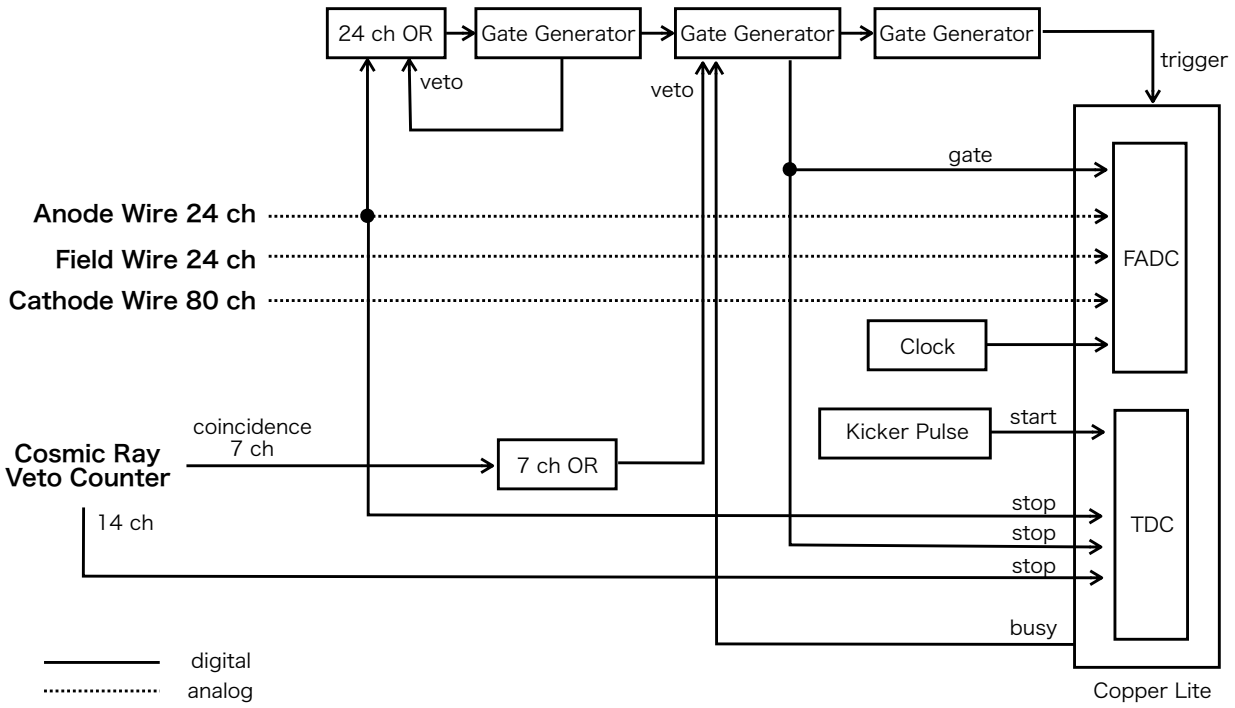

Figure 2.27: Schematic diagram of the DAQ circuit for the physics data acquisition. ADC and TDC operating in the COPPER Lite system [28] are used for taking the data. Wire waveforms of the TPC are recorded by the flash-ADC (FADC), and timing of waveforms, kicker pulse, and cosmic ray veto counters are recorded by the TDC.

Table 2.6: Specification of the Finesse ADC module.

Model	GNV-440 FINESSE 8CH ADC BOARD
Resolution	12 bits
Sampling clock frequency	10 MHz (external input)
Dynamic range	2 V peak to peak
Data size	10 bit
Input channel	8
Dimensions	76 mm $\times$ 186 mm

Table 2.7: Specification of the Finesse TDC module.

Model	FINESSE 32CH MULTI HIT TDC V2
Sampling clock frequency	125 MHz
Dynamic range	$\pm$131 μs from trigger timing
Input channel	32
Dimensions	76 mm $\times$ 186 mm

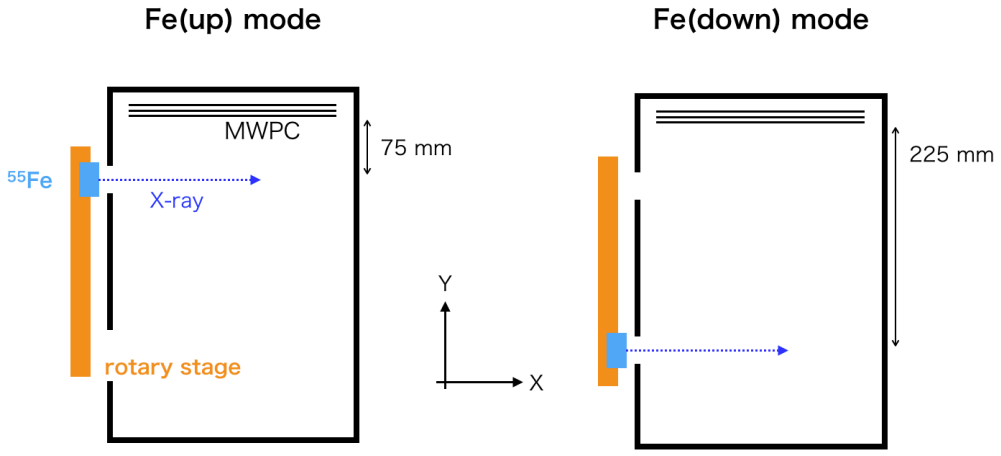

Figure 2.28: Schematic view of the calibration measurement setup. The calibration source (^{55}Fe) is attached to a rotary stage, enabling to change the height of the source. The drift length of electrons is 75 mm for Fe (up) mode and 225 mm for Fe (down) mode.

and an alert signal is produced when each of the voltage fell below a threshold voltage.

2.11 Calibration system

This section describes the energy, drift velocity, and dead time calibration system for the TPC.

2.11.1 Energy calibration

The multiplication factor of the TPC during the measurement is monitored using a ^{55}Fe X-ray source. The K_α and K_β X-ray, the energies of which are 5.86 keV and 6.45 keV, respectively [29], are emitted from the ^{55}Fe source. The X-ray causes a photoelectric effect with the TPC gas molecules, and the total energy is observed as the kinetic energy of a photoelectron by the TPC. The source is attached to a rotary stage located close to the TPC side wall, making it possible to selectively change the height of the source position. The drift length of an electron is 75 mm in the Fe (up) mode, while 225 mm in the Fe (down) mode as shown in Figure 2.28. The X-ray is limited within 20 mrad in the vertical direction by a collimator.

A set of Fe (up) and Fe (down) data is taken every hour during the measurement, in order to monitor the multiplication factor of the TPC. A typical transition of the energy peak position for Fe (up) and Fe (down) mode is shown in Figure 2.29. The gas deterioration from outgas causes an exponential reduction of the multiplication factor. Once the operation gas is pumped out for a while and new gas is filled in the TPC, the energy peak position completely recovers. By comparing the energy peak position between the two setups, the attenuation effect for an electron to drift 150 mm can be evaluated as a function of time. The attenuation length λ can be expressed as

$$\lambda = \frac{225\ \mathrm{mm} - 75\ \mathrm{mm}}{\log(E_{\mathrm{up}}/E_{\mathrm{down}})}, \tag{2.4}$$

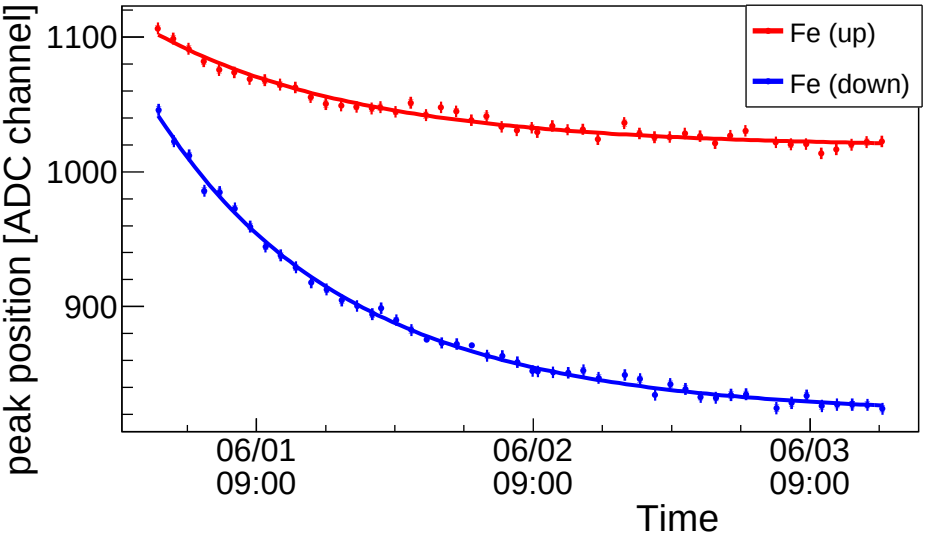

Figure 2.29: Typical transition of the energy peak position after gas filling. The red and blue points show the result at Fe (up) and Fe (down) modes, respectively. Each of the data points is fit by an exponentially-decaying function.

where E_{up} and E_{down} represent the peak positions in the Fe (up) and Fe (down) modes, respectively. The average attenuation length evaluated using Eq. (2.4) is about 2000 mm, corresponding to 7% attenuation for an electron to drift 150 mm. Using this result, the energy calibration is conducted as a function of time, correcting for the attenuation effect. The attenuation becomes significant one week after filling the gas, thus the operation gas is changed on a weekly basis in average during the beam time.

2.11.2 Drift velocity calibration

The drift velocity of an electron inside the TPC is evaluated using cosmic ray events passing vertically through the TPC. Such an event has a different rise time of waveforms among anode wires, originating from the drift time of an electron. The difference between the fastest and the slowest rise time T_{drift} corresponds to the drift time of the TPC length in the y direction ($h \sim 30$ cm). However, the effective length becomes $h - \Delta h$, where the correction length Δh can be expressed using the number of hit anode wires (n) as $\Delta h = h/n$ (see Figure 2.30). With this correction, the

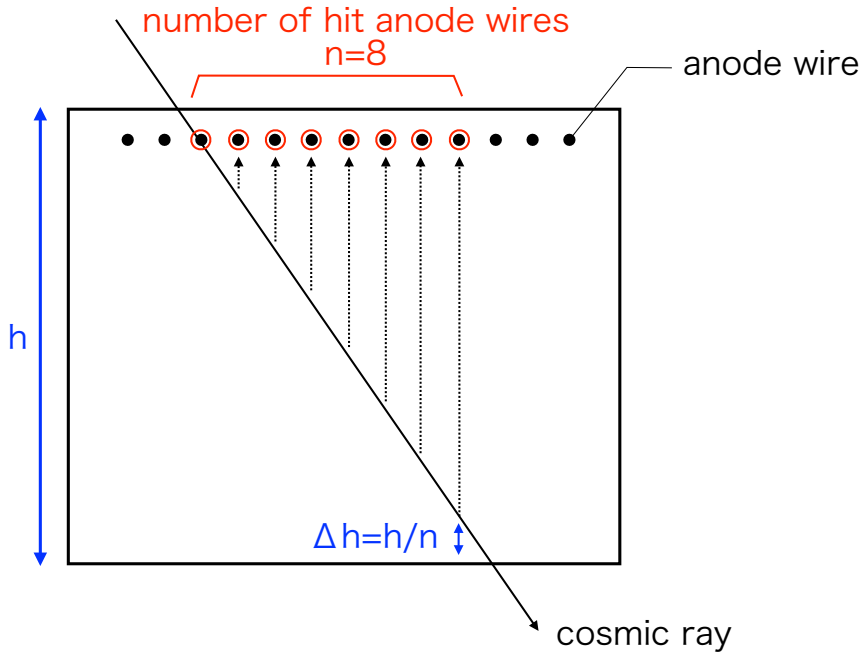

Figure 2.30: Cross section of the TPC for a cosmic-ray event describing the drift length correction of Eq. (2.6). The maximum drift length of electrons among the anode wires (the rightest anode wires among 8 hit anode wires in the figure) becomes $h - \Delta h$, where Δh is expressed as h/n.

drift velocity v_n can be expressed as

$$v_n = \frac{h}{T_{\rm drift}} \tag{2.5}$$

$$= \frac{(h-\Delta h)\left(1+\frac{\Delta h}{h-\Delta h}\right)}{T_{\rm drift}} \tag{2.6}$$

$$= v_0\left(1+\frac{h/n}{h-h/n}\right) \tag{2.7}$$

$$= \frac{v_0}{1-1/n} \tag{2.8}$$

Hence, by fitting v_n as a function of n using the function in Eq. (2.8), the modified drift velocity of an electron v_0 can be evaluated as shown in Figure 2.31. Since the drift velocity depends on the operation gas composition, the drift velocity calibration is conducted for each gas. The typical drift velocities v_0 are evaluated to be 1.0 cm/μs.

2.11.3 Dead time calibration

As described in Sec 2.10, the data acquisition system vetoes the trigger signal under two conditions: (A) the data transfer time (typically 100 μs per trigger), (B) veto counters signal coincides with that of anode wires (70 μs). During this dead time, no event in the TPC is recorded even if it happens,

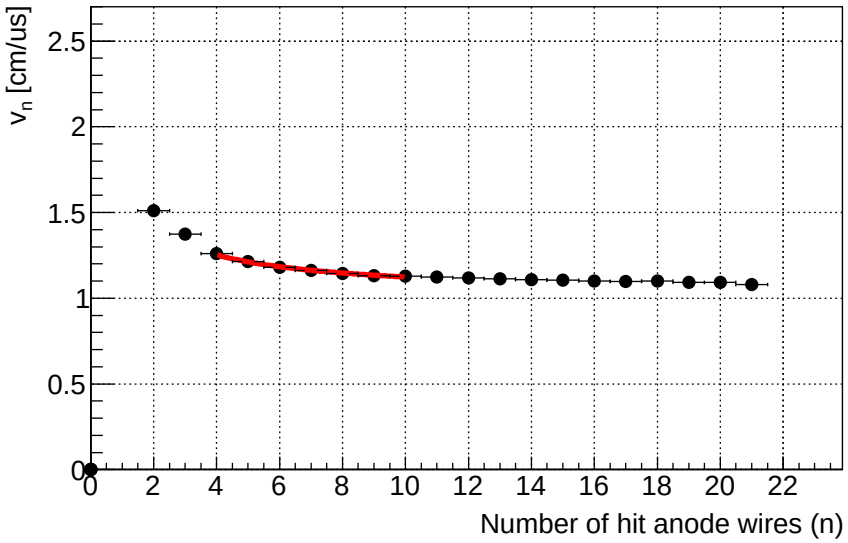

Figure 2.31: Drift velocity (v_n) distribution as a function of the number of hit anode wires (n). The points are fit by the $v_0/(1-1/n)$ function to evaluate the modified drift velocity (v_0).

which affects the event rate of the signal and background events. Thus an accurate calibration process for dead time is necessary to evaluate the accurate event rate of signal and background events. The calibration is processed as a function of TOF, because both (A) and (B) components have TOF dependence.

The dead time calibration is conducted according to the following procedure. Let's assume i represents a neutron pulse identification number ($1 \leqq i \leqq N$; N is the number of total neutron pulses).

1. The dead time flag of i-th neutron pulse $d_i\ (t_{\mathrm{TOF}})$ is 1 when the veto function works at the TOF of t_{TOF}. That is to say,

$$d_i\ (t_{\mathrm{TOF}}) = \begin{cases} 1 & (t_i^{\mathrm{start}} \leqq t_{\mathrm{TOF}} \leqq t_i^{\mathrm{end}}) \\ 0 & (\mathrm{otherwise}) \end{cases},$$

   where t_i^{start} and t_i^{end} represent the start and end timing of the dead time in the i-th neutron pulse, respectively.

2. The dead time ratio $D\ (t_{\mathrm{TOF}})$ is evaluated as

$$D\ (t_{\mathrm{TOF}}) = \frac{1}{N}\sum_{i=1}^{N} d_i(t_{\mathrm{TOF}}). \tag{2.9}$$

3. The live time ratio $L\ (t_{\mathrm{TOF}})$ as defined as

$$L\ (t_{\mathrm{TOF}}) = 1 - D\ (t_{\mathrm{TOF}}). \tag{2.10}$$

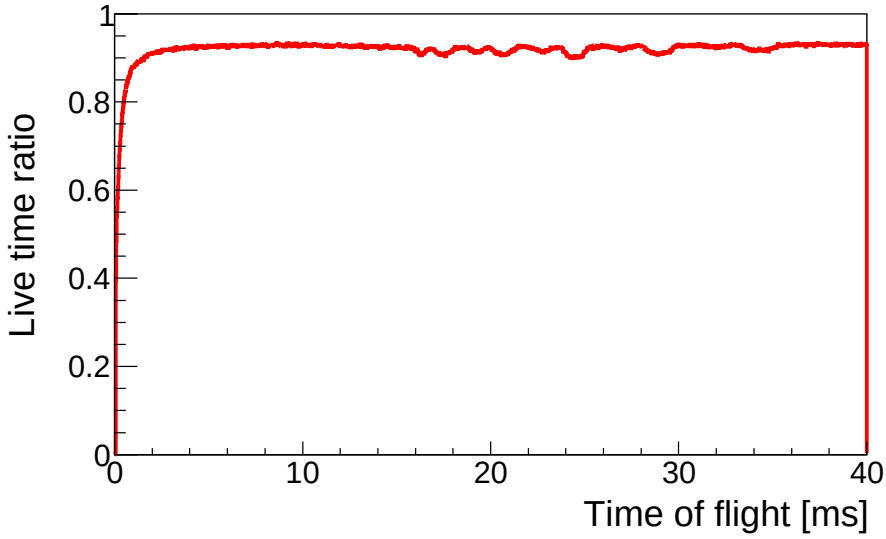

Figure 2.32: Live time ratio (L) of the data acquisition system in the shutter open mode. Hollows originating from neutron bunches (15 ms $< t_{\mathrm{TOF}} <$ 35 ms) and the neutron beam production (t_{TOF} ∼0 ms) are observed.

4. The corrected event rate at t_{TOF}, expressed as $R\left(t_{\mathrm{TOF}}\right)$, is obtained by multiplying the inverse of $L\left(t_{\mathrm{TOF}}\right)$ by the observed event rate $R^0\left(t_{\mathrm{TOF}}\right)$ as

$$R\left(t_{\mathrm{TOF}}\right) = R^0\left(t_{\mathrm{TOF}}\right) \times \frac{1}{L\left(t_{\mathrm{TOF}}\right)}. \tag{2.11}$$

Figure 2.32 shows the $L\left(t_{\mathrm{TOF}}\right)$ distribution in the shutter-open mode. Since a lot of background events are produced as prompt γ-rays the moment when a neutron beam is generated, $L\left(t_{\mathrm{TOF}} \sim 0ms\right)$ becomes smaller. Several hollows originating from 5 neutron bunches, at around 15 ms $< t_{\mathrm{TOF}} <$ 35 ms, are also observed in the plot. The average of the live time ratio is about 93%.

2.12 Gas handling system

The operation gas described in Section 2.7.2 is injected into the TPC through the SUS-based gas handling system located at the BL05 beamline. The schematic diagram of the gas handling system is shown in Figure 2.33. Every region and valve in the system is named as I1, I2,..., and V1, V2,..., respectively. The vacuum chamber housing the TPC is expressed as ITPC in the figure. Helium and CO_2 gas cylinders are connected with the I1 region, while a ^{3}He gas cylinder is stored at the I6 region. Two Mensor pressure gauges are connected at Im region, whose full scales are 120 kPa and 35 kPa, respectively. The Pfeiffer pressure gauge, the full scale of which is 1.3 kPa, is connected with I6 region for low-pressure measurement. The detailed specification of the pressure gauges is listed in Table 2.8 and 2.9. The Automatic Systems Laboratories platinum thermometer is attached to a surface of I1 SUS tube to measure gas temperature. A rotary pump and a turbo molecular pump (TMP) are attached to the I1 region to pump out the gas.

Table 2.8: Specification of the Mensor pressure gauge.

Model	Mensor CPG2500
Full scale	120 kPa(chA), 35 kPa(chB)
Precision	Max(0.01% of measured value, 6 Pa) for chA, 3.5 Pa for chB
Sensor volume	5 cc
Sensor temperature	5 K larger than environmental temperature

Table 2.9: Specification of the Pfeiffer pressure gauge.

model	690A11TRA
full scale	1333 Pa
precision	0.06% of measuring pressure + 25 mPa

As the operation gas, ^{3}He, ^{4}He, and CO_2 gases are injected into the TPC in this order through this gas handling system. At first, ^{3}He gas is expanded from I6 to Im, and after measuring the pressure (a few kPa) by the Mensor gauge, it is expanded to ITPC. Next, ^{4}He gas is made to flow directory into the TPC, with V1, V9 and VTPC valves open and others closed. After waiting 10 minutes for the gas to approach equilibrium, the ^{4}He pressure is measured by Mensor gauge, and CO_2 gas is injected into the TPC by the same procedure. It took approximately one hour to fill the three gases into the TPC.

2.13 Mass spectrometer

The isotopic contamination in a helium gas cylinder is required to be measured for evaluating ^{3}He number density in the TPC. The contamination ratio for a typical helium gas cylinder is known to be 0.1 ppm, which corresponds to about 10% of the total ^{3}He number density in the TPC. The contamination ratio is precisely measured by a dual-type mass spectrometer (VG5400) at the University of Tokyo [30]. A picture of the mass spectrometer is shown in Figure 2.34. A sampled gas from a helium gas cylinder is attenuated to an order of 10^{-5} Pa and injected into the ion source region. The gas is ionized and accelerated, and ^{3}He and ^{4}He ions are separated by the bending region where a magnetic field is applied in the vertical direction. As ion detectors, the spectrometer has a Faraday cup for a ^{4}He ion and a multiplication counter for a ^{3}He ion, respectively. The number of both ^{3}He and ^{4}He ions can be counted simultaneously. The detail of the ^{3}He/^{4}He ratio measurement is described at Section 5.4.

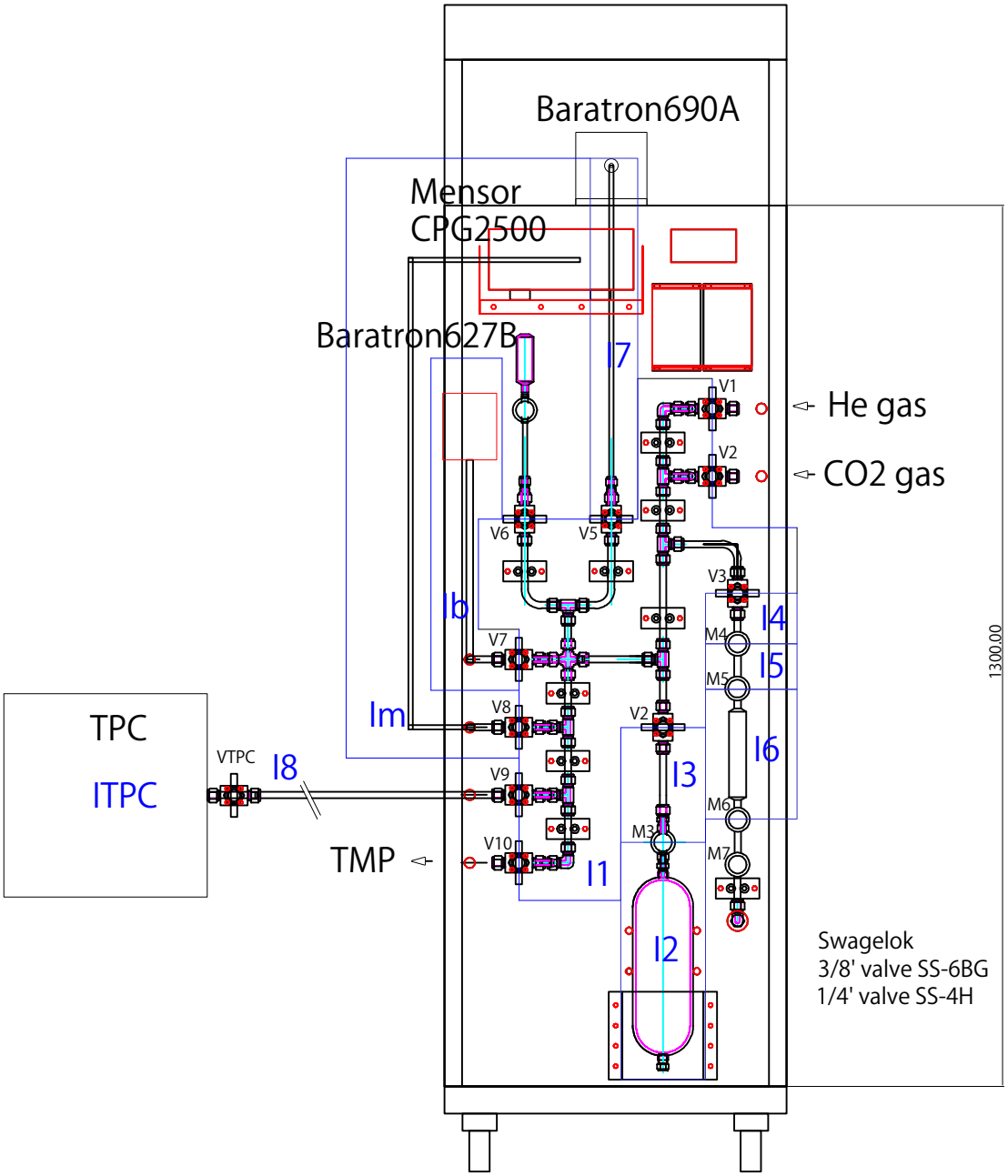

Figure 2.33: Schematic diagram of the gas handling system. Helium, CO_2 and ^3He gases are injected into the TPC using this system.

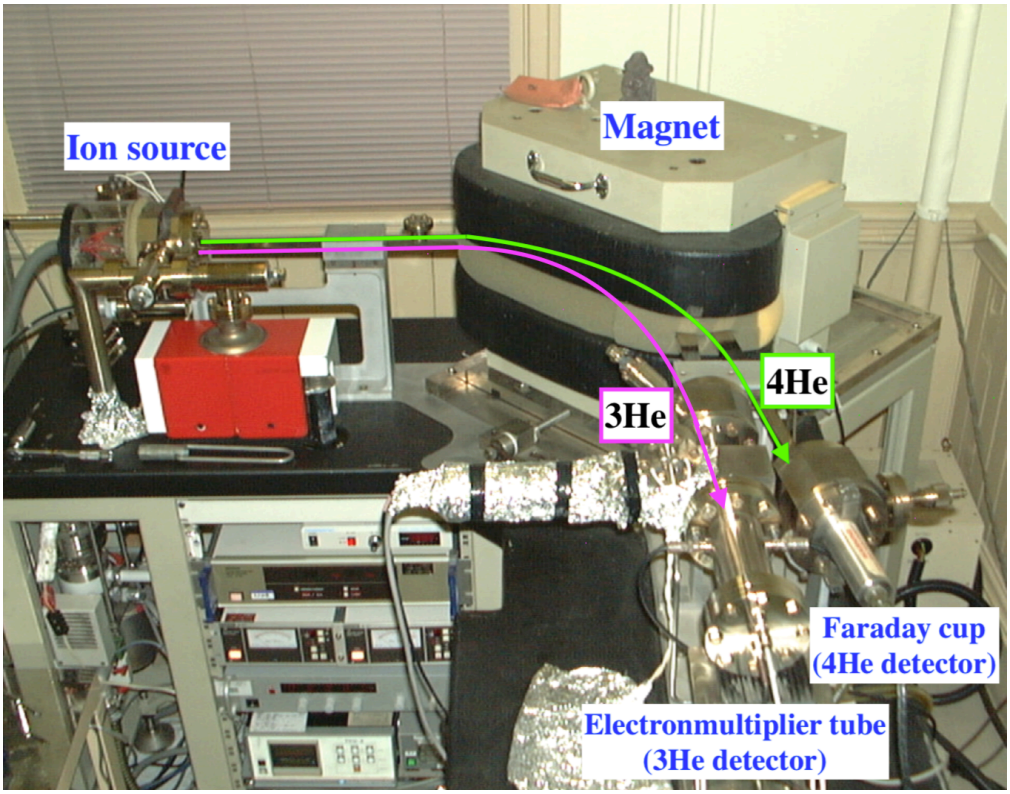

Figure 2.34: Picture of the mass spectrometer [30] at the University of Tokyo. As indicated by the two arrows, the ^{3}He and ^{4}He ions can be separated by the magnet and counted simultaneously.

Chapter 3

Data acquisition cycle and data quality

This chapter describes the data acquisition cycle for the lifetime measurement from 2014 to 2018. During the four years, some of the experimental setup changed as described in Section 3.3. The data quality analysis in comparison with the different hardware condition is of great significance to guarantee our analysis, which is discussed in the last part of this chapter.

3.1 Acquired physics data

We started taking the physics data to evaluate τ_n in 2014, and continued until 2018. Table 3.1 shows the acquired data set. We took the data with 20 sets of operation gas conditions. The detailed measurement condition of each gas ID is described in Table 3.3. The accelerator operation power decreased from 500 kW to 200 kW in 2015 due to a target problem in MLF. In total, we obtained 960 hours (40 days) beam-incident data, and 6.0×10^{11} neutrons entered the TPC. The first result of this experiment was presented by S. Ieki using the data between 2014 and 2016 [31]. All-combined neutron beam fluence in Table 3.1 is 3.6 times more than the data used in the first result.

3.2 Data acquisition cycle

The data acquisition cycle during the lifetime measurement is listed in Table 3.2. The data with the neutron beams is taken in two multiplication gain modes. At the normal-gain mode, 1720 V is applied and the avalanche multiplication gain corresponds to 10^4. At the low-gain mode, 1200 V is applied and the avalanche gain is 10^2.

Table 3.1: Physics data set

Period	Start	End	Gas ID	Operation power [kW]	Open [hour]	Open [run]	Closed [run]	Calibration [run]	Neutrons entering TPC [$\times 10^{11}$]
2014A	2014/5/27	2014/6/3	42	300	34	126	119	349	0.2
2015A	2015/4/26	2015/5/4	53	500	16	57	59	105	0.2
2016A	2016/4/16	2016/6/14	63-66	200	224	825	788	1222	1.2
2017A	2017/5/28	2017/6/28	83-89	150	172	517	517	792	0.6
2017B	2017/11/21	2018/3/22	94-101	300, 400	514	1644	1509	2404	3.9
Combined					960	3169	2992	4872	6.0×10^{11}

Table 3.2: List of data acquisition cycle

Gain	Mode	Time [s]	Neutron shutter	Trigger condition	Trigger rate [cps]
normal	open	1000 or 1200	open	TPC hit without cosmic veto counters hit	10
	closed	1000 or 800	closed	TPC hit without cosmic veto counters hit	5
	Fe (up)	100	closed	TPC hit without cosmic veto counters hit	40
	Fe (down)	100	closed	TPC hit without cosmic veto counters hit	40
	cosmic	100	closed	TPC and cosmic veto counters hit coincidence	50
low	open	1000 or 300	open	TPC hit without cosmic veto counters hit	4
	closed	1000 or 300	closed	TPC hit without cosmic veto counters hit	0.2

The purpose of taking each data in Table 3.2 is described in the following.

- Normal gain / shutter open
  measuring the neutron beta-decay and $^3\mathrm{He}(n,\ p)^3\mathrm{H}$ events for evaluating τ_n.

- Normal gain / shutter closed
  evaluating the background flux without the presence of the neutron beam.

- Normal gain / Fe (up), Fe (down)
  detecting 5.9 keV monochromatic X-rays for the TPC energy calibration. The source position is changed in two ways for monitoring the attenuation effect.

- Normal gain / cosmic
  detecting cosmic rays for the drift velocity calibration inside the TPC.

- Low gain / shutter open
  measuring the $^{14}\mathrm{N}(n,\ p)^{14}\mathrm{C}$ background amount with respect to the $^3\mathrm{He}(n,\ p)^3\mathrm{H}$ event. In this mode, the $^{14}\mathrm{N}(n,\ p)^{14}\mathrm{C}$ and $^3\mathrm{He}(n,\ p)^3\mathrm{H}$ peaks can be clearly separated in the energy deposit distribution.

- Low gain / shutter closed
  evaluating the background event in the low-gain measurement.

3.3 Device conditions during the measurement

During the four-years data taking time, the hardware conditions was changed as described in Table 3.3. The hardware setup conditions were changed mainly at the interval of the data acquisition period. For example, the TPC alignment is found to be off the correct position after 2017. This is because the TPC was temporarily taken out from the beamline for the performance measurement, and realigned at the beamline in the year. The TPC position directly affects the beam profile distribution in the TPC, which leads to the variation of the event selection efficiencies.

Table 3.3: List of experimental setup condition. A single capital letter in the table means the setup had not changed during the period.

Fill number	42	53	63 64 65 66	83 84 86 87 88 89	94 95	96 97 98 99 100 101
Year	2014A	2015A	2016A	2017A	2017B	
Beam power [kW]	300	500	200	150	300	400
Target type	#2				#8	
G1 helium cylinder	#6	#7	#8	#10	#11	
Calibration source	#1			#2		
Beam monitor position	A	B	C D	E		
LiF guide position	A	B	C	D		
TPC alignment	A			B		
Proton bunch mode	double bunch					single bunch
BL06-side Fe shield	no shield	shield				
Low-divergence beam branch	?	closed			almost open	
Vacuum condition	not bad	good	bad		not bad	
DAQ time (open, closed) [s]	1000, 1000		1200, 800	1200, 800	1000, 1000	mix 1200, 800
TDC module	old	new				

3.4 Gain deterioration with the elapsed time

The attenuation effect of a drifting electron in the TPC is estimated using the calibration source data as described in Section 2.11.1. As Figure 3.1 shows, the attenuation coefficient gradually grows with the elapsed time after the gas filling time, due to outgas from the material inside the vacuum chamber. The attenuation effect is empirically known to be in equilibrium at a coefficient of about 1.5 m^{-1}.

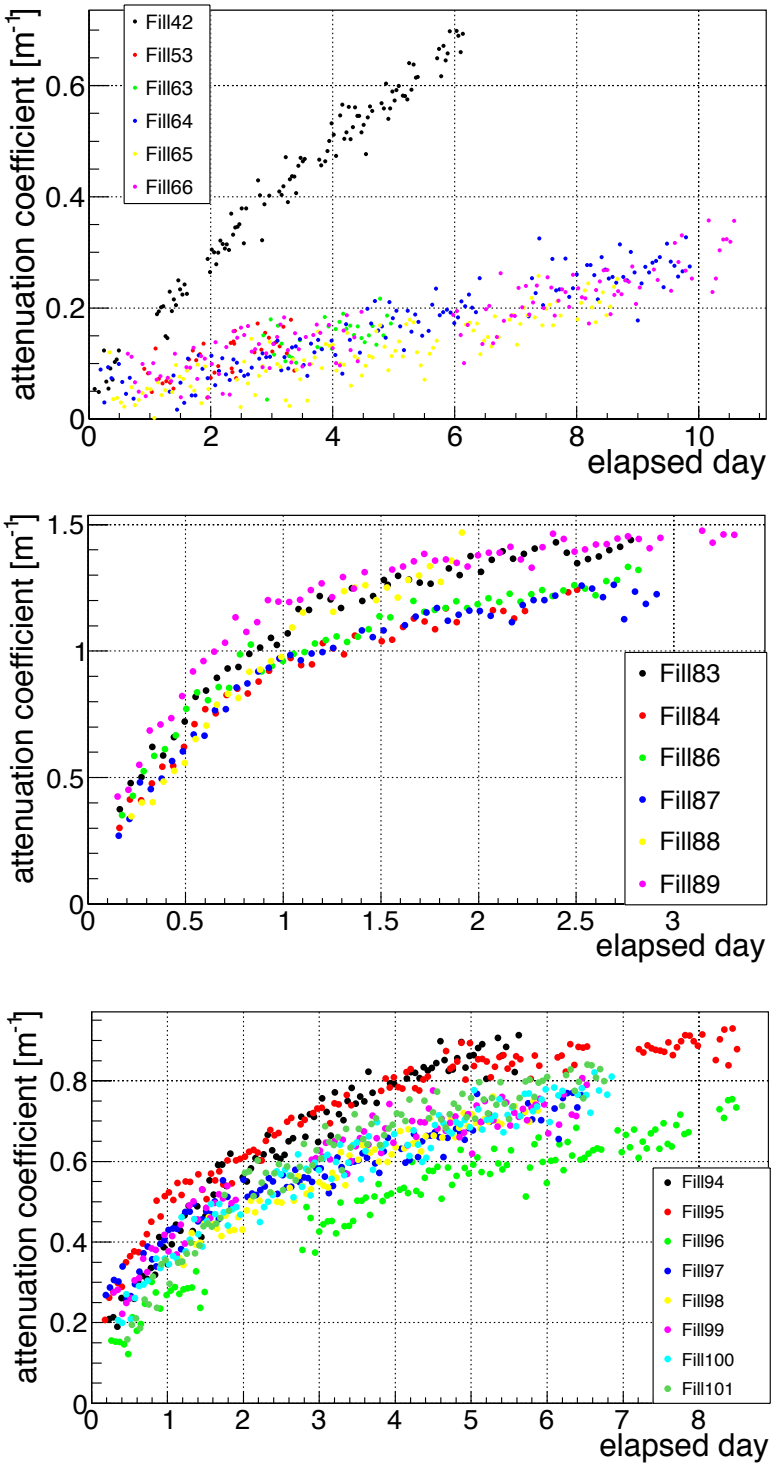

Figure 3.1: Growth of the attenuation coefficient in the TPC as a function of the elapsed day after the gas filling time: (top) 2014A∼2016A, (middle) 2017A, (bottom) 2017B.

Chapter 4

Simulation

This chapter describes the detail of the simulation framework. The Monte Carlo simulation of our detector system is constructed based on the Geant4 simulation framework [32] [33] [34]. In this simulation, the output waveforms of the anode, field and cathode wires are simulated. The event selection procedure, described in Chapter 5, is applied to the waveforms in order to evaluate signal selection efficiencies for evaluating the ε_β and $\varepsilon_{^3\mathrm{He}}$ parameters in Equation (1.27). The result is also used to estimate the background amount in the signal region.

4.1 Overview of simulation process

Figure 4.1 shows the overall procedure of the Monte Carlo simulation. It is divided into two processes: the particle simulation and the detector response simulation processes. At the particle simulation framework, the detector setup at the BL05 polarization beam branch is implemented, such as plastic scintillation counters, the lead shield, the beam pipes, and the LiF plates. The TPC structure made of PEEK and LiF plates is also faithfully reproduced. A schematic view of the setup construction in the simulation framework is shown in Figure 4.2. Particle transportation and ionization process in the TPC is simulated by the Geant4 simulation, and the corresponding energy deposit from a charged particle is calculated as a function of its position. Note that the time information is not used at the simulation procedure. The physics model of Bertini Cascade "FTFP_BERT_PEN" (Fritiof with Precompound, Bertini Cascade, Penelope model) is used for the interaction model.

The energy deposit calculated at the particle simulation process is converted into the wire waveforms in the detector simulation process. In this process, the induced current and the space charge effect at the avalanche multiplication as well as recombination and attenuation during the drift are implemented. A template waveform and the noise level are evaluated based on the experimental waveforms. The event selection algorithm, which is the same as the one used in the experimental data, is applied to the simulated waveforms.

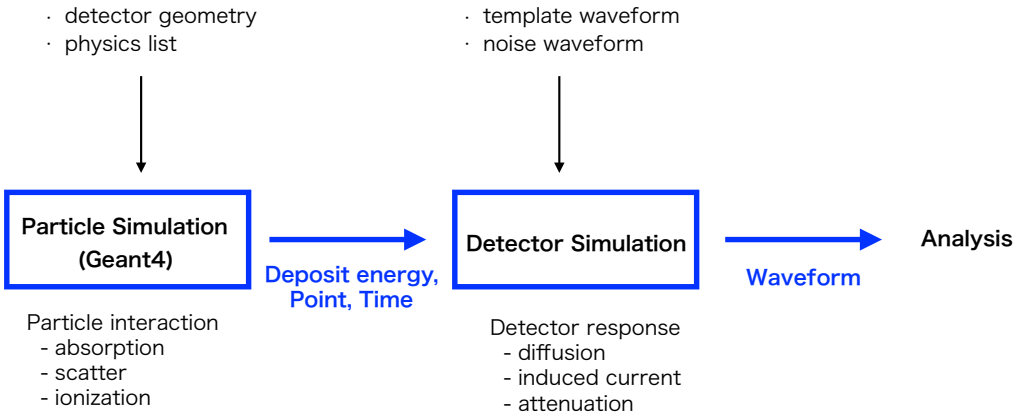

Figure 4.1: Simulation flow.

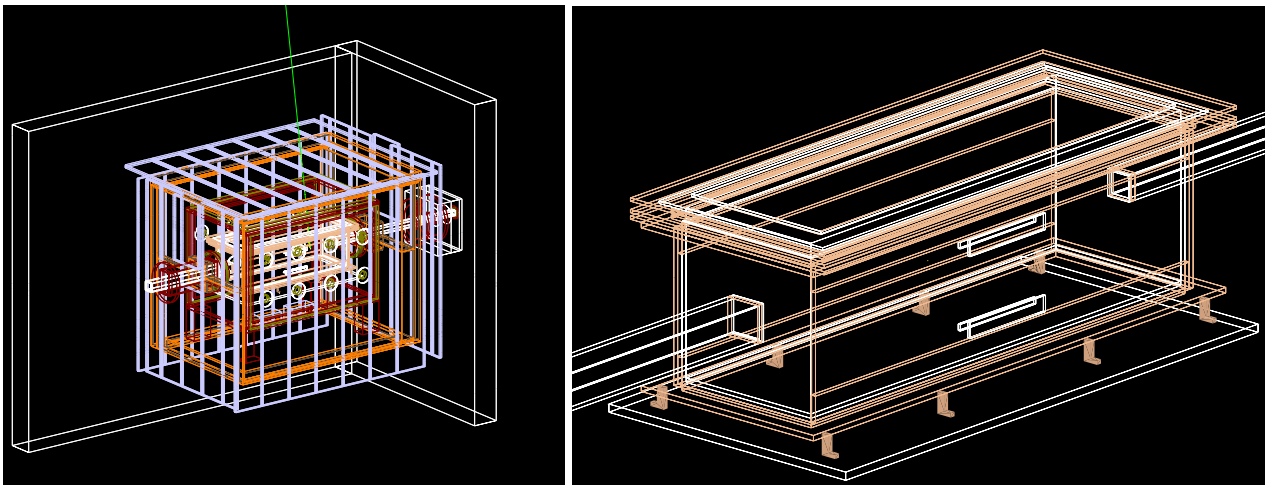

(a) Overall detector setup. (b) TPC structure.

Figure 4.2: Schematic view of the detector setup constructed at the Geant4-based Monte Carlo simulation system: (a) overall detector setup, (b) TPC structure.

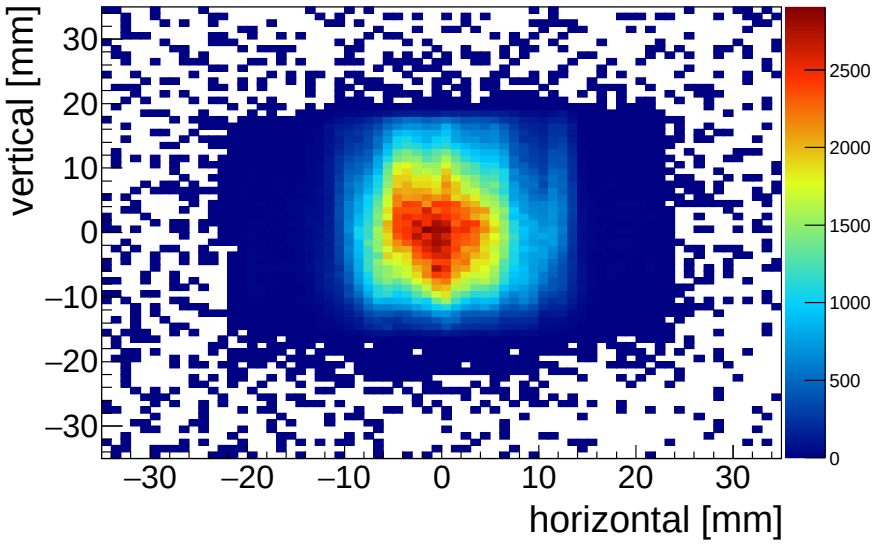

Figure 4.3: Neutron beam profile observed from the downstream side. It is measured by a neutron position detector at the TPC position.

4.2 Beam profile measurement

The neutron beam profile is measured by a two-dimensional neutron position detector. As a neutron position detector, a ZnS/^{6}LiF scintillator is attached at a position-sensitive photomultiplier (model R3292) manufactured by Hamamatsu Photonics. The detector has a sensitive region of 60 cm^2, and the spatial resolution is less than 1 mm^2 [35]. The position dependence of the detection efficiency is evaluated in advance at an interval of 5 mm, and it is found to be at most 10% in the region within 15 cm from the center of the detector.

The neutron position detector is set at the position of the TPC, and the two-dimensional beam distribution is measured. The efficiency-corrected beam profile is shown in Figure 4.3. During the measurement, the SFC operated as usual, thus making 5 neutron bunches per pulse, so as to reproduce the lifetime measurement condition. The standard deviation of the distribution is 5.8 mm and 7.6 mm in the x and y direction, respectively. The result of this beam profile measurement is used as an input of the interaction point as described in Section 4.3.

4.3 Simulated events

4.3.1 Neutron beta-decay

Since a neutron beta-decay process is a three-body decay, each of decay products has a continuous energy spectrum. The maximum kinetic energies of the electron and the proton are 782 keV and 751 eV, respectively. Neglecting the masses of the electron and the anti-neutrino, the kinetic energy

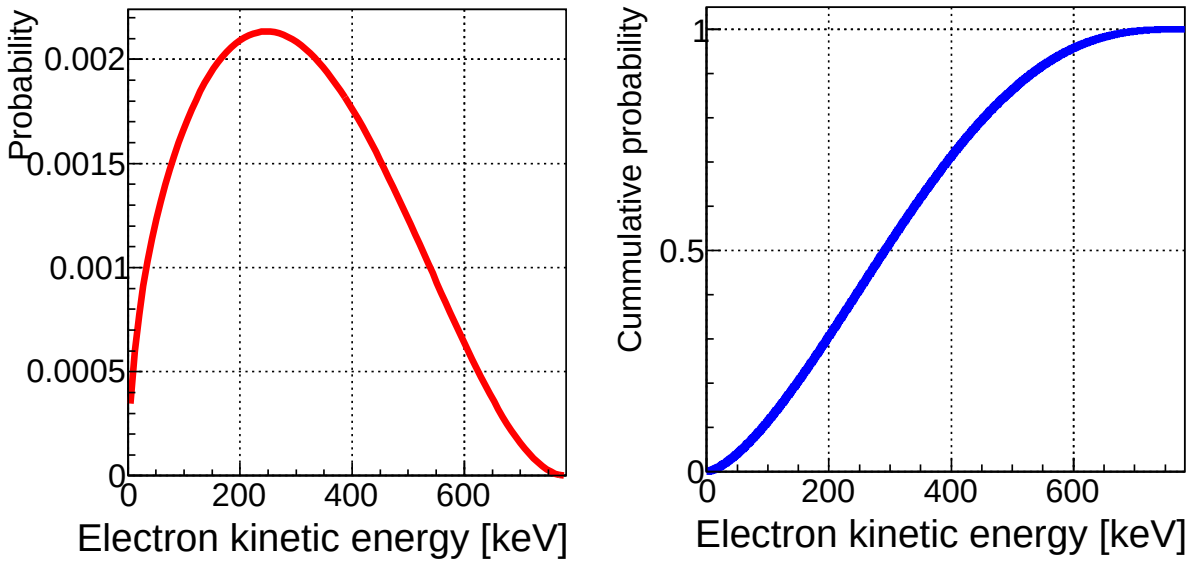

Figure 4.4: Kinetic energy distribution of an electron from neutron beta-decay. The left plot represents the probability density and the right plot represents the cumulative probability.

distribution of an electron K_e is expressed as

$$\frac{d\Gamma}{dK_e} \propto (K_e - Q_e)^2 \sqrt{K_e^2 - m_e^2} K_e, \tag{4.1}$$

where Q_e is the Q-value of the electron energy, and m_e is the mass of an electron. The kinetic energy distribution and its cumulative distribution are plotted in Figure 4.4.

The momentum direction of the electron has a slight dependence with respect to the neutron's polarization direction θ as

$$\frac{d\Gamma}{d\Omega} \propto 1 + A\frac{\vec{J}\cdot\vec{P}_e}{E_e}, \tag{4.2}$$

where $\vec{J}$ is a spin of the neutron beam, P_e and E_e are the momentum and the energy of the electron, respectively. The parameter A $(= -0.1184 \pm 0.0010)$ [6] is the neutron beta-decay asymmetry parameter. There also exists an electron-neutrino angular correlation, which can be expressed as

$$\frac{d\Gamma}{d\Omega} \propto 1 + a\frac{\vec{P}_e\cdot\vec{P}_\nu}{E_e E_\nu}, \tag{4.3}$$

where P_e and E_e are momentum and energy of the anti-neutrino. The parameter a is the electron-neutrino angular coefficient, which is currently evaluated to be -0.1059 ± 0.0028 [6]. The momentum of the proton can be determined to satisfy the momentum conservation law.

The decay point in the x-y plane is randomly selected from the result of a beam profile measurement (see Section 4.2). The z position is determined in order to reproduce the experimental distribution after the event selection using the time of flight (see Section 5.3.1).

4.3.2 $^3\mathrm{He}(n,\ p)^3\mathrm{H}$ reaction

A $^3\mathrm{He}$ nucleus in the TPC captures a neutron and emits a tritium and a proton with a Q-value of 764 keV. According to the masses of the two nuclei, the kinetic energies of a $^3\mathrm{H}$ and a proton are 191 keV and 572 keV, respectively. The two nuclei are emitted in the opposite direction with each other. The range of the two nuclei is a few cm in the usual operation gas composition. The x, y, and z coordinates of $^3\mathrm{He}(n,\ p)^3\mathrm{H}$ reaction points are randomly selected from the same distribution as that of the neutron beta-decay simulation.

4.3.3 Neutron scattering

The neutron scattering cross sections with TPC operation gas molecules are listed in Table 2.5. Since a wavelength of a neutron at BL05 beamline ($\lambda \sim 1$ Å) is the same order of the atomic distance of a $\mathrm{CO_2}$ molecule, coherent scattering cannot be neglected. Generally speaking, the scattering cross section between a neutron and a molecule is expressed as a function of the zenith angle θ as

$$\sigma(\theta) = \frac{1}{4\pi}\left(\frac{M}{M+1}\right)^2 \sum_i \sum_j \sqrt{\sigma_i \sigma_j}\frac{\sin x_{ij}}{x_{ij}}, \tag{4.4}$$

$$x_{ij} \equiv \frac{4\pi r_{ij}}{\lambda}\sin\frac{\theta}{2}, \tag{4.5}$$

where i and j are the index of each atom, r_{ij} is the distance between i and j atoms, σ_i and σ_j are coherent scattering cross sections of i and j nuclei, respectively, λ is a neutron de Brogile wavelength, and M is the mass ratio of the molecule to a neutron [36]. The comparison of theoretical and experimental angular distributions of neutrons with a $\mathrm{CO_2}$ gas molecule was studied by N. Z. Alcock and D. G. Hurst in 1949 as shown in Figure 4.5 [37]. The scattering process is simulated using this formula for a neutron with 5 different velocities (400, 600, 800, 1000, and 1200 m/s). The five velocities approximately represent the velocities of 5 respective neutron bunches.

4.3.4 Cosmic rays

In the cosmic rays simulation, a charged muon is made incident on the upper side of the TPC. The flux ratio of charged muons is set to be $F_{\mu^+}/F_{\mu^-} \sim 1.3$ to reproduce the observed data [6]. The incident angle is implemented to follow the $\cos^2\theta$ distribution with respect to a zenith angle.

4.3.5 Photoabsorption of $^{55}\mathrm{Fe}$ X-rays

The photoabsorption process of $^{55}\mathrm{Fe}$ X-ray is used for the energy calibration. It is simulated by emitting X-rays from the $^{55}\mathrm{Fe}$ source position. The X-ray energy is selected to be 5.86 keV (89%) or 6.45 keV (11%) [29]. The incident angle of the X-ray is limited to reproduce the collimator used in the experiment. The absorption probability of X-rays in the TPC is evaluated to be 18%.

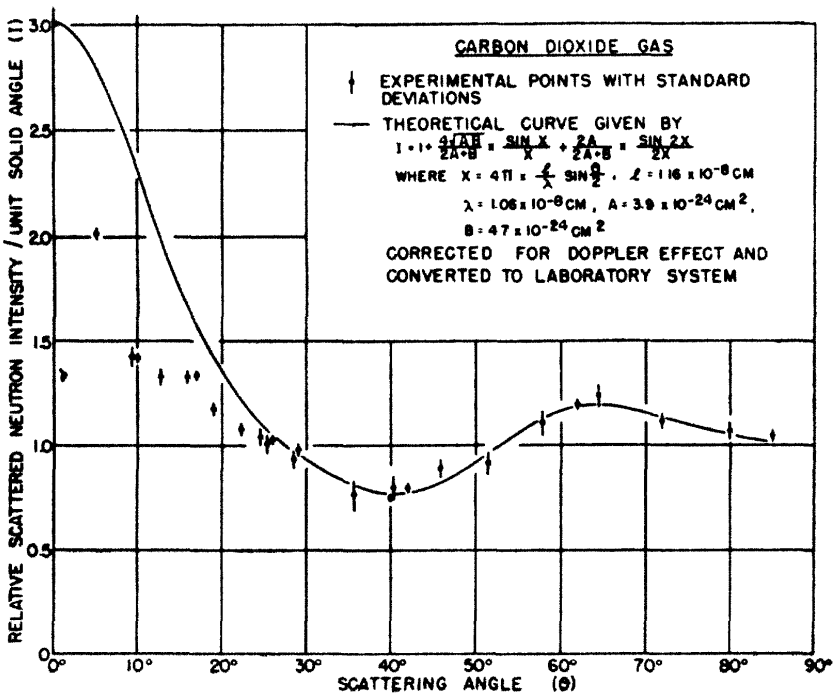

Figure 4.5: Comparison of theoretical and experimental angular distributions of neutrons with a CO_2 gas molecule, taken from the work by N. Z. Alcock and D. G. Hurst in 1949 [37]. According to the paper, the most likely cause of the small intensity at the small angle region is inter-molecular interference because the carbon dioxide used in the experiment was near a liquid form.

Table 4.1: Cross sections and γ-ray energies for a CO_2 molecule to capture a neutron [40].

Reaction	Cross section [mb]	Probability [%]	E_γ^1 [keV]	E_γ^2 [keV]	E_γ^3 [keV]
$^{12}\mathrm{C}(n,\ \gamma)^{13}\mathrm{C}$	3.89 ± 0.06	67.8	4945	-	-
		32.2	1262	3684	-
		0.161	1857	3089	-
$^{16}\mathrm{O}(n,\ \gamma)^{17}\mathrm{O}$	0.189 ± 0.008	81.7	10888	2184	871
		18.3	3272	871	-

4.3.6 Prompt γ-rays from LiF plate

Prompt γ-rays are produced from a LiF plate in the TPC by capturing a scattered neutron. The capture point distribution is evaluated by simulating the neutron scattering process using Eq. 4.4 [31]. A single or multiple γ-rays are emitted from the capture point according to a decay cascade database [38]. The produced γ-ray undergoes Compton scattering mainly with the TPC wall, and the probability is evaluated to be 1.3%.

4.3.7 Prompt γ-ray from SFC

A process of producing prompt γ-rays produced at the SFC is simulated by the Phits simulation [39], in which the SFC and the beam bender at the BL05 beamline is implemented. The energy, momentum, and position of the γ-ray at the position of the neutron shutter are recorded. Making the data as an input, the TPC output is simulated using the Geant4 simulation. The interaction probability between the γ-ray and the TPC is about 2%.

4.3.8 $^3\mathrm{H}$ beta-decay

A neutron beam is captured by a beam dump made of LiF plate, at which the $^6\mathrm{Li}(n,\ \alpha)^3\mathrm{H}$ reaction occurs. A fraction of the tritium produced by the reaction is expected to leak out into the TPC and diffuse through the entire TPC volume. A tritium nucleus undergoes beta-decay process and decays into a $^3\mathrm{He}$, an electron, and an anti-neutrino, with a half lifetime of 12.3 years. The process is simulated by emitting the three decay objects from a randomly selected point in the TPC sensitive region.

4.3.9 $^{12}\mathrm{C}(n,\ \gamma)^{13}\mathrm{C}$ reaction

A CO_2 molecule in the TPC causes $^{12}\mathrm{C}(n,\ \gamma)^{13}\mathrm{C}$ and $^{16}\mathrm{O}(n,\ \gamma)^{17}\mathrm{O}$ reactions and emits γ-rays. The γ-ray energy and cross section are determined based on database values [40] as listed in Table 4.1. The reaction points are randomly selected from the same distribution as that of the neutron beta-decay simulation. The γ-ray is emitted isotropically and the angular correlation between multiple γ-rays is neglected.

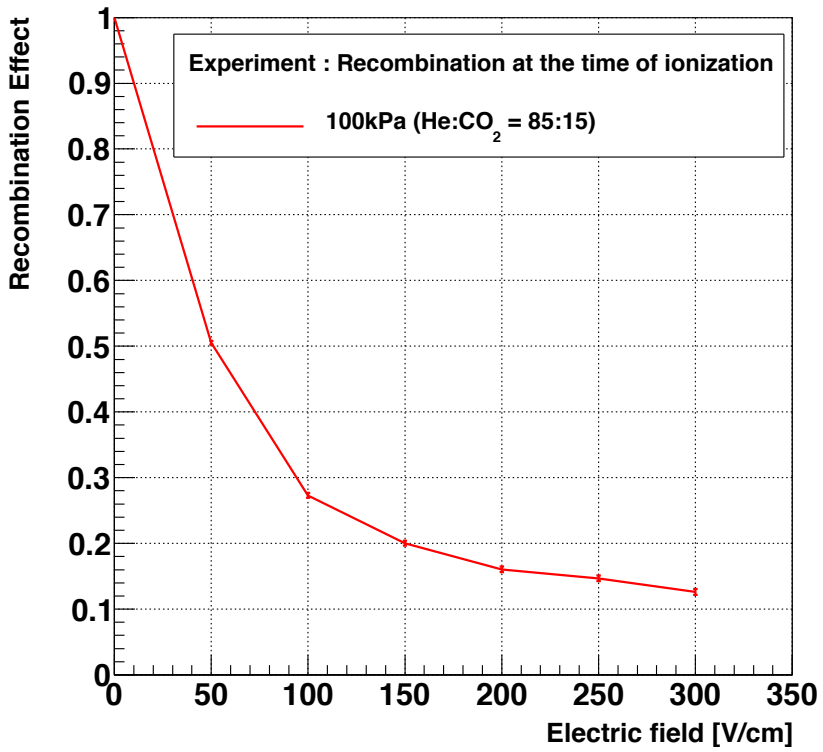

Figure 4.6: Recombination ratio of an electron-ion pair as a function of electric field in the TPC gas composition (85 kPa He and 15 kPa CO_2) [21].

4.4 Detector simulation

In this section, implemented model to describe physical procedures in the TPC is described in this section.

4.4.1 Recombination effect

A fraction of an electron-ion pair produced from a charged particle is recombined into an ordinary natural atom. The recombination affects the number of drifting electrons, resulting in the decrease of the deposit energy measured by the anode wires. For the purpose of evaluating the recombination ratio, the ^{55}Fe X-ray was emitted directory towards the MWPC region, at which the electric field is too strong for the recombination process to occur. By comparing the observed energy at this source position and that in the normal source position, the recombination ratio can be evaluated. Figure 4.6 shows the recombination ratio as a function of an electric field in the TPC [21]. At our normal operation field of 300 V/cm, the ratio was found to be 12%. In the detector simulation process, the number of ionized electrons are decreased by this factor.

4.4.2 Diffusion effect

Drift electrons disperse randomly due to the multiple collisions between gas molecules in the TPC. It directly affects the resolution of the track reconstruction, which is important to separate some backgrounds from the signal events. Assume that ionized electrons are produced at one point $x = 0$ at the time of $t = 0$, which can be expressed as $N(x, t = 0) \propto \delta(x)$, the electron density $N(x, t)$ can be described using a diffusion coefficient D as

$$N(x,t) \propto \frac{1}{\sqrt{Dt}} \exp\left(-\frac{x^2}{4Dt}\right). \tag{4.6}$$

The diffusion coefficient D describes how widely a drift electron disperses. Since the energy deposit from the Fe X-rays is localized in the TPC (typically a few mm), the spread of ionized electrons in the anode wires are used to optimize the diffusion coefficient. Following parameters are introduced to describe the spread of ionized electron:

$$\mathrm{maxch} \equiv \arg\max_{\mathrm{ch}} \Delta E_{\mathrm{ch}}, \tag{4.7}$$

$$\mathrm{CHARGE\_DIV} \equiv \frac{\max\{\Delta E_{\mathrm{maxch}-1}, \Delta E_{\mathrm{maxch}+1}\}}{\Delta E_{\mathrm{maxch}}}, \tag{4.8}$$

where ΔE_i represents the observed energy at the i-th anode wire. The CHARGE_DIV parameter becomes larger when the diffusion effect increases. The diffusion coefficient used in the simulation is determined to reproduce the experimental CHARGE_DIV distribution as shown in Figure 4.7. Noise and background cause the significant excesses in low CHARGE_DIV regions. In this analysis, the region of interest to optimize the diffusion coefficient is set to the CHARGE_DIV > 0.3 region.

4.4.3 Attenuation effect

A fraction of a drifting electron is captured by an impurity gas molecule in the TPC gas, such as a water molecule. During the lifetime measurement, water vapor gradually comes out from the wall of the TPC and the vacuum chamber. The effect significantly deteriorates the multiplication factor of the anode wires, resulting in the decrease of the observed energy deposit. During the lifetime measurement, the attenuation effect can be quantitatively monitored by the Fe (up) and Fe (down) data using Eq. (2.4). In the Monte Carlo simulation, the attenuation length evaluated at the middle time of the total measurement is implemented as an input parameter.

4.4.4 Space charge effect

The avalanche multiplication process for $^3\mathrm{He}(n,\ p)^3\mathrm{H}$ suffers the self-induced space charge effect due to high-density electrons around a wire. As a result, the linearity of the detected energy with respect to the deposit energy deteriorates. In this experiment, the significant space charge effect occurs for the $^3\mathrm{He}(n,\ p)^3\mathrm{H}$ events because of the high-density energy deposit. The $^3\mathrm{He}(n,\ p)^3\mathrm{H}$ events is separated from beta-decays based on the energy deposit, thus the effect is required to be corrected. An analytical model to describe the saturation due to the space charge effect was

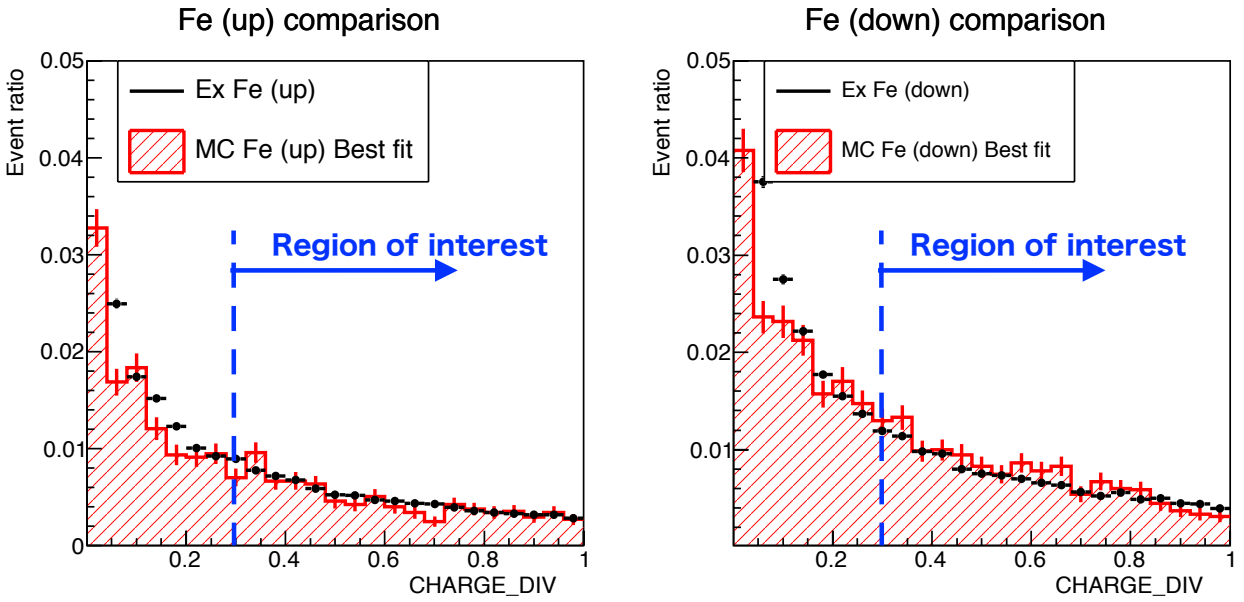

Figure 4.7: Comparison of the diffusion ratio parameter (CHARGE_DIV) for experiment and Monte Carlo simulation. The left and right distributions are the result of Fe (up) and Fe (down) modes, respectively. Noise and background cause the significant excesses in low CHARGE_DIV regions. In this analysis, the region of interest is set to CHARGE_DIV > 0.3.

experimentally verified [41] and implemented in the Monte Carlo simulation. According to the model, the gain reduction factor s ($s < 1$) can be expressed as

$$s = \frac{\log\left(1 + f\frac{dE}{dl}G_0\right)}{f\frac{dE}{dl}G_0}, \tag{4.9}$$

where $\frac{dE}{dl}$ is the energy deposit density per anode wire length, G_0 is a multiplication factor without the space charge effect, and f is a parameter to determine the amplitude of the saturation effect. The experimental verification of the gain reduction model is described in Appendix C.

Comparison of the energy deposit distribution between the experimental data and the Monte Carlo simulation is shown in Figure 4.8. The Monte Carlo simulation without the saturation model is plotted in the left figure, while the simulation with the model in the right figure. The Monte Carlo simulation implementing the gain reduction model describes the measured energy deposit distribution, although there exists a significant discrepancy for the $^3\mathrm{He}(n,\ p)^3\mathrm{H}$ event in the high energy region. The discrepancy is neglected in the analysis because it is much higher than the separation threshold (see Section 5.3.2).

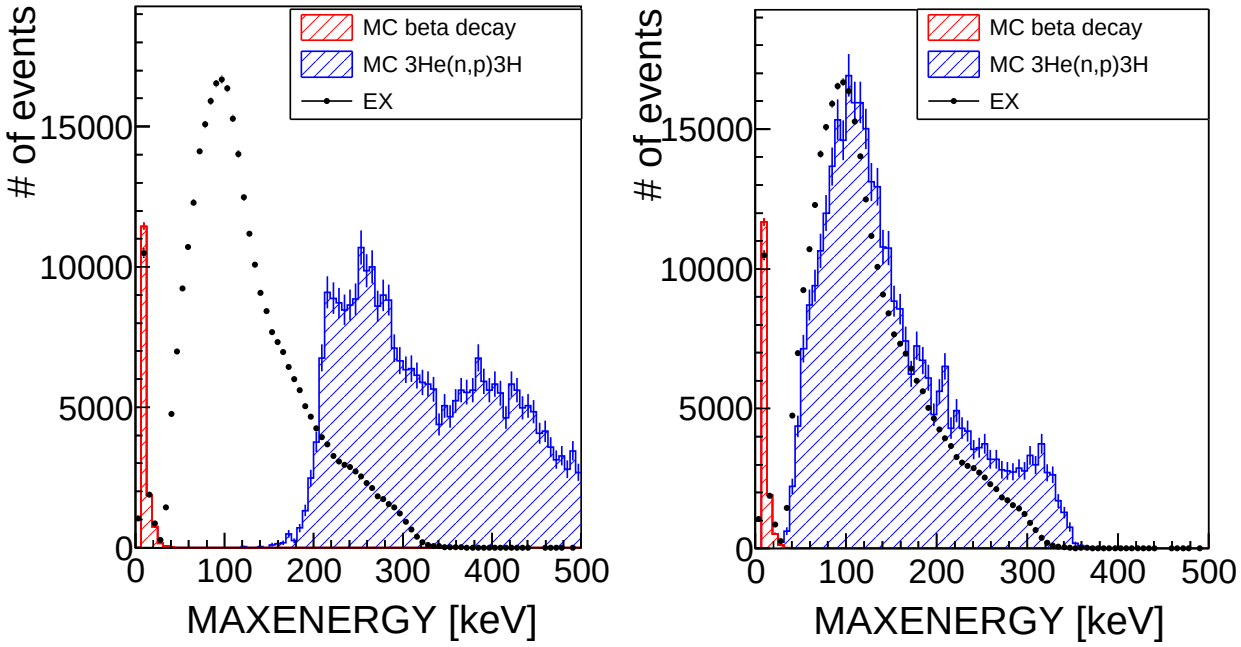

Figure 4.8: Comparison of the maximum energy deposit (MAXENERGY) distribution without space charge correction (left) and with space charge correction based on an analytical gain reduction model [41] (right). The Monte Carlo simulation implementing the gain reduction model describes the measured energy deposit distribution, although there exists a significant discrepancy for the $^{3}\mathrm{He}(n,\ p)^{3}\mathrm{H}$ event in the high energy region.

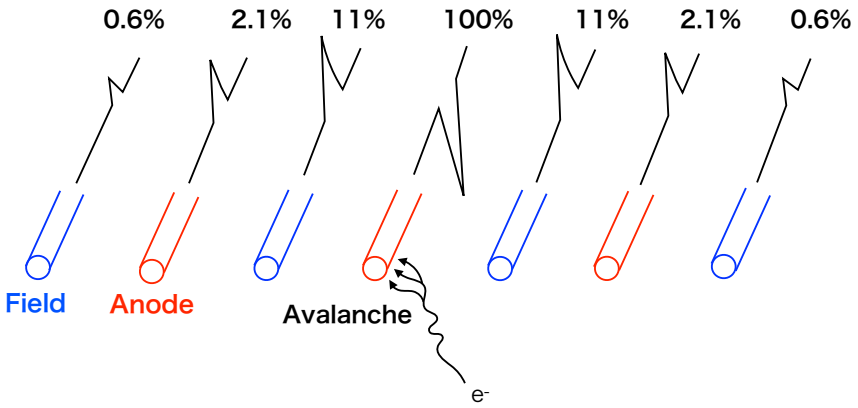

Figure 4.9: Amplitude ratio of induced waveform for wires near the avalanche anode wire evaluated by the ANSYS [43] and Garfield [23] software.

4.4.5 Charge-inducing process

A wire signal waveform is induced by a motion of ions produced from an avalanche multiplication. Furthermore, the motion also induces reverse-phase waveforms at the grounded wires (the field and cathode wires) and anode wires at which no avalanche multiplication has occurred. In this experiment, the field wires as well as the anode wires are used to measure the energy deposit of charged particles, therefore the amplitude of the induced charge is an important parameter for the energy calibration. It can be determined using Ramo's theorem [42]. According to the theorem, the induced current i at an electrode is expressed as

$$i = q\vec{v} \cdot \vec{E_w}, \tag{4.10}$$

where q is the electric charge, $\vec{v}$ is the velocity vector of the charge, $\vec{E_w}$ is the weighted field of the electrode. The weighted field can be obtained by giving unit potential to the electrode and grounding the other electrodes. The calculation is conducted using ANSYS [43] and Garfield [23] software. As shown in Figure 4.9, the amplitude is evaluated as a function of the distance between the target wire and the point where the avalanche multiplication has occurred. The software is not able to calculate the induced signal of the cathode wires due to memory shortage. Therefore, in the detector simulation process, the induced waveforms of the cathode wires are generated to reproduce experimental pulse height distributions.

Chapter 5

Analysis

This chapter introduces the analysis procedure to evaluate the number of signal events (S_β and $S_{^3\mathrm{He}}$) and the number density of $^3\mathrm{He}$ (ρ). The analysis parameters used in the analysis are defined in Section A.

5.1 Expected background

The Expected background events for S_β and $S_{^3\mathrm{He}}$ detected at the TPC are described in this section.

5.1.1 Types of backgrounds for $^3\mathrm{He}(n,\ p)^3\mathrm{H}$

- $^{14}\mathrm{N}$ neutron capture (hereinafter called B_{nitro})
  Although nitrogen is not originally injected into the TPC as operation gas, it gradually comes out from the wall of the TPC or the vacuum chamber. A neutron is captured by a $^{14}\mathrm{N}$ nucleus of a nitrogen molecule and undergoes $^{14}\mathrm{N}(n,\ p)^{14}\mathrm{C}$ reaction in the TPC. The Q-value of the reaction is 626 keV, and the cross section is (1.83 ± 0.03) barn [15].

- $^{17}\mathrm{O}$ neutron capture (B_{oxy})
  A neutron is captured by a $^{17}\mathrm{O}$ nucleus, which exists as an isotope of an oxygen in $\mathrm{CO_2}$ gas. The natural abundance of $^{17}\mathrm{O}$ is $(3.8 \pm 0.3)\%$ [15]. The Q-value is 1818 keV and its cross section is (0.235 ± 0.010) barn [15].

- $^3\mathrm{He}(n,\ p)^3\mathrm{H}$ from scattered neutrons (B_{scat3He})
  Neutrons are scattered by gas molecules in the TPC with a probability of about 1%, and the neutrons cause the $^3\mathrm{He}(n,\ p)^3\mathrm{H}$ reaction. A fraction of the event occurs near the TPC wall and has small energy deposit in the TPC, which leads to deteriorate the detection efficiency for the $^3\mathrm{He}(n,\ p)^3\mathrm{H}$ reaction. In order to avoid the deterioration, the $^3\mathrm{He}(n,\ p)^3\mathrm{H}$ reaction from scattered neutrons is treated as a background in the analysis.

5.1.2 Types of backgrounds for neutron beta decay

- ^{12}C neutron capture (hereinafter called B_{CO2})
  A ^{12}C or ^{16}O nucleus in a CO_2 gas molecule captures a neutron and undergoes the $^{12}\mathrm{C}(n,\ \gamma)^{13}\mathrm{C}$ or $^{16}\mathrm{O}(n,\ \gamma)^{17}\mathrm{O}$ reactions, respectively. The cross sections of the two reactions are (3.53 ± 0.07) barn and (0.190 ± 0.019) barn, respectively [15]. After capturing, the nucleus in an excited state returns to a ground state with prompt γ-rays while the nucleus itself recoils towards the opposite direction. The typical recoil energy is a few keV, which is high enough to be detected by the TPC.

- γ-ray produced inside the TPC ($B_{\mathrm{int}\gamma}$)
  A scattered neutron interacts with a LiF plate in the TPC and produces prompt γ-rays from (n, γ) reaction, such as ^{6}Li($n,\ \gamma)^{7}$Li and ^{19}F($n,\ \gamma)^{20}$F. The γ-rays undergo Compton scattering with the TPC gas or wall material and produces an electron inside the TPC sensitive region.

- Beta-decays from scattered neutrons ($B_{\mathrm{scat}\beta}$)
  A scattered neutron undergoes beta-decay in the TPC. This event is treated as a background in the same way as B_{scat3He} for consistency.

- ^{3}H beta-decay (B_{trit})
  A neutron beam passing through the TPC is captured by a beam dump made of a LiF plate mainly through the $^{6}\mathrm{Li}(n,\ \alpha)^{3}\mathrm{H}$ reaction. Some tritium nuclei are expected to be emitted from the plate and dispersed in the TPC gas. A tritium nucleus decays into a ^{3}He, an electron, and an anti-neutrino through the beta-decay process with a half-life of 12.3 year and a Q-value of 18.6 keV. During the measurement, the increase of the point-like events can be observed in the sideband region [31]. The events are uniformly distributed in the TPC.

- γ-ray produced outside of the TPC ($B_{\mathrm{ext}\gamma}$)
  At the SFC, prompt γ-rays synchronized with the neutron pulses are produced due to the neutron absorption at, for example, the magnetic super mirror. Some γ-rays pass through the beam pipe and cannot be absorbed by the lead shield. A fraction of the γ-ray undergoes Compton scattering and produces an electron in the TPC. This background has the time-of-flight distribution roughly synchronized with that of the neutron pulses.

- TPC material radioactivation (B_{rad})
  When a neutron beam is made incident in the TPC, the material inside the TPC becomes radioactivated by capturing a neutron. For example, a LiF plate captures a neutron beam and produces radioactive isotopes, such as ^{8}Li and ^{20}F, which undergo beta-decay with lifetimes of (839.9 ± 0.9) ms and (11.00 ± 0.02) s, respectively [40]. These lifetimes are much larger than the pulse repetition interval (40 ms), while much shorter than the data acquisition period ($\sim$1000 s). Consequently, (1) this background is not observed in the shutter-closed mode, but only in the shutter-open mode, and (2) the background has the constant time-of-flight distribution in the shutter-open mode.

- Environmental background (B_{env})
  A constant background existing both in the shutter-open and shutter-closed modes is classified

Table 5.1: Trigger event rate of signal and background in the fiducial time window at Fill94 (300 kW accelerator operation).

Event	Event rate [cps]	
S_β	1.2	
B_{CO2}	3.5	
$B_{\mathrm{int}\gamma}$	0.05	
$B_{\mathrm{scat}\beta}$	0.003	
B_{trit}	0.0$\sim$ 0.2	increase with time
$B_{\mathrm{ext}\gamma}$	0$\sim$1	dependent on time of flight
B_{rad}	0.06	
B_{env}	5.7	
$S_{^3\mathrm{He}}$	27	
B_{nitro}	0$\sim$0.1	increase with time
B_{oxy}	0.2	
B_{scat3He}	0.06	

as this type of background. One example is natural radiation, such as beta-decay or electron capture of a ^{40}K nucleus. Furthermore, when a cosmic ray passing through a gap of the veto counters creates an energy deposit in the TPC, such an event cannot be vetoed by our trigger system and is counted as this type of background.

5.1.3 Event rates of signal and background

The trigger event rates of signal and background described above are listed in Table 5.1. Note that the event rates of B_{trit} and B_{nitro} increases with the elapsed time after the gas filling time.

5.2 Definition of analysis parameters

Definitions of parameters used in this analysis are described in this section. The mathematical expression of the definitions is described in Appendix A.

The following parameters for the waveforms of anode, field, and cathode wires are defined as shown in Figure 5.1. The parameters defined in every event are introduced in the following, some of which are described in Figure 5.2.

- TOTALENERGY
  Total energy deposit detected by the all anode wires.
- MAXENERGY
  Maximum energy deposit per wire among all the field wires. It is used to describe how localized the energy deposit is in the TPC.
- LOCALITY
  Ratio of the maximum energy deposit to the total energy deposit among all the anode wires

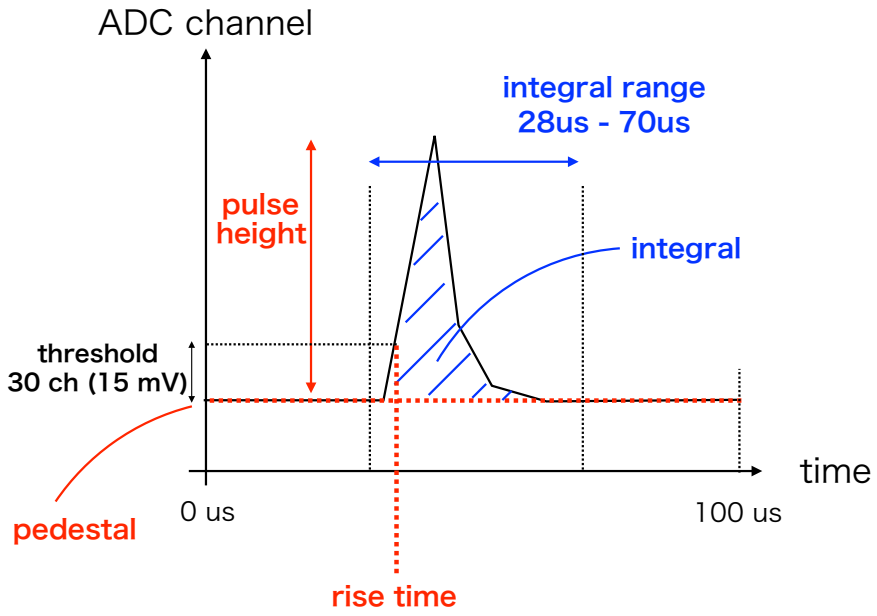

Figure 5.1: Waveform parameter definitions. The detailed definition is described in Appendix A.

- MINRISE
  Trigger timing of the TPC (corresponds to the time when the first wire waveform exceeds the threshold level).

- HITNUM
  Number of wires detecting energy deposit above the threshold level among all the field wires. It describes the track length in the field wire direction.

- DTIME
  Track length in the y direction as a unit of drift time measured by the anode wires.

- CENTER
  Track center position weighted by the energy deposit of wires. It expresses the reaction point in the $^3\mathrm{He}(n,\ p)^3\mathrm{H}$ event. CENTER_A, CENTER_F, and CENTER_CH correspond to the center position measured by the anode wires, the field wires, and cathode high-gain wires, respectively

- DTC (Distance between Track and TPC Center in Anode wires)
  The distance between the center wire and the most closest wires detecting energy deposit. DTC_A and DTC_CH correspond to the distance measured by the anode wires and cathode high-gain wires, respectively.

- DVC (Distance between track Vertex and TPC Center in Anode wires)
  Distance between the track origin point and TPC center as a unit of wire interval. DVC_A and DVC_CH correspond to the distance measured by the anode wires and cathode high-gain

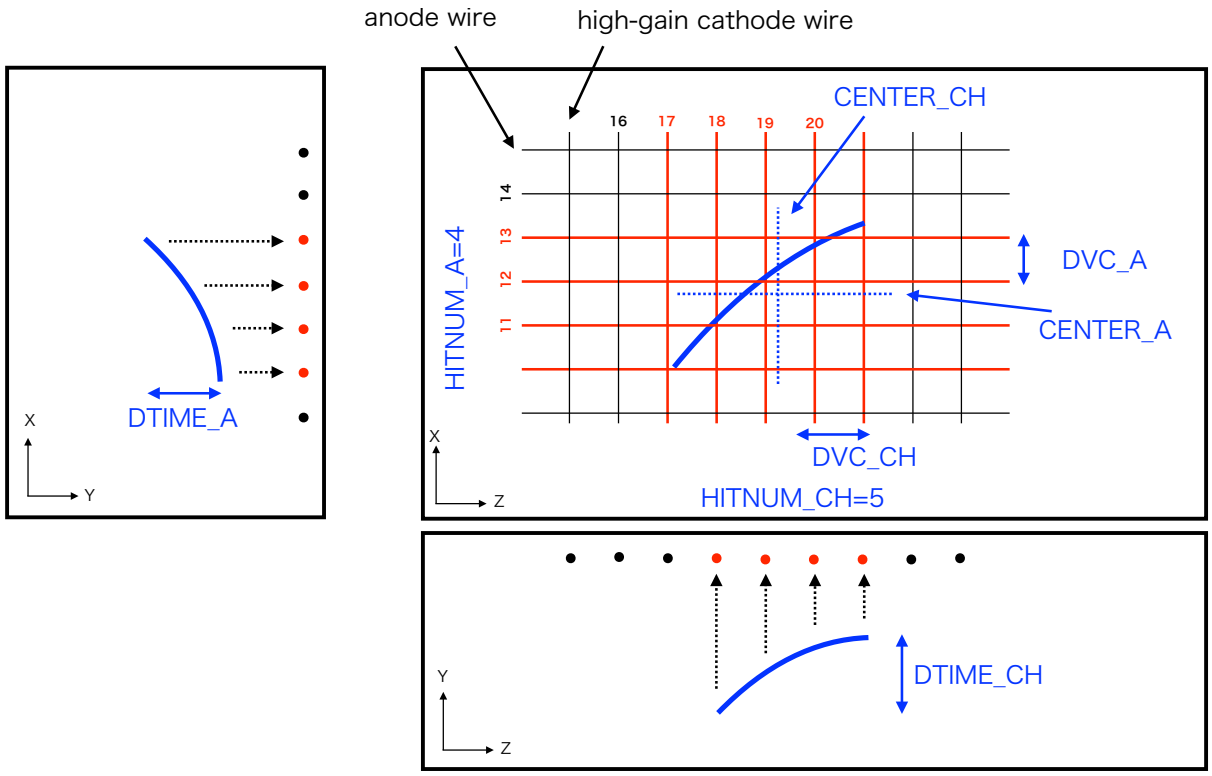

Figure 5.2: Track parameter definitions. The detailed definition is described in Appendix A.

wires, respectively. DTC and DVC parameters are closely correlated to the track origin point and are useful to separate the background event originating from the TPC wall.

5.3 Data analysis algorithm

An analysis algorithm to extract the number of signal events (S_β and $S_{^3\mathrm{He}}$) from the acquired data is introduced in this section. The section describes the overall procedure of the analysis, and the details are described in the following sections. The overall analysis algorithm is described in Figure 5.3. Each of the detailed procedures is explained according to the sequence in the figure.

5.3.1 Time-of-flight subtraction method

The TOF subtraction process is conducted at first for the obtained data, at which the background having different TOF structure can be subtracted, such as $B_{\mathrm{ext}\gamma}$, B_{rad}, and B_{env}. Figure 5.4 shows a schematic drawing of the TOF distribution for the signal (beta-decay) and background events in the TPC. The variable N is defined as the number of observed events in the TPC, where the superscript "open" or "close" represents the shutter mode, and the subscript "f" and "s" represents the "fiducial" and "sideband" time in the TOF distribution. The background events having different

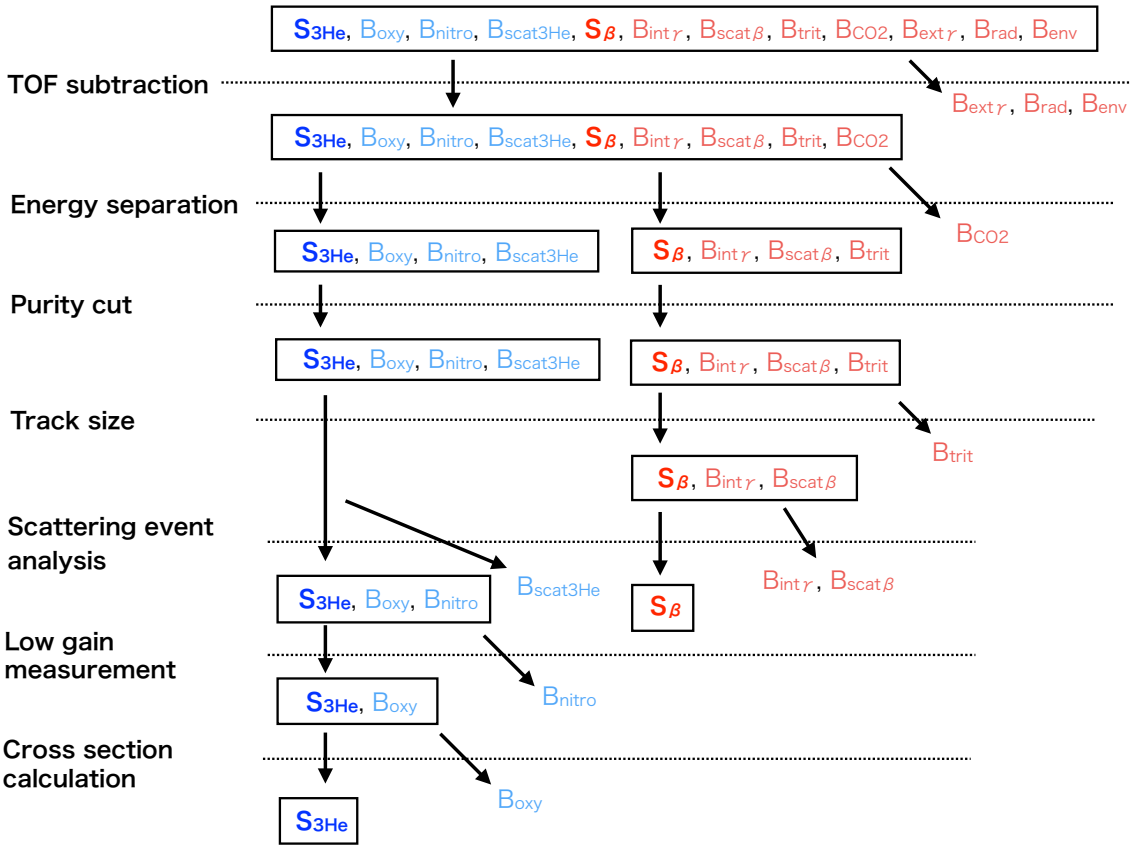

Figure 5.3: Analysis flow to select the beta-decay events (S_β) and the $^3\mathrm{He}(n,\ p)^3\mathrm{H}$ events ($S_{^3\mathrm{He}}$).

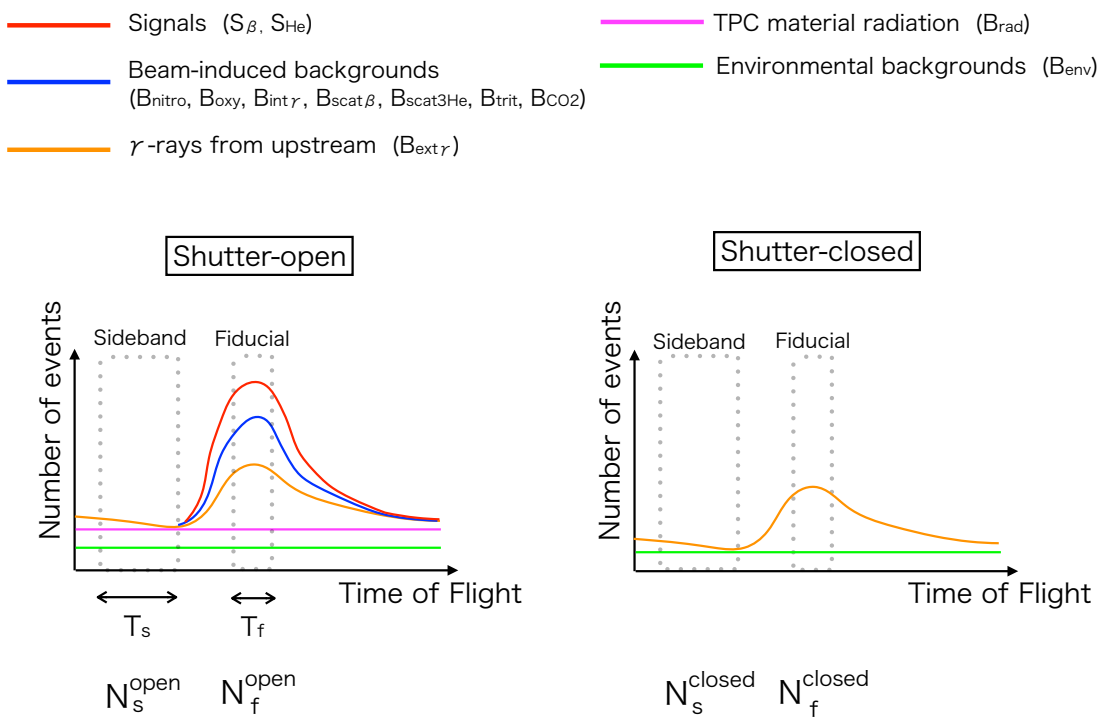

Figure 5.4: Schematic drawing of the time-of-flight distribution for signal and background events in the shutter-open (left) and shutter-closed (right) mode. The backgrounds with different time-of-flight structure from signals can be subtracted using the two distributions. Note that there are five sets of fiducial time per pulse in the actual measurement setup, although only one is shown in the figure.

TOF structure than that of signal events can be subtracted in this process. Both $B_{\mathrm{ext}\gamma}$ and B_{env} backgrounds can be subtracted using the shutter-closed data. The B_{rad} background can be estimated using the sideband data in the shutter-open mode because it has a uniform TOF distribution. For comparing the shutter-open and shutter-closed events, the total counts of the beam monitor (BM_{open} and BM_{closed}) are used. This normalization can correct for the neutron flux fluctuation during the measurement. On the other hand, for comparing the fiducial and sideband events, each of the time width per neutron pulse ($T_f = 2.35$ ms and $T_s = 6.00$ ms) is used as the normalization factor. As a result, the amount of these three types of backgrounds can be subtracted from N_f^{open} as

$$N_f^{\mathrm{open}} - (B_{\mathrm{ext}\gamma} + B_{\mathrm{env}}) - B_{\mathrm{rad}} \tag{5.1}$$

$$= N_f^{\mathrm{open}} - N_f^{\mathrm{closed}} \times \frac{BM^{\mathrm{open}}}{BM^{\mathrm{closed}}} - \frac{T_f}{T_s}\left(N_s^{\mathrm{open}} - N_s^{\mathrm{closed}} \times \frac{BM^{\mathrm{open}}}{BM^{\mathrm{closed}}}\right). \tag{5.2}$$

5.3.2 Energy separation

The acquired data after the TOF subtraction is divided into three categories based on the deposit energy in the TPC. First, high energy events are defined as those with MAXENERGY of larger than

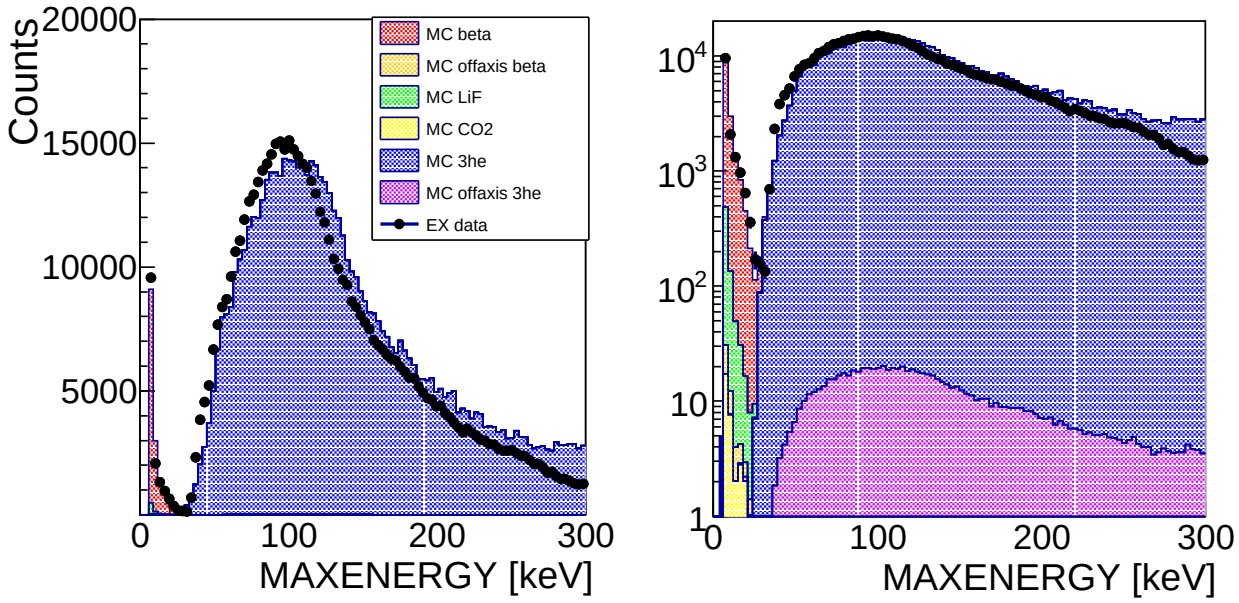

Figure 5.5: Maximum energy deposit (MAXENERGY) distribution in linear scale (left) and logarithmic scale (right). The clear separation of the beta-decay events and the $^3\mathrm{He}(n,\ p)^3\mathrm{H}$ events at around 30 keV is seen.

25 keV. Here, S_β-like events (S_β, B_{CO2}, $B_{\mathrm{int}\gamma}$, $B_{\mathrm{scat}\beta}$, and B_{trit}) and $S_{^3\mathrm{He}}$-like events (S_{He}, B_{nitro}, B_{scat3He}, and B_{oxy}) are separated as shown in Figure 5.5. Next, the events having TOTALENERGY less than 5 keV are treated as very low energy events and separated from the beta-decay events as shown in Figure 5.6. In this process, 99.9% of the B_{CO2} background can be subtracted because the energy deposit in the TPC is extremely low (typically a few keV in the TPC). The remaining 0.1% events still exists in the beta-decay region, which is treated as the uncertainty for the beta-decay event (see Section 6.1).

5.3.3 Purity cut

Several purity cuts are applied for both S_β-like and $S_{^3\mathrm{He}}$-like events to increase the signal-to-noise ratio. The purity cuts are introduced in the following.

- Beta-decays
  - Trigger cut
    The trigger timing is later than 25 μs (MINRISE > 25 μs).
    The cut requires no events before trigger timing.
  - Anode any hit cut
    Reconstructed track center position of anode wires exists in the sensitive area (0 wire < CENTER_A < 23 wire).
    The cut requires detection of the energy deposit by any anode wire.

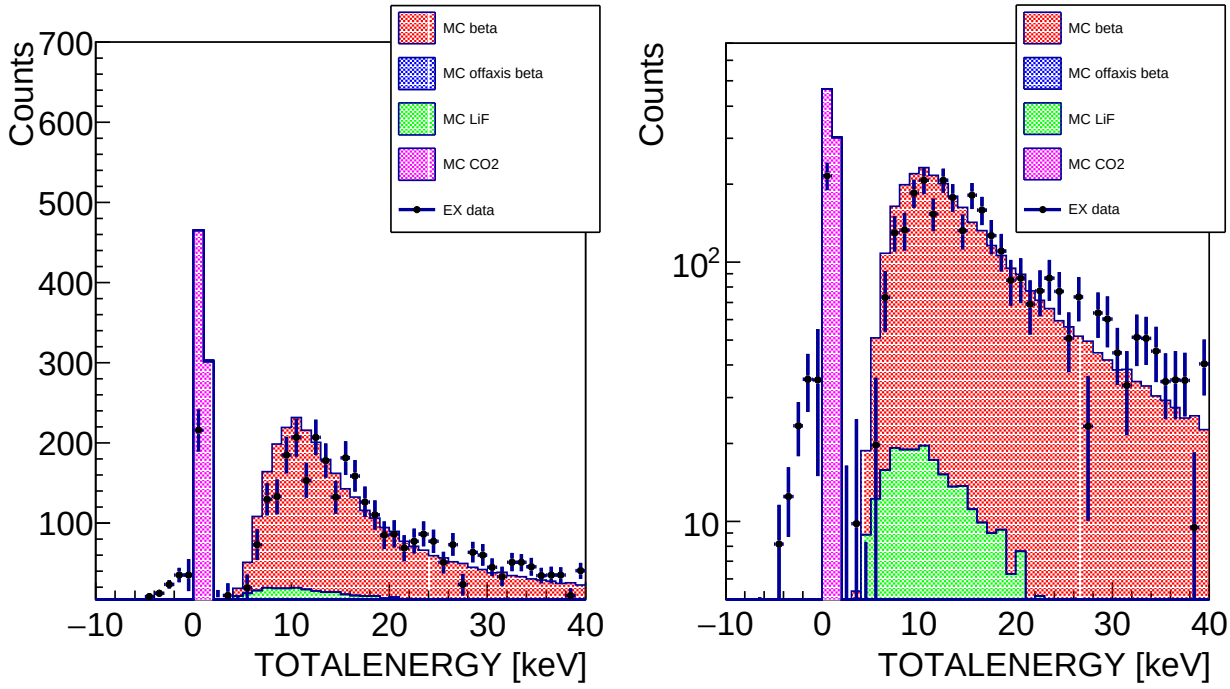

Figure 5.6: Total energy deposit (TOTALENERGY) distribution in linear scale (left) and logarithmic scale (right). The cut threshold energy is set at 5 keV. The shortage of the B_{CO2} background in the experimental data supposedly originates from the TPC inefficiency at the low energy region.

  - Drift cut
    Track length in the y direction is shorter than 190 mm (DTIME < 190 mm).
    The cut rejects events whose track passing vertically through the TPC, such as cosmic rays.
  - TPC passing cut
    Track does not pass through the TPC in the z direction ((CENTER_CH-20)^2+(DVC_CH-20)^2 < (8 wires)^2).
    The cut rejects events whose track passing parallel to the beam direction in the TPC.

- $^3\mathrm{He}(n,\ p)^3\mathrm{H}$
  - Trigger cut
    Same as the one for beta-decays.
  - Anode any hit cut
    Same as the one for beta-decays.
  - Basic cut
    The cut requires the energy deposit detection by at least one fired field wires. Furthermore, the reconstructed track center position by the field wires is required to exist in the TPC sensitive area (HITNUM > 0 & 0 wire < CENTER_F < 23 wire).

5.3.4 Track size separation

A track size selection is introduced to separate the B_{trit} background from the rest of S_β events. The maximum kinetic energy of an electron is 18.6 keV, flying a few mm in the TPC gas. As a result, the energy deposit is extremely localized in the TPC, and only a single anode wire detects the energy deposit. The track localization in the TPC is expressed by the LOCALITY parameter. Figure 5.7 shows the LOCALITY distribution for the experimental data, the S_β events, and the B_{trit} background. The separation threshold value is optimized to be 0.8. According to the Monte Carlo simulation, the inefficiency of this selection for the beta-decay events is 0.6%.

5.3.5 Scattering event analysis

In the scattering event analysis procedure, the amount of gas-induced backgrounds for $^3\mathrm{He}(n,\ p)^3\mathrm{H}$ (B_{scat3He}) and beta-decay ($B_{\mathrm{int}\gamma}$ and $B_{\mathrm{scat}\beta}$) is estimated by the Monte Carlo simulation. The $^3\mathrm{He}(n,\ p)^3\mathrm{H}$ reaction from a scattered neutron can be identified using the reaction point in the TPC. As a parameter to describe the position, a weighted mean position of the field wires (CENTER_F) is used. The B_{scat3He} background has a broad distribution, while $S_{^3\mathrm{He}}$ has a localized distribution around the center. As shown in Figure 5.8, the simulated B_{scat3He} and $S_{^3\mathrm{He}}$ distributions are normalized by the numbers of events in the inner (5 wires <CENTER_F<18 wires) and outer (CENTER_F < 5 wires or CENTER_F > 18 wires) regions in the experimental data. The ratio of the two normalized events, which is 0.3%. The $B_{\mathrm{scat}\beta}$ distribution is also normalized using this scattering probability.

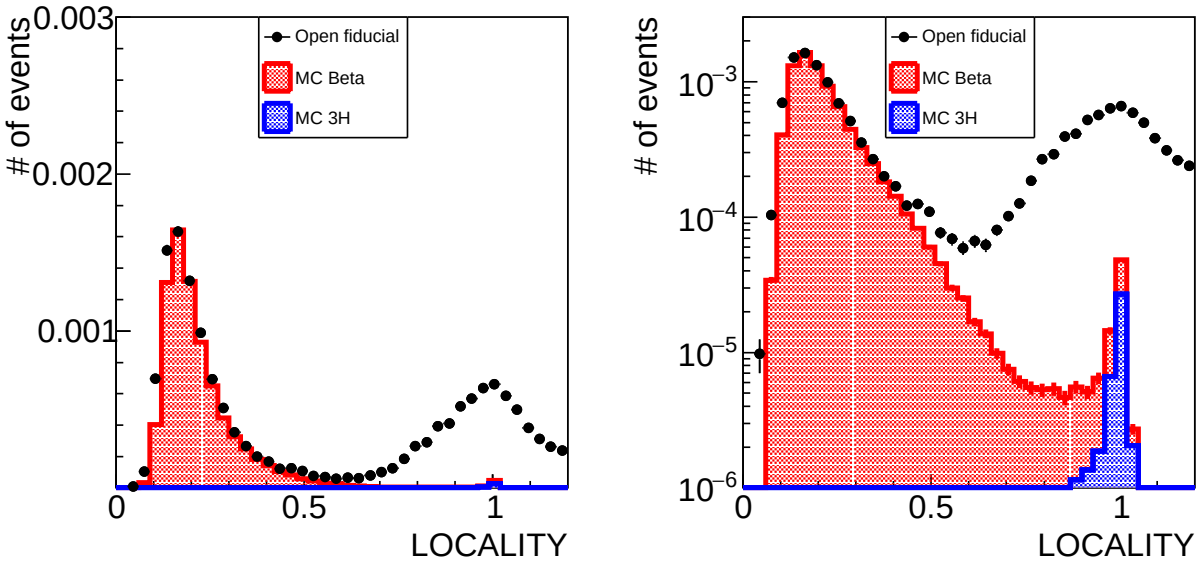

Figure 5.7: Track length locality (LOCALITY) distribution in linear scale (left) and logarithmic scale (right). The cut threshold energy is set at 0.8. The experimental fiducial distribution in the shutter open mode is also shown as black points. The distributions of the Monte Carlo simulation are arbitrary normalized.

The amount of $B_{\mathrm{int}\gamma}$ is estimated using the DTC_A parameter, which represents the initial ionization point in the TPC in the anode wire direction. An electron track starts at around the beam position for S_β, thus the S_β event exists at the inner region DTC_A < 4 wires. The $B_{\mathrm{int}\gamma}$ background, on the other hand, has a flat DTC_A distribution because an electron track mainly originates from the TPC wall. The simulated $B_{\mathrm{int}\gamma}$ distribution is normalized by the number events in the outer region (DTC_A $\geqq$ 4 wires). Figure 5.9 shows the DVC_A distribution, in which the signal region is defined as DVC_A < 4 wires. The amount of the gas-induced background is evaluated to be about 5% for S_β in the signal region.

5.3.6 Low-gain measurement

After sealing the vacuum chamber, the nitrogen pressure gradually increases due to outgas from the material, such as PEEK. A ^{14}N nucleus captures a neutron and undergoes a $^{14}\mathrm{N}(n,\ p)^{14}\mathrm{C}$ reaction with a Q-value of 626 keV. Unfortunately, the TPC does not have enough energy resolution to separate the event from the $^{3}\mathrm{He}(n,\ p)^{3}\mathrm{H}$ events (Q=764 keV). For the purpose of separating the two kinds of events, the applied voltage of the anode wires is decreased to 1200 V (see Table 3.2) so that the multiplication factor decreases by 2 orders of magnitude. Under this condition, the beta-decay signal could not be detected. The low-gain data is taken usually every other day (each one is called as a data cycle) during the lifetime measurement.

Figure 5.10 shows the TOTALENERGY distribution of the all data cycles under the low-gain condition. The clear separation of ^{14}N and $^{3}\mathrm{He}(n,\ p)^{3}\mathrm{H}$ is seen. The double-gaussian fitting is

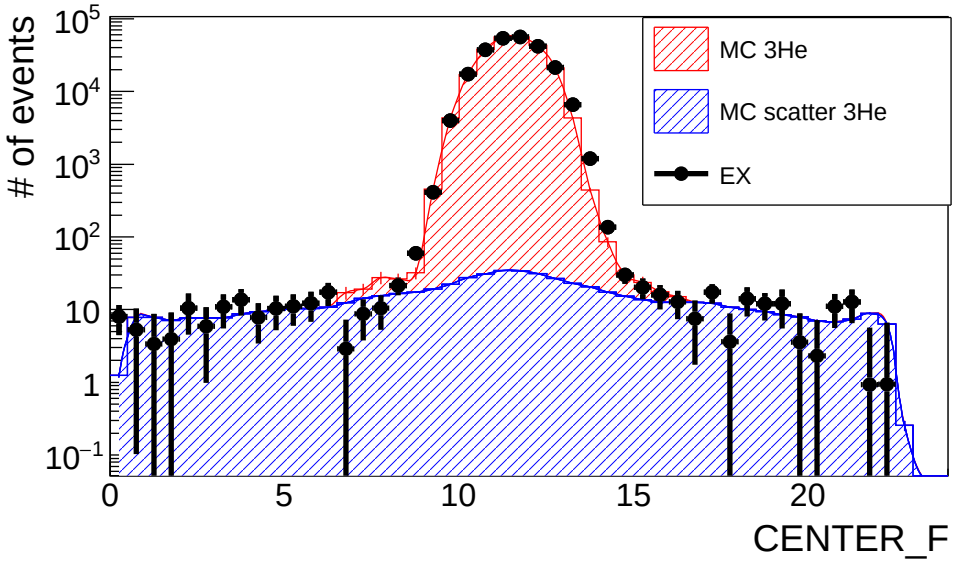

Figure 5.8: Distribution of the reaction x position (CENTER_F) of the $^3\mathrm{He}(n,\ p)^3\mathrm{H}$ events. The experimental data (black points) are fit by the Monte Carlo simulation result of $^3\mathrm{He}(n,\ p)^3\mathrm{H}$ reaction from scattered neutrons (blue) and $^3\mathrm{He}(n,\ p)^3\mathrm{H}$ reaction from non-scattered neutrons (red).

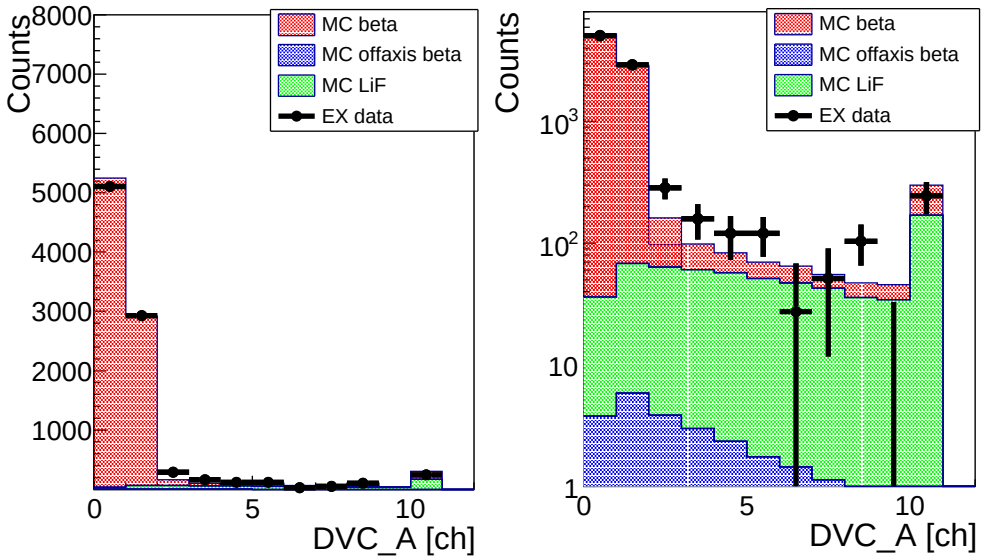

Figure 5.9: Distribution of the distance between track vertex and TPC center (DVC_A) for S_β, $B_{\mathrm{int}\gamma}$, and $B_{\mathrm{scat}\beta}$ in a linear scale (left) and a logarithmic scale (right).

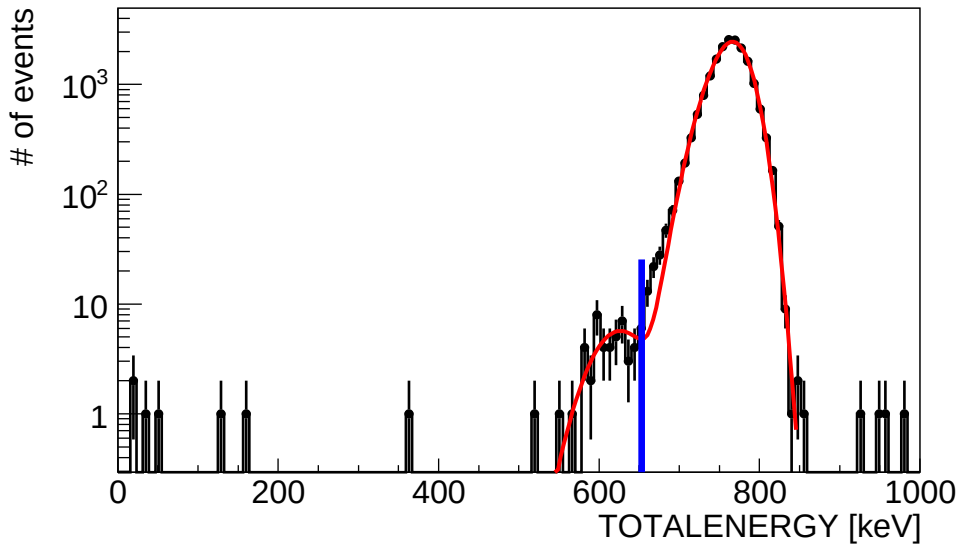

Figure 5.10: Total energy deposit (TOTALENERGY) distribution under the low-gain condition (anode voltage at 1200 V). The two peak corresponds to the $^{14}\mathrm{N}(n,\ p)^{14}\mathrm{C}$ (Q=626 keV) and $^{3}\mathrm{He}(n,\ p)^{3}\mathrm{H}$ (Q=764 keV) events. The cut threshold drawn as a blue line is set at a local minimum of the distribution. The deviation of the low-energy $^{3}\mathrm{He}(n,\ p)^{3}\mathrm{H}$ peak from the gaussian function is expected to be due to the space charge effect around the anode wires.

conducted for the distribution, and the cut threshold is set at the local minimum position. The numbers of both the $^{14}\mathrm{N}(n,\ p)^{14}\mathrm{C}$ and the $^{3}\mathrm{He}(n,\ p)^{3}\mathrm{H}$ events are counted for each data cycle. The contamination from the $^{3}\mathrm{He}(n,\ p)^{3}\mathrm{H}$ peak to the $^{14}\mathrm{N}(n,\ p)^{14}\mathrm{C}$ peak is corrected based on the fitting result. Note that the fitting for the $^{14}\mathrm{N}(n,\ p)^{14}\mathrm{C}$ distribution does not work well for each data cycle because of the poor statistics. Figure 5.11 shows the time variation of the contamination. The data is fit by a straight line, and it is found to have (0.430 ± 0.031) Pa/day increase in average. The result is used to correct for the number of $^{3}\mathrm{He}(n,\ p)^{3}\mathrm{H}$ events counted in the high-gain mode. Since the rate of increase depends heavily on how good the vacuum condition has been before injecting the operation gas, the contamination analysis is conducted individually for each gas condition.

5.3.7 Cross section calculation

A $^{17}\mathrm{O}$ nucleus in a $\mathrm{CO_2}$ molecule captures a neutron in the TPC and undergoes the $^{17}\mathrm{O}(n,\ \alpha)^{14}\mathrm{C}$ reaction. Since the TPC does not have enough energy resolution to separate this event from $S_{^3\mathrm{He}}$, the contamination from the B_{oxy} events is corrected based on its reaction probability. It is calculated using the cross section and the natural abundance of $^{17}\mathrm{O}$. Assuming the natural abundance ratio of $^{17}\mathrm{O}$ ($R_{^{17}\mathrm{O}}$=0.038%) for the $\mathrm{CO_2}$ gas and the 100% detection efficiency of the TPC, the number of

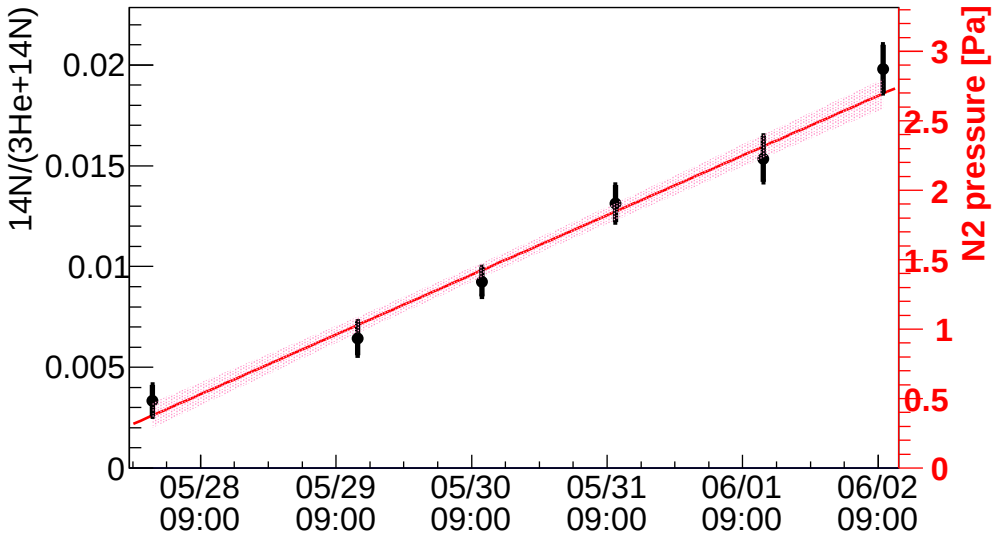

Figure 5.11: Ratio of $^{14}\mathrm{N}(n,\ p)^{14}\mathrm{C}$ and $^{3}\mathrm{He}(n,\ p)^{3}\mathrm{H}$ events as a function of time. The data points are plotted for each data cycle. The corresponding nitrogen pressure is also shown on the right axis. The data is fit by a straight line ($\chi^2/\mathrm{ndf} = 3.66/4 = 0.92$), and the pink band represents the 1σ standard deviation of the fitting line. The rate of increase is evaluated to be (0.430 ± 0.031) Pa/day.

$^{17}\mathrm{O}(n,\ \alpha)^{14}\mathrm{C}$ events with respect to that of $^{3}\mathrm{He}(n,\ p)^{3}\mathrm{H}$ ($N_{^{17}\mathrm{O}}/N_{^{3}\mathrm{He}}$) in the TPC is calculated as

$$\frac{N_{^{17}\mathrm{O}}}{N_{^{3}\mathrm{He}}} = \frac{\sigma_{^{17}\mathrm{O}} \times \rho_{^{17}\mathrm{O}}}{\sigma_{^{3}\mathrm{He}} \times \rho_{^{3}\mathrm{He}}}, \tag{5.3}$$

$$= \frac{\sigma_{^{17}\mathrm{O}} \times 2P_{\mathrm{CO_2}} \times R_{^{17}\mathrm{O}}}{\sigma_{^{3}\mathrm{He}} \times P_{^{3}\mathrm{He}}}. \tag{5.4}$$

Under the normal gas conditions, $P_{\mathrm{CO_2}} = 15$ kPa and $P_{^{3}\mathrm{He}} = 100$ mPa, and according to Table of Isotopes, $\sigma_{^{17}\mathrm{O}} = (0.235 \pm 0.010)$ barn and $\sigma_{^{3}\mathrm{He}} = (5333 \pm 7)$ barn [15]. Substituting these values, $N_{^{17}\mathrm{O}}/N_{^{3}\mathrm{He}} = (0.502 \pm 0.025)\%$ is obtained, where the uncertainty is dominated by that of $\sigma_{^{17}\mathrm{O}}$. The value is used to subtract the $^{17}\mathrm{O}(n,\ \alpha)^{14}\mathrm{C}$ contamination.

5.3.8 Pileup correction

In the waveform integration range of 40 μs, it is possible that the TPC accidentally detects more than one events for a single trigger, resulting in multiple signals being recorded. Such events are called as pileup events, which may affect the signal selection efficiency. A typical event display of a pileup event is shown in Figure 5.12. The image recognition algorithm is applied to the acquired data for the purpose of counting the number of observed tracks in the TPC. The event is rejected from the analysis when multiple tracks are identified. After this selection, the pileup correction amount is estimated using the Monte Carlo simulation, by taking into account all of the possible pileup event combinations.

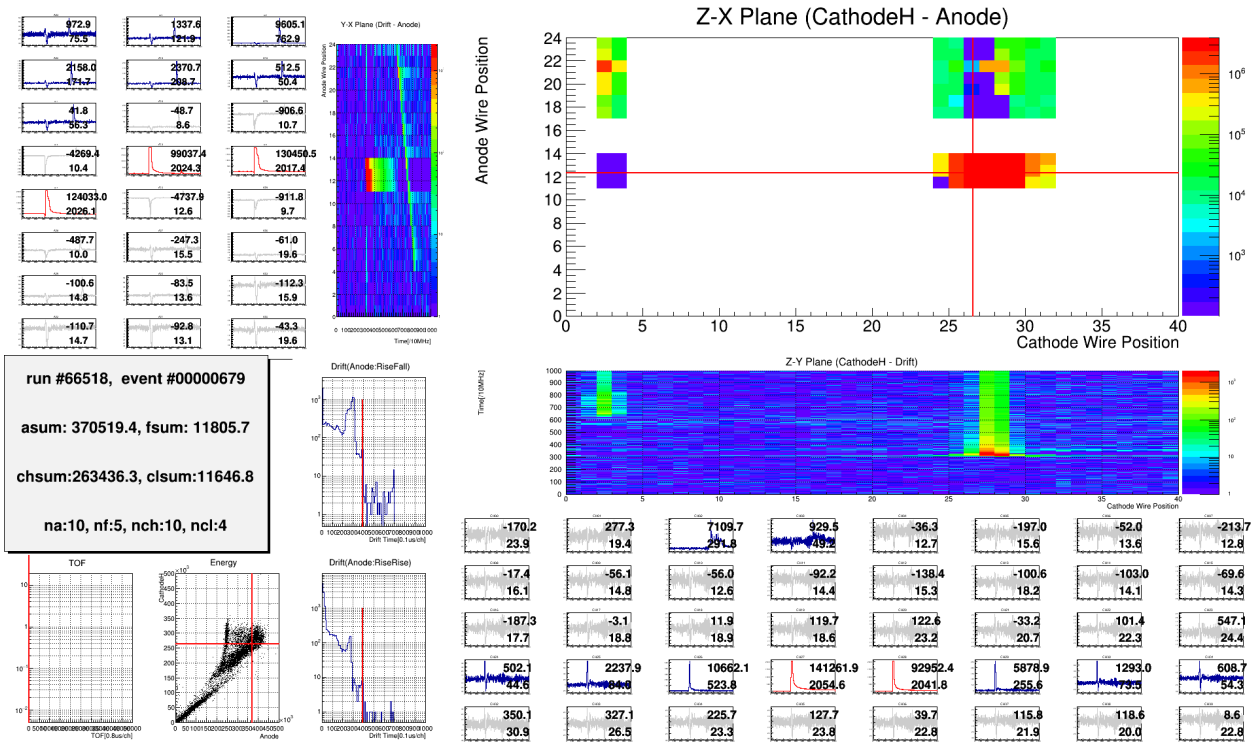

Figure 5.12: Typical event display of a pileup event. The energy deposit is shown with colors.

Table 5.2: Multi track recognition efficiencies for the simulation data.

Event		Multi track recognition efficiency		
Trigger	Following	x-y plane	z-y plane	both in x-y and z-y planes
S_β	-	0.04	0.006	0.002
S_β	S_β	0.58	0.73	0.50
S_β	$B_{\mathrm{ext}\gamma}$	0.60	0.73	0.50
S_β	$B_{\mathrm{int}\gamma}$	0.60	0.59	0.47
$B_{\mathrm{ext}\gamma}$	S_β	0.61	0.80	0.55
$B_{\mathrm{int}\gamma}$	S_β	0.53	0.56	0.42

For identifying a charged track in the TPC, the technique of image recognition using OpenCV library [44] is applied. Based on the two-dimensional event displays constructed using the anode and cathode high gain wire waveforms, the observed track number and respective position are recognized. The image recognition algorithm is described in the following.

1. Create two-dimensional event displays of the TPC in the x-y and z-y planes. The waveform voltages are shown with colors in the event displays.

2. Transform the x-y and z-y color event displays into binary images at a certain threshold.

3. Identify bounded regions surrounding pixels whose values are one.

4. Create a box which completely contains each polygon so that its size becomes minimum.

5. Identify the box as a track when the area size exceeds the threshold.

Free parameters in the algorithm, such as the binary threshold and the area size threshold, are optimized using the experimental event displays. Figure 5.13 shows some examples of the recognized tracks in the x-y plane event displays. A track detection efficiency of 99.9% can be achieved for the single beta-decay event. As the figure shows, the algorithm can detect multiple tracks when they are spatially separated in the event display, although the overlapped pile up event cannot be separated. Double tracks are detected with an efficiency of about 60% for the pileup beta-decay events. To achieve the higher pileup detection efficiency, new types of track separation algorithm, such as Hough transform, are desired.

The algorithm performance is estimated using the Monte Carlo simulation, in which two waveforms are superimposed with a random delay time to reproduce the pileup event. Table 5.2 lists the recognition efficiencies of the algorithm for the simulation data. In our analysis, the event is rejected from the signal events when more than one tracks are recognized both in the x-y and z-y event displays. About half of the pileup events can be rejected using the recognition algorithm, although 99.8% of the single beta-decay events survives.

5.4 ^{3}He number density determination

The ^{3}He pressure in the TPC is required to be measured with an accuracy of 0.1% for evaluating the total neutron fluence in the TPC. However, the typical ^{3}He pressure is about 100 mPa, which cannot

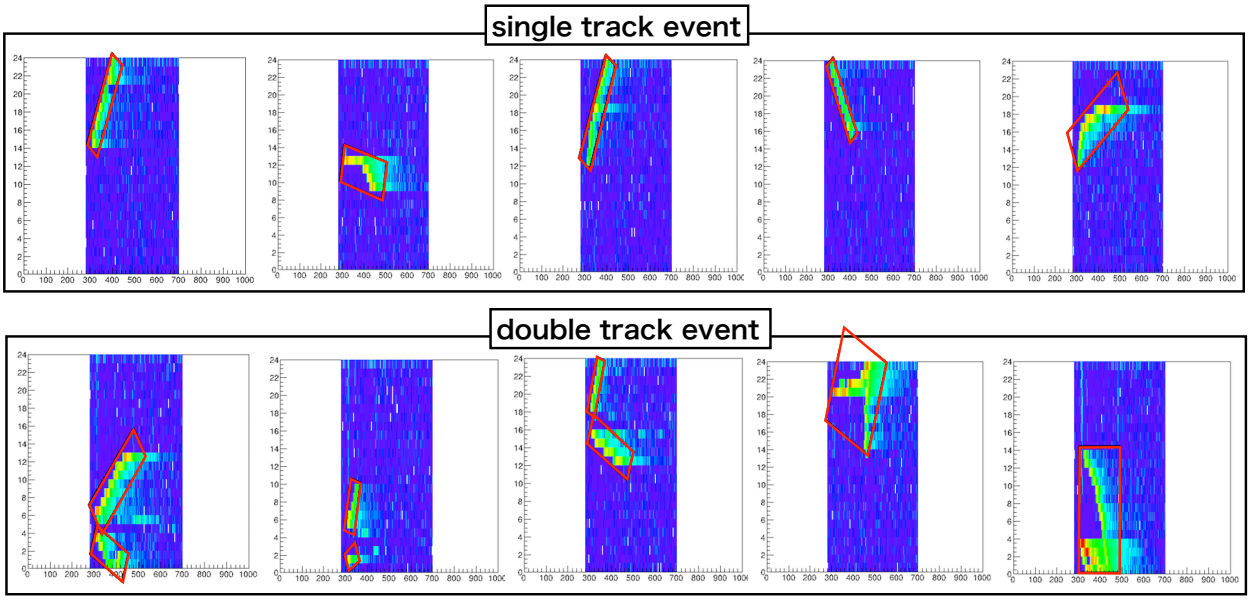

Figure 5.13: Examples of recognized tracks in the x-y plane event displays for the single track events (top) and the double track events (bottom). The recognized track is expressed as a red box. The algorithm can detect multiple tracks when they are completely separated in the event display. However, when they are partially overlapped with each other, the algorithm cannot separate them.

be directly measured by a pressure gauge with the accuracy. We therefore independently evaluated the number density of ^{3}He (1) injected from a ^{3}He cylinder and (2) contained in the operation helium gas, and summed them to evaluate the total number density in the TPC. Each method is described in the following.

5.4.1 Evaluation of injected ^{3}He pressure

As described in Section 2.12, ^{3}He gas is expanded from the Im (V_{buffer}) region to the Im, I1, I8, and ITPC regions (V_{TPC}). The schematic drawing of the expansion method is shown in Figure 5.14. The ^{3}He pressure in V_{buffer} is about 1 kPa, which can be directly measured with about 0.01% accuracy. The volume ratio of V_{buffer} and V_{TPC} is measured in advance with about 0.01% accuracy using ^{4}He gas. Assuming the helium gas to be an ideal gas, the injected ^{3}He pressure in the TPC is calculated with about 0.1% accuracy using Boyle's Law. In this estimation, the effect of the discrepancy between an ideal gas and a real gas is also considered (see Section 6.3).

5.4.2 Evaluation of ^{3}He pressure in operation He gas

The ^{4}He cylinder used in this experiment is known to contain about 0.1 ppm ^{3}He gas. Assuming 85 kPa ^{4}He pressure in the TPC, the contaminated ^{3}He pressure corresponds to 85 kPa $\times$ 0.1 ppm = 8.5 mPa. Since we inject about 100 mPa ^{3}He directly from the ^{3}He cylinder, the contamination

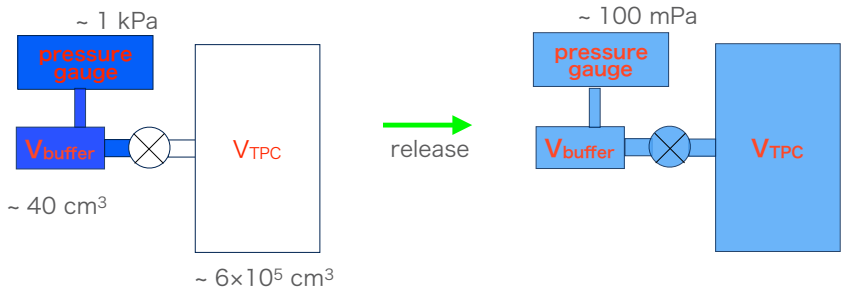

Figure 5.14: Schematic drawing of the volume expansion method. A ^{3}He gas at 1 kPa ^{3}He is stored in a buffer region (40 cm^3), and is expanded to the TPC volume ($\sim 6 \times 10^5$ cm^3).

is not negligible and should be measured accurately. We used 4 cylinders, and the contamination amount is evaluated for each cylinder using two independent methods as described in the following.

- Mass spectrometer method
  One method is to analyze the ^{3}He/^{4}He ratio of the cylinder gas using a mass spectrometer at the University of Tokyo [30]. The mass spectrometer is calibrated by a standard helium gas sample known as Helium Standard of Japan (HESJ) [45], whose ^{3}He/^{4}He ratio is evaluated by our group to be (27.36 ± 0.11) ppm [46]. The calibration measurement is conducted for at least two cycles to monitor the spectrometer operation. The precision of the ^{3}He/^{4}He ratio measurement is a few percent, which is currently limited by the spectrometer output fluctuation.

- Flux method
  The other method is to extrapolate the proportional relationship between the $^3\mathrm{He}(n,\ p)^3\mathrm{H}$ event rate and the ^{3}He pressure in the TPC. Multiple gas data with different injected ^{3}He pressures are combined to evaluate the coefficient of proportion. Figure 5.15 shows the correlation between the $^3\mathrm{He}(n,\ p)^3\mathrm{H}$ event rate and the injected ^{3}He pressure in the TPC. The contamination ^{3}He pressure from the ^{4}He cylinder can be expressed as the intercept point in the x axis. The extrapolation is independently conducted for each cylinder.

Figure 5.16 shows the evaluated ^{3}He ratio in each ^{4}He cylinder. The results of both methods are consistent with each other ($\chi^2/\mathrm{NDF} = 1.14$), although the mass spectrometer method currently gives better precision. The result of the mass spectrometer measurement is used to evaluate the total ^{3}He pressure in the TPC.

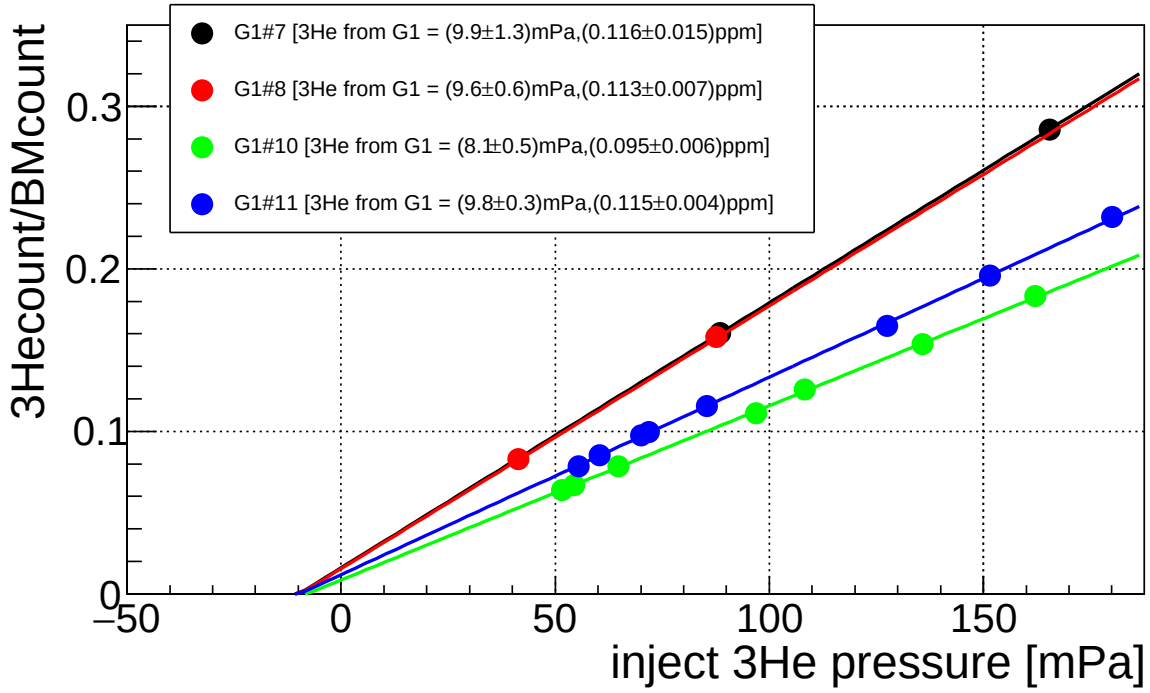

Figure 5.15: $^3\mathrm{He}(n,\ p)^3\mathrm{H}$ event flux as a function of injected $^3\mathrm{He}$ pressure. Each point corresponds to a single gas data. The intercept point in the x axis indicates the $^3\mathrm{He}$ pressure from the $^4\mathrm{He}$ cylinder.

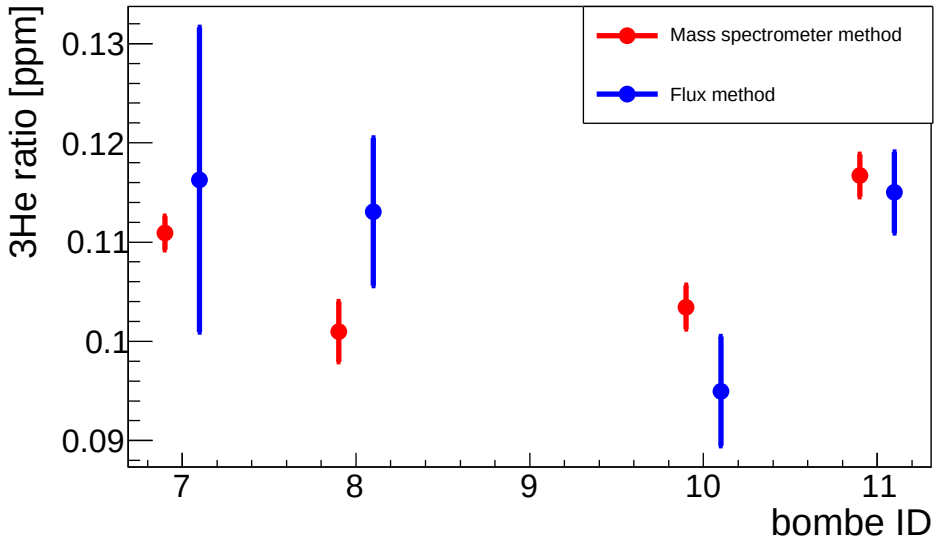

Figure 5.16: Results of the $^3\mathrm{He}/^4\mathrm{He}$ ratio measurements using the mass spectrometer method (red) and flux method (blue). They are consistent with each other within their respective uncertainties ($\chi^2/\mathrm{NDF} = 1.14$).

Chapter 6

Results

The corrections and uncertainties for each parameter in Eq. (1.27) are described in this chapter. The analysis result of τ_n is also discussed.

6.1 Uncertainties for the neutron beta-decay events (S_β)

- Upstream γ-ray correction from LiF plates
  The γ-rays coming from the SFC undergoes Compton scattering in the TPC, which becomes a background for beta-decay ($B_{\mathrm{ext}\gamma}$) as described in Section 5.1. Although this background can be subtracted for the most part by the TOF subtraction algorithm (see Section 5.3.1), a fraction of the γ-ray is expected to be stopped by a neutron shutter, or 5 mm-thick LiF plate, in the shutter-closed mode. Therefore, the background rate in the shutter-closed mode is not same as that in the shutter-open mode any more. The effect is estimated using Phits [39] and Geant4 [32] [33] [34]: The position, momentum, and energy distribution of γ-rays at the LiF plate position is evaluated by the Phits simulation, while the interaction between the γ-ray and the LiF plate is estimated by the Geant4 simulation.

- SFC S/N
  Although neutron bunches are formed by the SFC as described in Figure 2.7, neutrons also exist outside of the bunch region with an average contrast ratio of 1/422, because of the imperfectness of the spin flipping and reflection at the SFC. The event selection efficiency decreases for neutron beta-decays that decay close to the upstream or downstream edge of the TPC. The acceptance depends on the track length of the event, thus the effects for beta-decay and $^3\mathrm{He}(n,\ p)^3\mathrm{H}$ do not cancel as shown in Figure 6.1. As the figure shows, The selection efficiencies degrade at around $z = \pm 500$ mm, which corresponds to the edge of the TPC sensitive area.

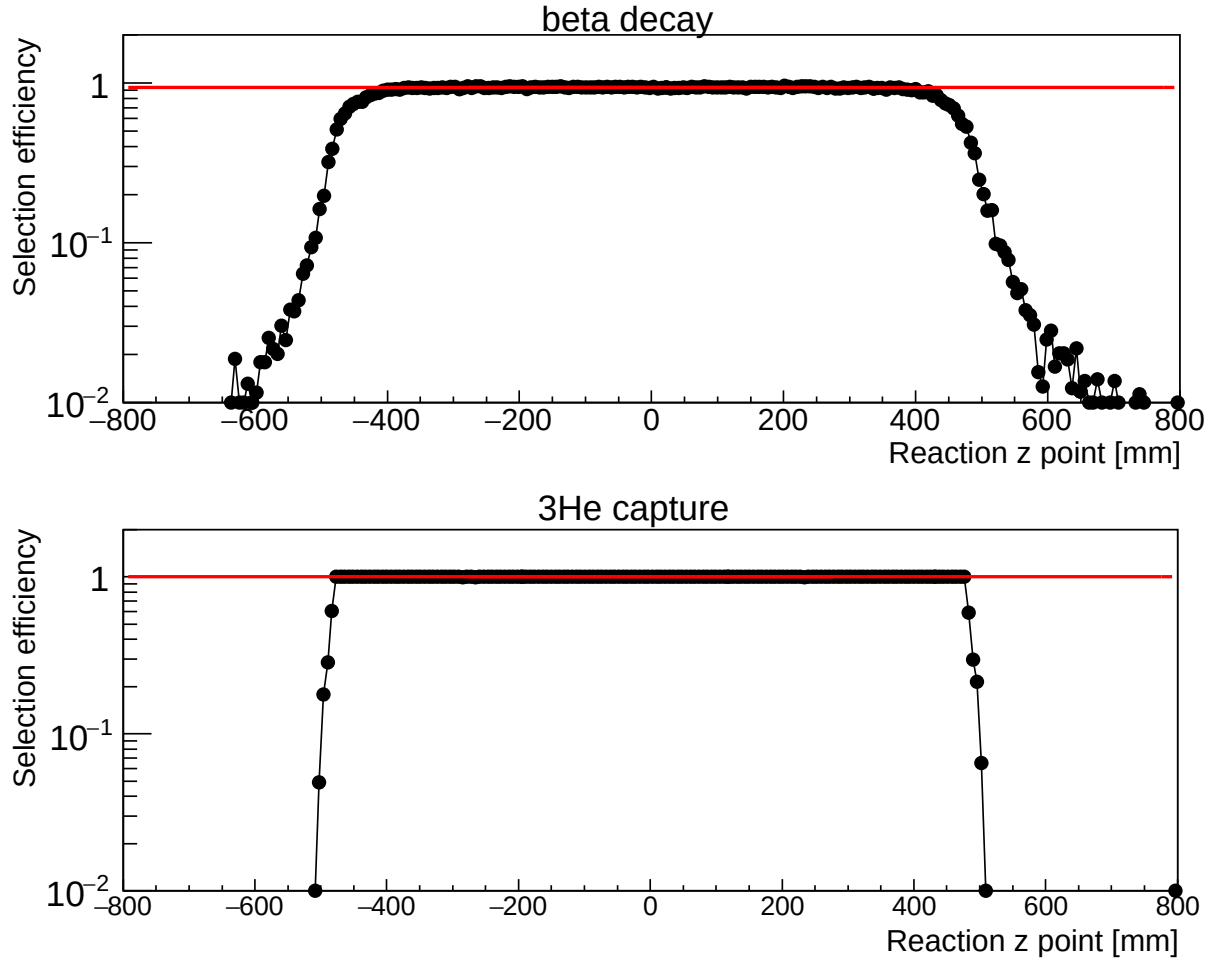

Figure 6.1: Signal selection efficiencies for the beta-decay events (top) and the $^3\mathrm{He}(n,\ p)^3\mathrm{H}$ events (bottom) as a function of the reaction z point. The red line shows the average efficiency between -280 mm < z < 280 mm. The decrease of the selection efficiencies starts at around the $z = \pm 500$ mm region.

6.2 Uncertainties for the neutron beta-decay selection efficiency (ε_β)

- Drift distortion
  Due to the asymmetrical structure of the TPC in the y direction, the drift velocity has a significant non-uniform dependence along the y direction. It gives a systematic uncertainty for the beta-decay selection efficiency because the drift time parameter is used as a purity cut. The non-uniformity is measured using the cosmic rays events assuming that each of their tracks forms a straight line. The drift time is defined as the time width from the veto scintillator hit to the waveform rise time. The ionization y position of channel i anode wire (y_i) is defined as
  $$y_i = y_{\mathrm{MWPC}} - L_{\mathrm{TPC}} \times \frac{i - \mathrm{MINHIT} - 1}{\mathrm{HITNUM} - 2}, \tag{6.1}$$
  where y_{MWPC}=150 mm is the MWPC y position and L_{TPC}=300 mm is the TPC y length. The drift velocity can be evaluated by differentiating the drift time. Figure 6.2 shows the drift time and drift velocity distribution as a function of the y position in the TPC. The non-uniformity of the drift velocity along with the y direction is observed. The drift velocity distortion (dv/dy) is evaluated to be 0.011 μs, which gives a drift velocity distortion of 20% between the upper and lower region of the TPC. The systematic uncertainty of the drift distortion effect is estimated by implementing this distortion in the detector simulation.

- Proton w value
  It is experimentally known that the w value, the average energy to create an electron-ion pair, is independent of the kinetic energy above a few MeV for an α particle and a few keV for an electron [47]. In the Monte Carlo simulation, the w value is implemented as the mean value in CO_2 and He gases, independent of the electron energy. However, in the low energy region, it is reported that the w values for charged particles increase, such as an electron in CO_2 gas [48] and a proton in water vapor [49] as shown in Figure 6.3 and 6.4, respectively. In the gas composition of the TPC, it is possible that the w value increase causes a significant effect on protons from neutron beta-decays, because the proton has a kinetic energy of less than 1 keV. The accurate w value dependence on the kinetic energy of a charged particle is unknown in the low energy region. The upper limit of this effect is estimated by the special beta-decay simulation in which a proton kinetic energy is set to be zero. This is equivalent to setting infinite w value for a proton, thus giving the upper limit of this effect.

- Neutron polarization
  Although the neutron beam is polarized at the SFC position, the polarization condition at the TPC position is totally unknown. A polarized neutron beam undergoes an asymmetric beta-decay with respect to the polarization direction as described in Section 4.3.1. For example, when the neutron beams are polarized in the vertical direction, the drift length of electrons from beta-decay would change and the attenuation effect would produce a systematic effect for the detection efficiency. However, the polarization of the neutron beams at the TPC position is yet to be measured. In order to estimate the upper limit of this effect, the detection efficiency

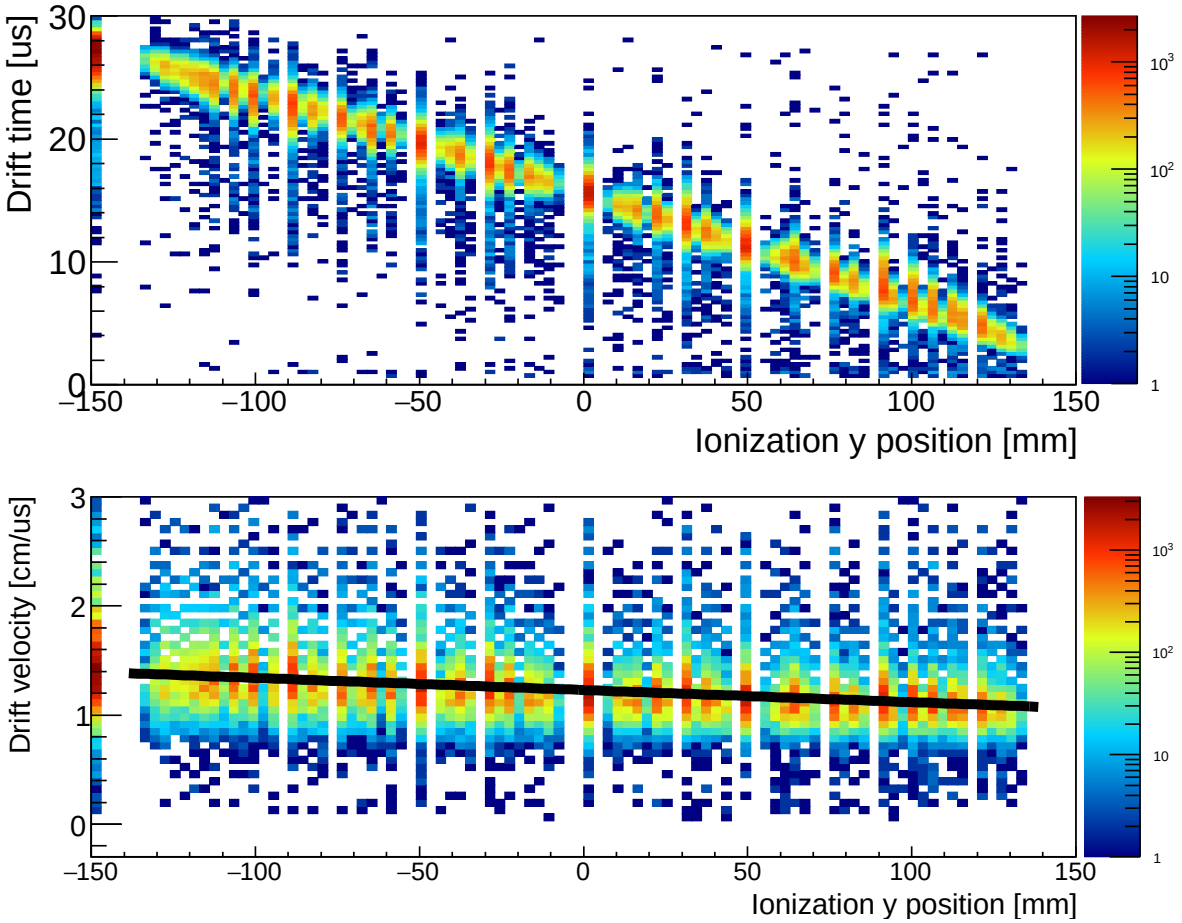

Figure 6.2: Electron drift time (top) and drift velocity (bottom) distribution of the cosmic rays events as a function of the ionization y position in the TPC. The bottom plot is obtained by taking the derivative of the y position in the top plot with respect to the drift time. The non-uniformity of the drift velocity along with the y direction is observed.

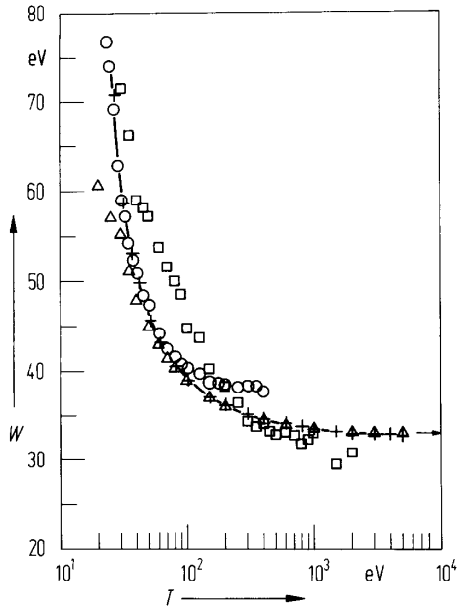

Figure 6.3: Average energy to create an electron-ion pair (w value) for an electron in CO_2 gas. The horizontal axis shows the kinetic energy of the electron. It was studied by E. Waibel and B. Grosswendt in 1991 [48]: (+), (○), (□) are independent experimental results, (△) Monte Carlo simulation, (-) fitting function.

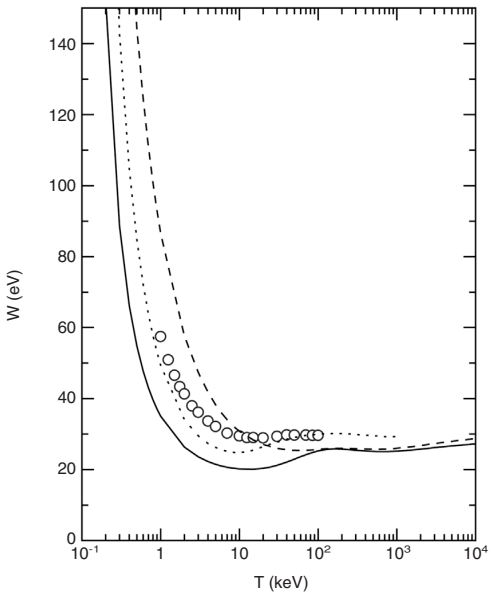

Figure 6.4: Average energy to create an electron-ion pair (w value) for a proton in water vapor. The horizontal axis shows the kinetic energy of the proton. It was studied by G. Willems $et\ al.$ in 2002 [49]: (○) experimental result, (—), ($\cdots$), and (– –) theoretical curves with different cross section models.

for neutron beta-decay is studied in the Monte Carlo simulation by changing the polarization direction, and it is found to have negligible effect on our analysis.

6.3 Uncertainties for the $^3\mathrm{He}$ number density (ρ)

- Chamber deformation by pressure
  The TPC volume is precisely measured by the volume expansion method as described in Section 5.4.1. However, during the volume ratio measurement, the $^4\mathrm{He}$ pressure filling the TPC volume is a few hundred Pa, resulting in a deformation of the vacuum chamber due to the atmospheric pressure surrounding the chamber. This means the TPC volume is slightly different between he volume ratio measurement and the lifetime measurement, which changes the $^3\mathrm{He}$ number density in the TPC. The deformation can be calculated using the Young's modulus parameter of the chamber material (aluminum and stainless steel). The deformation Δy of a rectangular plate with a Young's modulus E, a thickness t, applied pressure P, and a short side length b, is expressed as

$$\Delta y = \beta P \frac{b^4}{Et^3}, \tag{6.2}$$

  where β is a function of the ratio of the short to the long side length of the plate [50]. In our case, the atmospheric pressure causes the volume deviation of 2300 cm^3 at most, or 0.3% of the total volume.

- Virial coefficient
  For the $^3\mathrm{He}$ density calculation, the He and $\mathrm{CO_2}$ gases are assumed to be ideal gases and the gas state equation is used. For a real gas, however, molecules attract each other, which is taken into account in the van der Waals equation:

$$\left(P + \frac{a}{V^2}\right)(V - b) = RT. \tag{6.3}$$

  In this equation, V is a normalized volume. The equation can be rewritten as

$$\frac{PV}{RT} = 1 + \frac{B}{V} + \frac{C}{V^2} + \cdots \tag{6.4}$$

  Assuming $B = (127 \pm 13)$ cm^3/mol for $\mathrm{CO_2}$ gas at T =30° [51], and $B = (11.79 \pm 0.06)$ cm^3/mol for He gas at T =25° [52], the deviation from an ideal gas is expected to be about 0.5%.

6.4 Analysis results of parameters

The analysis results of parameters in Eq. (1.27) is shown in Table 6.1 for S_β, Table 6.2 for $S_{^3\mathrm{He}}$, Table 6.3 for ε_β, Table 6.4 for $\varepsilon_{^3\mathrm{He}}$, and Table 6.5 for ρ, respectively. The amount of each uncertainty is plotted in Figure 6.5.

Table 6.1: Summary of the S_β uncertainty: Fill66

Term	Value	Correction	Uncertainty	Correction[%]	Uncertainty[%]
S_β before correction	14175	0	$\pm$206 (stat.)	0.000	$\pm$1.505 (stat.)
Gas background	13685	-490	$\pm$204 (stat.)	-3.586	$\pm$1.491 (stat.)
Upstream γ-ray correction from LiF	13685	0	$\pm$ 3	0.000	$\pm$0.020
LiF γ-ray spectrum	13685	0	$\pm$ 18	0.000	$\pm$0.128
SFC S/N	13669	-16	$^{+16}_{-0}$	-0.118	$^{+0.118}_{-0.000}$
CO_2 recoil	13669	0	$^{+0}_{-39}$	0.000	$^{+0.000}_{-0.283}$
^{3}He event contamination	13665	-3	$^{+3}_{-0}$	-0.025	$^{+0.025}_{-0.000}$
Pileup	13670	5	$\pm$ 8	0.034	$\pm$0.060
S_β corrected	13670		$\pm$ 290 (stat.) $^{+26}_{-43}$ (sys.)		$\pm$2.118 (stat.) $^{+0.187}_{-0.317}$ (sys.)

Table 6.2: Summary of the $S_{^3\mathrm{He}}$ uncertainty: Fill66

Term	Value	Correction	Uncertainty	Correction[%]	Uncertainty[%]
$S_{^3\mathrm{He}}$ before corrected	346777	0	$\pm$593 (stat.)	0.000	$\pm$0.174 (stat.)
Scatter event	345936	-841	$\pm$60 (stat.)	-0.246	$\pm$0.018 (stat.)
Beta decay event contamination	345864	-72	$^{+72}_{-0}$	-0.021	$^{+0.021}_{-0.000}$
SFC S/N	345449	-415	$^{+415}_{-0}$	-0.122	$^{+0.122}_{-0.000}$
$^{14}\mathrm{N}(n,\ p)^{14}\mathrm{C}$ contamination	343596	-1853	$\pm$ 191	-0.542	$\pm$0.056
$^{17}\mathrm{O}(n,\ \alpha)^{14}\mathrm{C}$ contamination	341844	-1751	$\pm$ 88	-0.513	$\pm$0.026
Pileup	341724	-120	$^{+120}_{-0}$	-0.035	$^{+0.035}_{-0.000}$
$S_{^3\mathrm{He}}$ corrected	341724		$\pm$ 596 (stat.) $^{+486}_{-210}$ (sys.)		$\pm$0.175 (stat.) $^{+0.142}_{-0.061}$ (sys.)

Table 6.3: Summary of the ε_β uncertainty: Fill66

Term	Value	Correction	Uncertainty	Correction[%]	Uncertainty[%]
MC statistic	0.9414	0.0000	$\pm$0.0007 (stat.)	0.000	$\pm$0.079 (stat.)
Waveform shape	0.9414	0.0000	$^{+0.0004}_{-0.0006}$	0.000	$^{+0.046}_{-0.063}$
Low energy cut	0.9414	0.0000	$^{+0.0010}_{-0.0017}$	0.000	$^{+0.107}_{-0.179}$
High energy cut	0.9414	0.0000	$^{+0.0024}_{-0.0035}$	0.000	$^{+0.261}_{-0.371}$
Drift distortion	0.9414	0.0000	$\pm$ 0.0010	0.000	$\pm$0.110
Anode wire efficiency	0.9414	0.0000	$^{+0.0000}_{-0.0000}$	0.000	$^{+0.001}_{-0.001}$
Beam shift	0.9414	0.0000	$\pm$ 0.0009	0.000	$\pm$0.099
Proton w value	0.9414	0.0000	$\pm$ 0.0011	0.000	$\pm$0.113
Neutron polarization	0.9414	0.0000	$\pm$ 0.0002	0.000	$\pm$0.023
Multi track rejection	0.9396	-0.0018	$^{+0.0018}_{-0.0000}$	-0.191	$^{+0.191}_{-0.000}$
ε_β corrected	0.9396		$\pm$0.0007 (stat.) $^{+0.0037}_{-0.0043}$ (sys.)		$\pm$0.079 (stat.) $^{+0.391}_{-0.457}$ (sys.)

Table 6.4: Summary of the $\varepsilon_{^3\mathrm{He}}$ uncertainty: Fill66

Term	Value	Correction	Uncertainty	Correction[%]	Uncertainty[%]
MC statistics	0.9999	0.0000	$\pm$0.0000 (stat.)	0.000	$\pm$0.003 (stat.)
Energy cut	0.9999	0.0000	$\pm$ 0.0000	0.000	$\pm$0.000
$\varepsilon_{^3\mathrm{He}}$ corrected	0.9999		$\pm$ 0.0000 (stat.) $^{+0.0000}_{-0.0000}$ (sys.)		$\pm$0.003 (stat.) $^{+0.000}_{-0.000}$ (sys.)

Table 6.5: Summary of the ρ uncertainty: Fill66

Term	Value	Correction	Uncertainty	Correction[%]	Uncertainty[%]
Inject ^{3}He amount	2086.04	0.00	$\pm$ 6.57	0.000	$\pm$0.287
Virial coefficient	2089.76	3.72	$\pm$ 0.01	0.163	$\pm$0.000
Thermal transpiration	2088.78	-0.98	$\pm$ 0.10	-0.043	$\pm$0.004
^{3}He gas isotopic purity	2088.78	0.00	$^{+0.00}_{-1.04}$	0.000	$^{+0.000}_{-0.046}$
^{3}He gas chemical purity	2088.78	0.00	$^{+0.00}_{-0.12}$	0.000	$^{+0.000}_{-0.005}$
^{3}He from G1 ^{4}He gas	2290.82	202.04	$\pm$ 6.07	8.835	$\pm$0.265
Chamber deformation (pressure)	2287.31	-3.51	$\pm$ 3.51	-0.154	$\pm$0.154
Chamber deformation (temperature)	2286.82	-0.49	$\pm$ 0.49	-0.021	$\pm$0.021
Preamplifier heat generation	2286.82	0.00	$\pm$ 0.49	0.000	$\pm$0.022
ρ corrected	2286.82		$\pm$ 0.00 (stat.) $^{+9.64}_{-9.69}$ (sys.)		$\pm$0.000 (stat.) $^{+0.421}_{-0.424}$ (sys.)

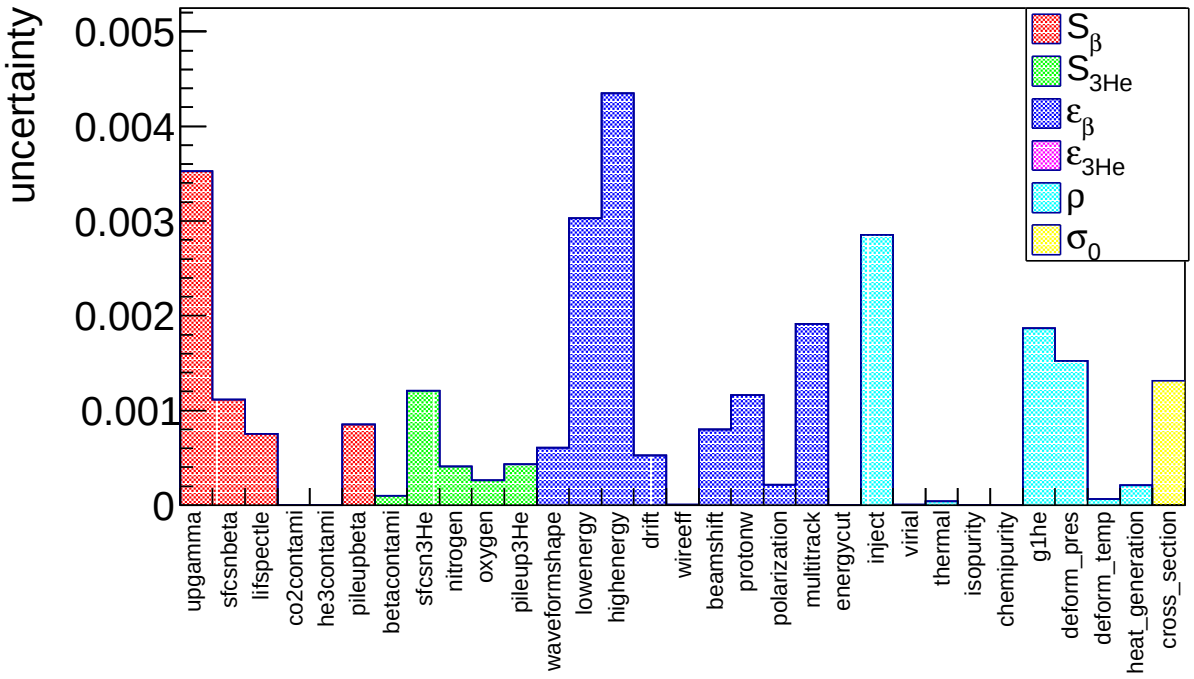

Figure 6.5: Breakdown of the uncertainties given for Fill96.

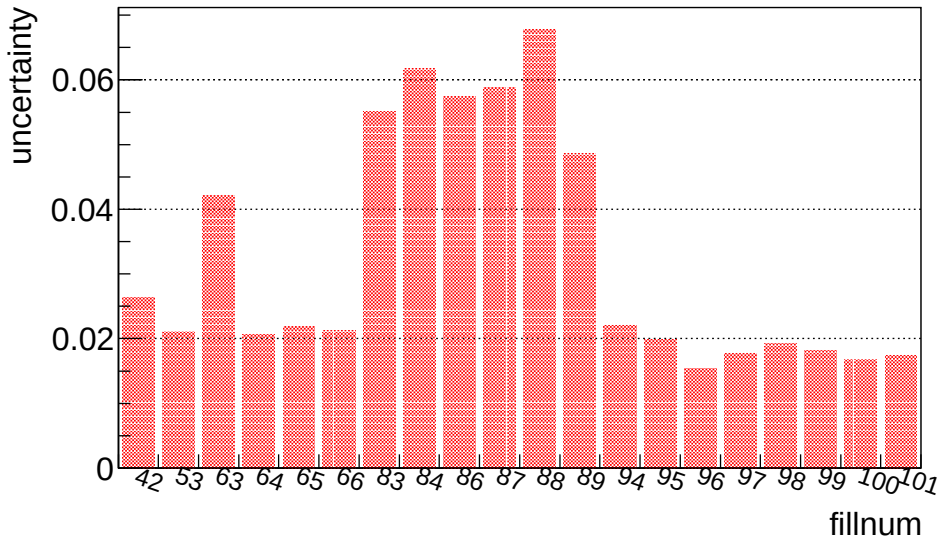

Figure 6.6: Statistical uncertainty for each gas fill data.

6.5 Combined result

The statistical and systematic uncertainties of the neutron lifetime for each gas fill data are shown in Figure 6.6 and Figure 6.7, respectively. The neutron lifetime evaluated for each gas fill condition is plotted in Figure 6.8. The averaged result combining the same year is listed in Table 6.6. They are consistent with each other, and the overall averaged value is $898.8 \pm 4.7\ (\mathrm{stat.})\ ^{+7.7}_{-8.9}\ (\mathrm{sys.})$ s. Our result is shown in Figure 6.9 along with previous measurements by others.

Table 6.6: Comparison of the lifetime value combined with the same year gas data.

Year	Measured neutron lifetime [s]
2014A	$942.1 \pm 24.9\ (\mathrm{stat.})\ ^{+14.0}_{-8.3}\ (\mathrm{sys.})$
2015A	$896.4 \pm 18.9\ (\mathrm{stat.})\ ^{+5.9}_{-5.7}\ (\mathrm{sys.})$
2016A	$887.9 \pm 10.5\ (\mathrm{stat.})\ ^{+6.3}_{-6.1}\ (\mathrm{sys.})$
2017A	$911.3 \pm 21.3\ (\mathrm{stat.})\ ^{+8.3}_{-10.7}\ (\mathrm{sys.})$
2017B	$899.0 \pm 5.7\ (\mathrm{stat.})\ ^{+7.9}_{-9.9}\ (\mathrm{sys.})$

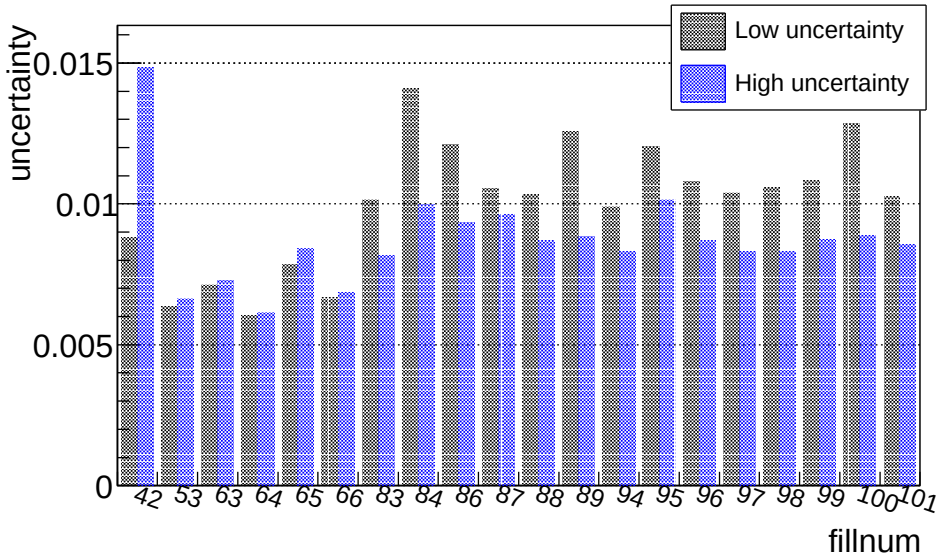

Figure 6.7: Systematic uncertainty for each gas fill data.

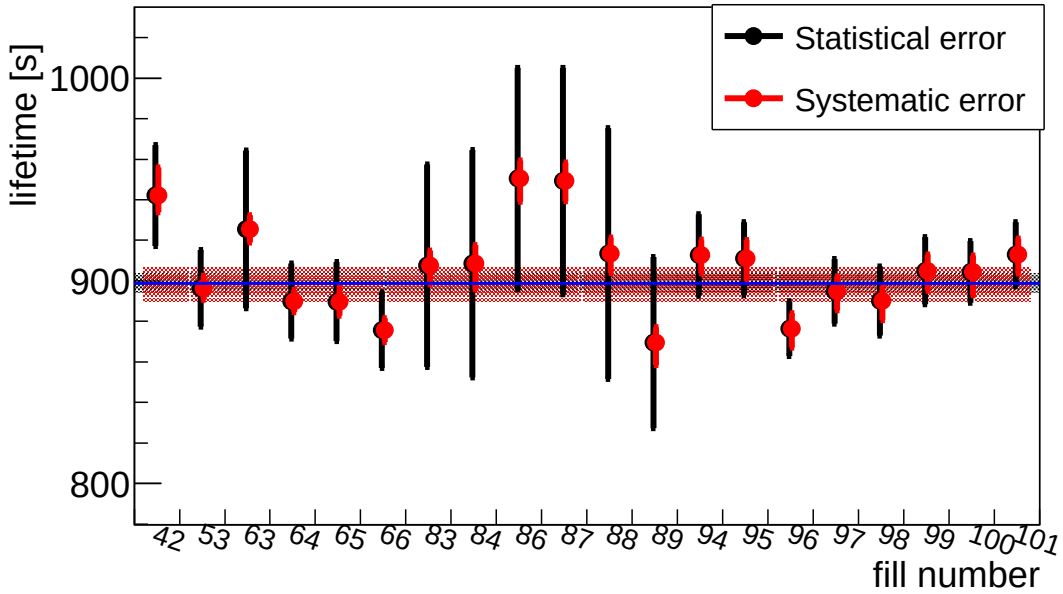

Figure 6.8: Result of the neutron lifetime for each gas fill data and their averaged value. Our overall averaged lifetime, shown as a blue line, is 898.8 ± 4.7 (stat.) $^{+7.7}_{-8.9}$ (sys.) s ($\chi^2/\mathrm{ndf} = 12.9/19 = 0.68$).

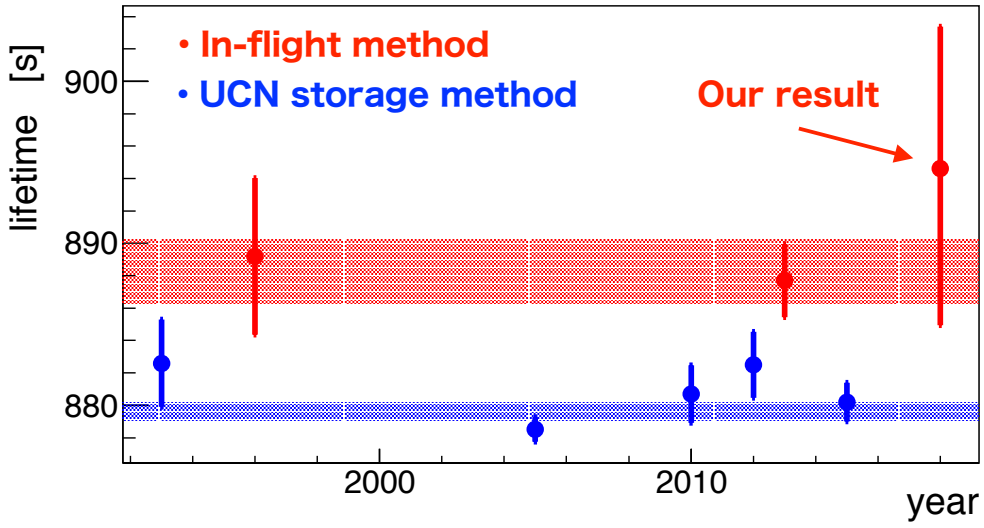

Figure 6.9: Comparison of our result with other neutron lifetime measurements [6].

Chapter 7

Summary and discussion

7.1 Summary

The precise neutron lifetime measurement was conducted using the pulsed neutron beams at J-PARC. The spin flip chopper is developed to form the neutron bunches from the pulsed beams. The signal events are counted only when each of the neutron bunches is completely inside the TPC sensitive region. As a result, the 4π solid angle acceptance is guaranteed for the signal events in addition to suppressing the background. As a detector, the time projection chamber made of the low radiation material is also developed. It is filled with helium, CO_2, and a small amount of $^3\mathrm{He}$ gases. It detects both the neutron beta-decay events and the $^3\mathrm{He}(n,\ p)^3\mathrm{H}$ events at the same time. The neutron lifetime is expressed using the numbers of these two kinds of events. Furthermore, The Monte Carlo simulation of the TPC is developed. Implementing the accurate physics models to describe the detector response, the simulation can reproduce the experimental distribution well. The signal selection efficiencies are evaluated using this simulation with an uncertainty of below 0.5%.

We started the data taking at 2014 and continued by 2018. Combining the four years' data, the total data taking time with the neutron beams is 40 days, and 6.0×10^{11} neutrons entered the TPC. The averaged result of the measured neutron lifetime is $898.8 \pm 4.7\ (\mathrm{stat.})\ ^{+7.7}_{-8.9}\ (\mathrm{sys.})$ s. This is the first result of the neutron lifetime measurement that obtained a 1% level of the precision using the pulsed neutron beams. Although our result is closer to the averaged result of the in-flight method, it is also consistent with the averaged result of the UCN storage method. We do not yet know what causes the discrepancy between the in-flight method and the UCN storage method: whether it is simply caused by missing some systematic effects or it indicates new physics beyond our understanding. By resolving this problem, the future potential of improving the V_{ud} precision can be proposed as well as increasing the reliability of the BBN model. Our result is not precise enough to give any indication of the discrepancy puzzle, hence further precise measurement is significantly required. We have to improve both the statistical and systematic uncertainties to achieve our eventual goal precision of 1 second. Several upgrade plans are proposed and ongoing in our goal.

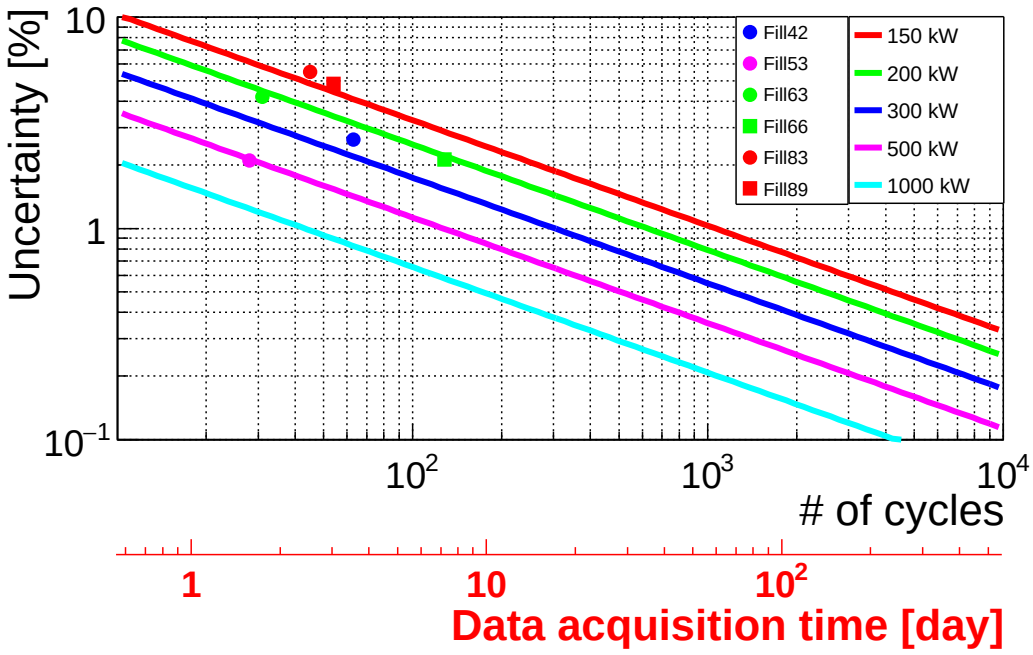

Figure 7.1: Expected statistical uncertainty as a function of the total data acquisition time. The color represents the accelerator operation power, and some of the experimental results are also expressed as points in the figure.

7.2 Upgrade plans

- SFC upgrade
  After the increase of the accelerator operation power, the neutron flux in the TPC is expected to be 2.5×10^7 neutrons/s for the 1 MW power operation. As shown in Figure 7.1, 600 days of data taking is required to achieve 0.1% statistical uncertainty by scaling our results statistically. Therefore, it would be preferable to increase the neutron beam flux in the TPC by several times. The current beam size, 2.5 cm $\times$ 2 cm, is significantly limited by the beam transportation system, such as magnetic super mirrors and flipper coils in the SFC. It is planned to increase the sizes of these devices so that the beam size in the TPC would be 3 cm $\times$ 10 cm. Two upgrade plans are currently proposed as summarized in Table 7.1. After these improvements, the total neutron flux in the TPC is expected to be 1.33×10^8 for the 1MW accelerator operation, which is 5.3 times larger than the current one. Under this operation condition, we can achieve a statistical uncertainty of 0.1% by taking data for 100 days.

- Low-pressure operation
  In the current analysis, the gas-induced background is one of the main backgrounds for beta-decays, which exists about a few percent for beta-decay in the signal region. Since this background comes from a neutron scattering with gas molecules in the TPC, the amount is expected to decrease when the operation gas pressure is reduced below 100 kPa. For this purpose, it is planned to operate the TPC with the low-pressure gas condition. We already

Table 7.1: Expected neutron flux in the TPC for two prospective upgrade setups. The neutron flux is normalized by the accelerator design operation power of 1 MW.

Setup	Collimator size	Vertical mirror	Reflection mirror	Coil	Neutron flux at TPC	Ratio
0 (default)	25×20 mm^2	no	$140\times30\times0.7$ mm^3	35×35 mm^2	2.50×10^7 /s	1
1	100×30 mm^2	yes	$200\times100\times0.3$ mm^3	35×35 mm^2	3.96×10^7 /s	1.58
2	100×30 mm^2	yes	$200\times100\times0.3$ mm^3	$> 40\times40$ mm^2	1.33×10^8 /s	5.32

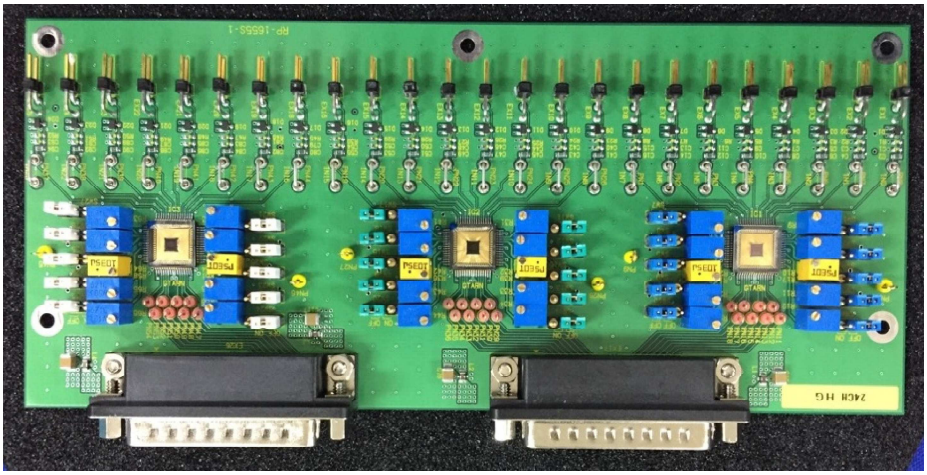

Figure 7.2: Picture of a new preamplifier. Input wire signals of 24 channels are amplified per board.

took the data in the 50 kPa gas condition while the composition ratio was maintained. Due to the heat generation from the preamplifiers, we found the gas temperature was increased by at most 20° during the measurement, which is higher than a 15° increase at 100 kPa condition. Under the further low-pressure condition, the temperature would increase more, which gives a large temperature gradient in the TPC. It gives a non-uniform ^{3}He distribution inside the TPC, which affects the estimation of the ^{3}He number density. In order to reduce this non-uniformity, a new type of preamplifier with low power-consumption, the specification of which is listed in Table 7.2, is currently developed in our group (see Figure 7.2).

Table 7.2: Specification comparison of the current and new preamplifier.

	Current preamplifier	New preamplifier
Channel	1 ch/chip	24 ch/board
Power consumption	500 mW/ch	9 mW/ch
Gain	1 V/pC	0.8 V/pC
Equivalent noise charge	∼8000	∼3000

- Thinning of the neutron shutter
  The neutron beam in the TPC can be switched on and off by the 5 mm-thick LiF shutter as

described in Section 2.4. Some of the backgrounds for the beta-decay events can be subtracted using the shutter-closed data (see Section 5.3.1). However, γ-rays from the upstream of the TPC undergo Compton scattering in the shutter with a probability of 4.8%, which causes the bias of the background subtraction between the shutter-open and shutter-closed data. The systematic uncertainty due to the effect is 0.35% for the number of beta-decayevents. The scattering probability can be reduced by lowering the composition ratio of the polytetra fluoro ethylene (PTFE) in the shutter. As as alternative, as a result of simply thinning the shutter thickness by half, the systematic uncertainty can be suppressed to be 0.1% level.

- ^{3}He density estimation
  The ^{3}He amount injected into the TPC is evaluated with a precision of 0.3%, which is currently one of the largest systematic uncertainties. The uncertainty mainly originates from the resolution of the pressure gauge. By using a new pressure gauge of Mensor CPT9000, which has a larger dynamic range (500 kPa) and better resolution (0.08%), the uncertainty can be suppressed. Furthermore, the procedure to inject ^{3}He gas into the TPC can be simplified in order to reduce the uncertainty propagation. After the improvement, the uncertainty of the injected ^{3}He number density is expected to be 0.11%.

Appendix A

Mathematical definition of analysis parameters

Mathematical definitions for the analysis parameters introduced in Section A are expressed in this appendix.

A.0.1 Waveform parameters

- PED
  A pedestal (an average voltage) level between $0\ \mu s$ to $28\ \mu s$.
- PH
  Waveform pulse height (maximum voltage from PED level).
- HIT
  A binary parameter expressing the existence of energy deposit of the wire. The HIT parameter becomes true when PH is higher than a threshold level, and false otherwise. The threshold level was set as 15 mV for anode and field, and low-gain cathode wires. For high-gain wires, we use 17.5 mV.
- RISETIME
  A time at which the waveform exceeds the threshold level for the first time.
- INT
  Integral of the waveform from PED level. The integral region was determined so as to completely contain a signal waveform. Since the drift velocity depends on the TPC gas pressure, the region was optimized as $28\mu\ s$ to $70\mu\ s$.

A.0.2 Event parameters

- TOTALENERGY = $\sum_{i \in \text{anode \& HIT}_i = \text{true}} \text{INT}_i$.
  Total energy deposit in the TPC

- MAXENERGY = $\max\{\mathrm{PH}_i | i \in \mathrm{field}\}$.
  Maximum energy deposit in the TPC

- LOCALITY = $\max\{\mathrm{PH}_i | i \in \mathrm{anode}\} / \sum_{i \in \mathrm{anode\ \&\ HIT}_i = \mathrm{true}} \mathrm{INT}_i$

- MINRISE = $\min\{\mathrm{RISETIME}_i | i \in \mathrm{anode}\ \&\ \mathrm{HIT}_i = \mathrm{true}\}$.
  Trigger timing of the TPC

- HITNUM = $\sum_{i \in \mathrm{field\ \&\ HIT}_i = \mathrm{true}} 1$.
  Number of wires detecting energy deposit

- DTIME = $\max\{\mathrm{RISETIME}_i | i \in \mathrm{anode}\,\&\,\mathrm{HIT}_i = \mathrm{true}\} - \min\{\mathrm{RISETIME}_i | i \in \mathrm{anode}\,\&\,\mathrm{HIT}_i = \mathrm{true}\} \times v_{\mathrm{drift}}$.
  Track length in y direction as a unit of time

- CENTER_A = $\left(\sum_{i \in \mathrm{anode\ \&\ HIT}_i = \mathrm{true}} i \times \mathrm{INT}_i \right) / \left(\sum_{i \in \mathrm{anode \& HIT}_i = \mathrm{true}} \mathrm{INT}_i \right)$.
  Track center position weighted by the energy deposit of wires

- MINHIT_A = $\min\{i | i \in \mathrm{anode}\ \&\ \mathrm{HIT}_i = \mathrm{true}\}$.
  The most left side (the x coordinate is minimum) wire number detecting energy deposit.

- MAXHIT_A = $\max\{i | i \in \mathrm{anode}\ \&\ \mathrm{HIT}_i = \mathrm{true}\}$.
  The most right side (the x coordinate is maximum) wire number detecting energy deposit.

- DTC_A = $\min\{|i - 12| \mid i \in \mathrm{anode}\ \&\ \mathrm{HIT}_i = \mathrm{true}\}$.
  The distance between the center wire and the most closest wires detecting energy deposit.

- DVC_A = $\min\{\mathrm{WIRENUM\_A}/2 - \mathrm{MINHIT\_A},\ \mathrm{MAXHIT\_A} - \mathrm{WIRENUM\_A}/2\}$,
  where WIRENUM_A=24, WIRENUM_F=24, WIRENUM_CH=40, and WIRENUM_CL=40.
  The distance between the center wire and the wire detecting the track origin point.

Appendix B

Thermometer specifications

The detailed specifications of the two types of thermometers (manufactured by LakeShore and Automatic Systems Laboratories) are listed in Table B.1 and Table B.2.

Table B.1: Specification of the Automatic Systems Laboratories platinum thermometer.

Monitor model	F201
Monitor manufacture	Automatic Systems Laboratories
Platinum manufacture	Netsushin and Chino
Platinum resistance	100 Ω
Uncertainty	60 mK at 298 K

Table B.2: Specification of the LakeShore platinum thermometer.

Monitor model	218
Monitor manufacture	LakeShore
Platinum manufacture	LakeShore
Platinum resistance	100 Ω
Uncertainty	105 mK at 300 K

Appendix C

Gain reduction model in a wire chamber due to the space charge effect

In this experiment, the multiplication factor of the TPC is relatively high ($\sim 10^4$) in order to achieve the high detection efficiency for the neutron beta-decay events. As a result, the linearity of the detected energy is distorted for the $^3\mathrm{He}(n,\ p)^3\mathrm{H}$ events because of a large number of space charges around the anode wires. An analytical model to describe the gain reduction is proposed [21] [41], which expresses the gain reduction factor s ($0 < s \leq 1$) as

$$s = \frac{\log\left(1 + fG_0\frac{dE}{dl}\right)}{fG_0\frac{dE}{dl}}, \tag{C.1}$$

where G_0 is the multiplication factor without the space charge effect, and dE/dl is the energy deposit density per anode wire length. In this model, the microscopic behaviour of the space charges is described by a single free parameter f. The f parameter, depending on the anode wire radius and the operation gas composition, determines the absolute saturation scale. The s value as a function of G_0 is drawn in Figure C.1.

For the purpose of experimentally verifying the model, a small multi wire drift chamber was developed as shown in Figure C.2 [41]. The proton beams at the Tandetron accelerator in the University of Tsukuba [53] were irradiated into the drift chamber. The gain reduction (s) for the proton beams was measured by comparing the detected energy with the energy deposit calculated by the Monte Carlo simulation. The model was investigated by changing (1) the anode wire voltage and (2) the proton beam angle with respect to the anode wires. The observed dependence of s was consistent with the proposed model in Eq. (C.1) as shown in Figure C.3. The optimum parameter to reproduce the experimental gain reduction was evaluated to be $f = (1.8^{+0.5}_{-0.4}) \times 10^{-3}$ mm/MeV.

Figure C.4 shows the energy deposit distribution before and after the correction using the model. This gain reduction model is implemented in the Monte Carlo simulation for the neutron lifetime measurement. For the purpose of updating the model, it is planned to measure the saturation effect with different ion beams and gas compositions.

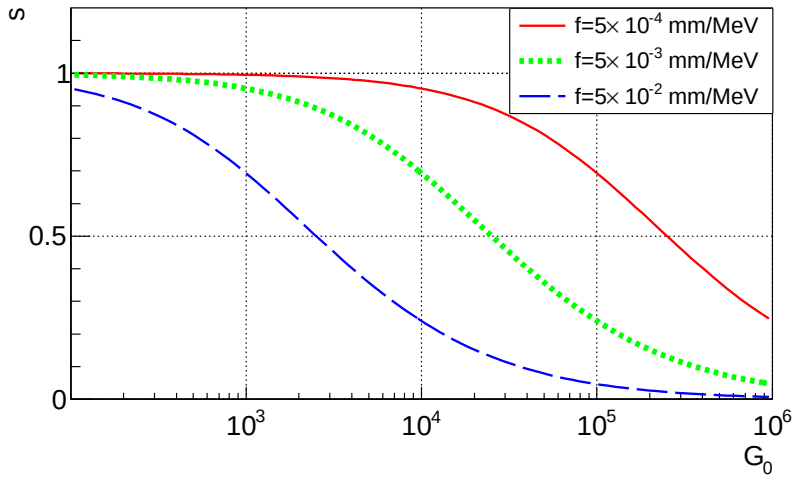

Figure C.1: Proposed model function of the gain reduction factor (s) as a function of the multiplication factor (G_0) [41]. In this plot, the typical energy deposit density $dE/dl = 20$ keV/mm is assumed.

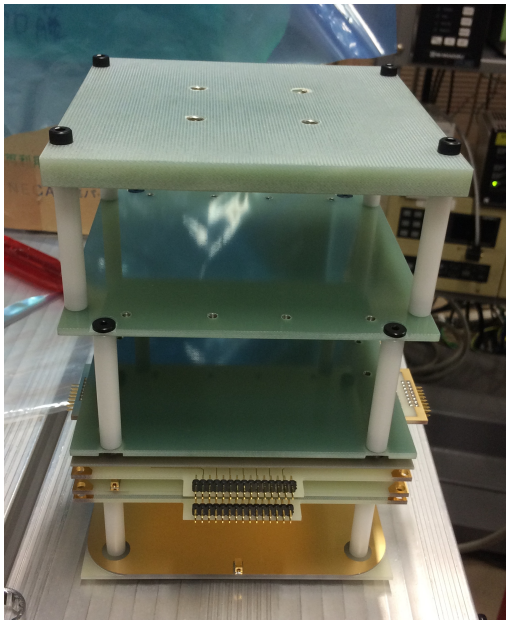

Figure C.2: Picture of the multi wire drift chamber. The chamber is composed of epoxy glass laminate (G10). The dimensions of the sensitive region are 13 cm $\times$ 13 cm $\times$ 6 cm.

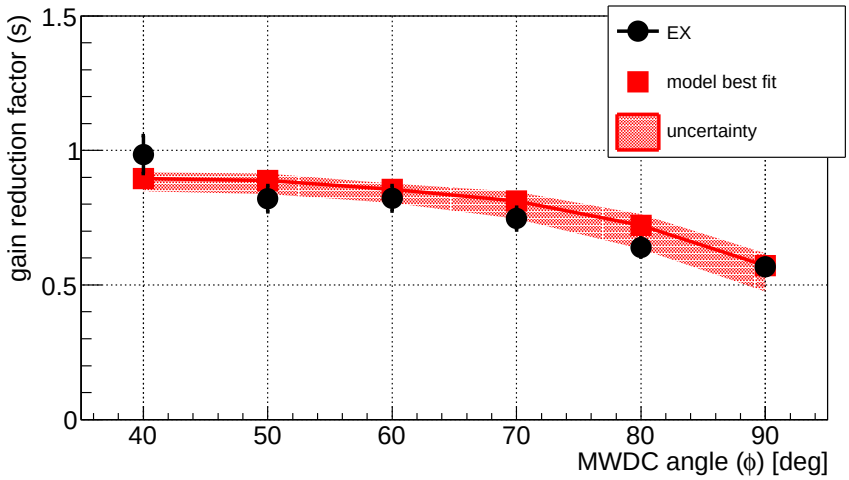

Figure C.3: Measured gain reduction factor along with the proposed best fit model curve [41]. The horizontal axis represents the proton beam angle with respect to the anode wires.

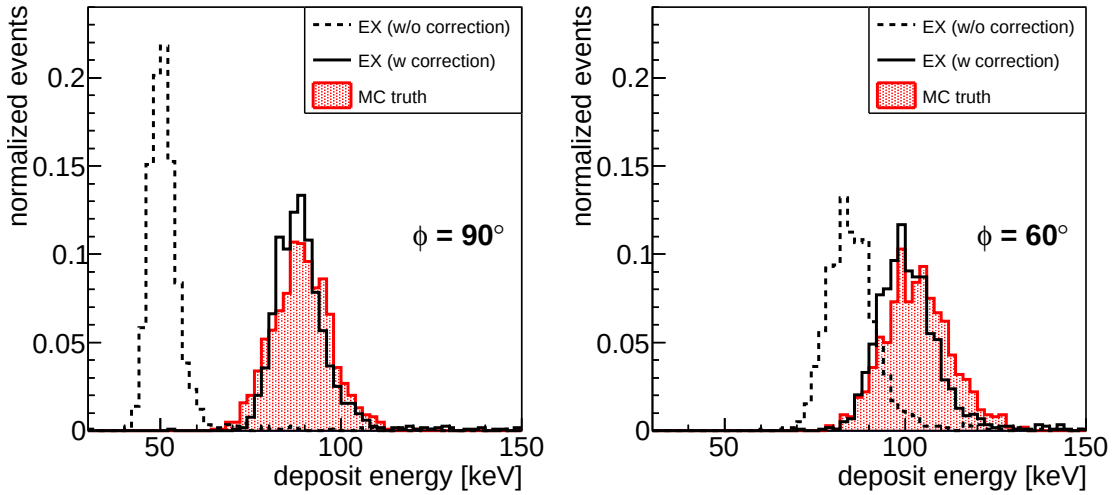

Figure C.4: Energy deposit distributions without and including the gain reduction correction [41]. The proton beam angles with respect to the anode wires were set at 90° (left) and 60° (right). The respective energy deposit distribution calculated by the Monte Carlo simulation is also drawn as a red histogram.

Acknowledgments

First of all, I would like to express my greatest appreciation to my supervising advisor Prof. Satoru Yamashita. He gave me the precious opportunity to join such an exciting and interesting experiment. Whenever I was at a standstill in my research, I always received accurate and essential advice from him. In addition, he actively gave me many opportunities to participate in various kinds of conferences, seminars, and schools. It greatly heightened my interest and motivation for physics. It was a wonderful and fruitful experience for me to be able to do the research with him for five years.

I am grateful to all the members of the neutron lifetime experiment. They always gave me lots of beneficial advice for my analysis, measurements, and presentations, which supported and encouraged me so much. Prof. Kenji Mishima devoted a considerable amount of his time to guide me in my research. We had many chances of discussing variety field of physics, and His extensive knowledge always taught me the fun to seek truths in physics. Prof. Masaaki Kitaguchi and Prof. Tamaki Yoshioka always gave me accurate advice in our weekly group meetings. I also would like to express my appreciation to all the other Neutron Optics and Fundamental Physics (NOP) members. It was a lot of fun to discuss neutron physics at conferences, seminars, and J-PARC dormitories. I hope all of them would enjoy their respective research and accomplish great achievements in the field.

I also would like to thank all the members of Yamashita laboratory. I especially had the immense support from Mr. Takahito Yamada and Dr. Sei Ieki, who are also collaborators of the neutron lifetime experiment. I spent a significant percentage of my research life with them, and they taught me all of the experiment, such as neutron physics, the data analysis, and the Monte Carlo simulation. I could not enjoyed my research so much without their kind and continuous support. In addition, I am deeply grateful to Mr. Yu Kato and Mr. Kazuki Fujii for improving ourselves through the experiment at the University of Tsukuba. Although it was not always an easy way due to a lot of troubles, it is definitely one of my best memories in my research life. Dr. Tomohiko Tanabe helped me a lot to finish this thesis by proofreading all the sentences in this thesis. Thanks to his appropriate and kind advice, I was able to keep my motivation up to writing the thesis. My gratitude also goes to all the other Yamashita laboratory members, Dr. Masakazu Kurata, Dr. Ryo Katayama, Dr. Nao Higashi, Mr. Harumichi Yokoyama, Mr. Takuaki Mori, Mr. Kento Kasuya, Mr. Shohei Fujikura, Mr. Takanori Mogi, and Mr. Shogo Kajiwara. Their earnest and energetic attitudes toward research are good stimuli for me, and they all gave me great advice for my research.

I would like to appreciate Sekiba laboratory members at the University of Tsukuba. We started collaboration experiment in 2016, and Dr. Daiichiro Sekiba provided us great opportunities

to conduct the experiment using the tandem accelerator. Furthermore, his advice based on his experience led me to the success of our collaborative experiment. I also enjoyed discussion and device development with other Sekiba laboratory members, Dr. Isao Harayama, Ms. Yumi Watahiki, Mr. Yuki Sugisawa, and Mr. Junichi Kikuda. It was great experience to have discussion with researchers in other fields.

I also enjoy my student life with all the ICEPP members. In particular, I would like to express my respectful gratitude to the ICEPP secretaries for supporting my research life. During my five years at ICEPP, I was able to focus on my research thank to their huge support.

I would like to thank Dr. Takuya Okudaira. I appreciate his feedback on my thesis despite his busy schedule. We enjoyed discussion every time participating in the international conferences, which always gave me a positive impact on my research.

I am also specially grateful to Mr. Tatsuya Kawaguchi and Mr. Yuichiro Tsuchiya for giving me a lot of technique related to the image recognition algorithm. I would not have finished the analysis without their persevering support.

In my research life, Dr. Jacqueline Yan gave me so many considerable support. She always provided useful comments and advice to my presentations as well as my thesis. In addition, she helped me to get the modules and the devices necessary for our experiment. We also enjoyed various kinds of meaningful seminars.

Finally, the deepest appreciation goes to my family for supporting me all my life.

Bibliography

[1] M. Pospelov and J. Pradler. Big Bang Nucleosynthesis as a Probe of New Physics. *Annual Review of Nuclear and Particle Science*, Vol. 60, pp. 539–568, 2010.

[2] A. Peimbert, M. Peimbert, and V. Luridiana. The primordial helium abundance and the number of neutrino families. *Revista Mexicana de Astronomia y Astrofisica*, Vol. 52, pp. 419–424, 2016.

[3] E. Aver, K. A. Olive, and E. D. Skillman. The effects of He I λ 10830 on helium abundance determinations. *Journal of Cosmology and Astroparticle Physics*, Vol. 2015, No. 07, p. 011, 2015.

[4] Y. I. Izotov, T. X. Thuan, and N. G. Guseva. A new determination of the primordial He abundance using the He I λ10830Å emission line: cosmological implications. *Monthly Notices of the Royal Astronomical Society*, Vol. 445, No. 1, pp. 778–793, 2014.

[5] PAR Ade $et\ al.$ Planck 2015 results: XIII. Cosmological parameters. *Astronomy and Astrophysics*, Vol. 594, pp. 1–63, 2016.

[6] M. Tanabashi $et\ al.$ (Particle Data Group). Review of particle physics. *Phys. Rev. D*, Vol. 98, p. 030001, Aug 2018.

[7] J. C. Hardy and I. S. Towner. Nuclear beta decays and CKM unitarity. In *13th Conference on the Intersections of Particle and Nuclear Physics (CIPANP 2018) Palm Springs, California, USA, May 29-June 3, 2018*, 2018.

[8] A. Czarnecki, W. J. Marciano, and A. Sirlin. Precision measurements and CKM unitarity. *Physical Review*, Vol. D70, p. 093006, 2004.

[9] J. Chadwick. The existence of a neutron. *Proceedings of the Royal Society of London A: Mathematical, Physical and Engineering Sciences*, Vol. 136, No. 830, pp. 692–708, 1932.

[10] S. Arzumanov $et\ al.$ A measurement of the neutron lifetime using the method of storage of ultracold neutrons and detection of inelastically up-scattered neutrons. *Physics Letters*, Vol. B745, pp. 79–89, 2015.

[11] J. S. Nico $et\ al.$ Measurement of the neutron lifetime by counting trapped protons in a cold neutron beam. *Physcal Review C*, Vol. 71, p. 055502, 2005.

[12] A. T. Yue *et al.* Improved Determination of the Neutron Lifetime. *Physical Review Letters*, Vol. 111, No. 22, p. 222501, 2013.

[13] R. Kossakowski *et al.* Neutron lifetime measurement with a helium-filled time projection chamber. *Nuclear Physics A*, Vol. 503, No. 2, pp. 473 – 500, 1989.

[14] J. Als-Nielsen and O. Dietrich. Slow Neutron Cross Sections for He^3, B, and Au. *Phys. Rev.*, Vol. 133, pp. B925–B929, Feb 1964.

[15] R. B. Firestone and V. S. Shirley. *Table of Isotopes*. Wiley-Interscience, 1.0 edition, March 1996.

[16] P. Grivot *et al.* A helium-filled time projection chamber for a neutron lifetime measurement. *Nuclear Instruments and Methods in Physics Research Section B: Beam Interactions with Materials and Atoms*, Vol. 34, No. 1, pp. 127 – 134, 1988.

[17] J-PARC official website. `http://j-parc.jp/`.

[18] T. Ino *et al.* Measurement of the neutron beam polarization of BL05/NOP beamline at J-PARC. *Physica B: Condensed Matter*, Vol. 406, No. 12, pp. 2424 – 2428, 2011. Proceedings of the 8th International Workshop on Polarised Neutrons for Condensed Matter Investigation.

[19] K. Mishima. J-PARC 中性子基礎物理ビームライン（BL05/NOP）. *Neutron network news (Hamon)*, Vol. 25, No. 2, pp. 156–160, 2015.

[20] Y. Arimoto *et al.* Development of time projection chamber for precise neutron lifetime measurement using pulsed cold neutron beams. *Nuclear Instruments and Methods in Physics Research Section A: Accelerators, Spectrometers, Detectors and Associated Equipment*, Vol. 799, pp. 187 – 196, 2015.

[21] H. Otono. *New detector system for the precise neutron lifetime measurement using pulsed cold neutron beams*. Ph.D. dissertation, The University of Tokyo, December 2011.

[22] T. Ino *et al.* Precision neutron flux measurement with a neutron beam monitor. *Journal of Physics: Conference Series*, Vol. 528, No. 1, p. 012039, 2014.

[23] Garfield official website. `http://garfield.web.cern.ch/garfield`.

[24] A. R. Siddiq and A. R. Kennedy. Porous poly-ether ether ketone (PEEK) manufactured by a novel powder route using near-spherical salt bead porogens: Characterisation and mechanical properties. *Materials Science and Engineering: C*, Vol. 47, pp. 180 – 188, 2015.

[25] Y. Lee. *Physical properties of poly(ether ether ketone)*. Ph.D. dissertation, University of Massachusetts Amherst, 1988.

[26] Neutron scattering lengths and cross sections. `http://www.ncnr.nist.gov/resources/n-lengths/`.

[27] Magboltz official website. `http://magboltz.web.cern.ch/magboltz/`.

[28] Y. Igarashi $et\ al.$ A common data acquisition system for high-intensity beam experiments. *Nuclear Science, IEEE Transactions*, Vol. 52, No. 6, 2 2005.

[29] Japan Radioisotope Association. アイトソープ手帳 11 版. Maruzen Publishing, 2012.

[30] H. Sumino, K. Nagao, and K. Notsuji. Highly sensitive and precise measurement of helium isotopes using a mass spectrometer with double collector system. *Journal of the Mass Spectrometry Society of Japan*, Vol. 49, No. 2, pp. 61–68, 2001.

[31] S. Ieki. *Measurement of the Neutron Lifetime by Counting the Beta Decay at J-PARC*. Ph.D. dissertation, The University of Tokyo, December 2017.

[32] S. Agostinelli $et\ al.$ Geant4—a simulation toolkit. *Nuclear Instruments and Methods in Physics Research Section A: Accelerators, Spectrometers, Detectors and Associated Equipment*, Vol. 506, No. 3, pp. 250 – 303, 2003.

[33] R. Grossman, D. Hanley, and Xiao Qin. Caching and migration for multilevel persistent object stores. In *Proceedings of IEEE 14th Symposium on Mass Storage Systems*, pp. 127–135, Sept 1995.

[34] J. Allison $et\ al.$ Recent developments in Geant4. *Nuclear Instruments and Methods in Physics Research Section A: Accelerators, Spectrometers, Detectors and Associated Equipment*, Vol. 835, pp. 186 – 225, 2016.

[35] K. Hirota $et\ al.$ Development of a neutron detector based on a position-sensitive photomultiplier. *Physical Chemistry Chemical Physics*, Vol. 7, pp. 1836–1838, 2005.

[36] N. Z. Alcock and D. G. Hurst. Neutron diffraction by the gases $\mathrm{N_2}$, $\mathrm{CF_4}$, and $\mathrm{CH_4}$. *Physical Review*, Vol. 83, pp. 1100–1105, Sep 1951.

[37] N. Z. Alcock and D. G. Hurst. Neutron diffraction by gases. *Physical Review*, Vol. 75, pp. 1609–1610, May 1949.

[38] Prompt gamma-ray neutron activation analysis. `https://www-nds.iaea.org/pgaa/pgaa7/index.html`.

[39] Phits official website. `https://phits.jaea.go.jp/indexj.html`.

[40] Nuclear data evaluation project. `http://www.tunl.duke.edu/nucldata/`.

[41] N. Nagakura $et\ al.$ Experimental verification of a gain reduction model for the space charge effect in a wire chamber. *Progress of Theoretical and Experimental Physics*, Vol. 2018, No. 1, p. 013C01, 2018.

[42] S. Ramo. Currents induced by electron motion. *Proceedings of the Institute of Radio Engineers*, Vol. 27, No. 9, pp. 584–585, Sept 1939.

[43] ANSYS official website. `https://www.ansys.jp/index.html`.

[44] G. Bradski. The OpenCV Library. *Dr. Dobb's Journal of Software Tools*, 2000.

[45] J. Matsuda *et al*. The 3He/4He ratio of the new internal He standard of Japan (HESJ). *Geochemical journal GJ*, Vol. 36, pp. 191–195, 01 2002.

[46] K. Mishima *et al*. Accurate Determination of the Absolute 3He/4He Ratio of a Synthesized Helium Standard Gas (Helium Standard of Japan, HESJ): Toward Revision of the Atmospheric 3He/4He Ratio. *Geochemistry, Geophysics, Geosystems*, Vol. 19, No. 10, pp. 3995–4005, 2018.

[47] W. Blum, W. Riegler, and L. Rolandi. *Particle Detection with Drift Chambers*. Springer, 2008.

[48] E. Waibel and B. Grosswendt. Degradation of low-energy electrons in carbon dioxide: energy loss and ionization. *Nuclear Instruments and Methods in Physics Research Section B*, Vol. 53, No. 3, pp. 239–250, 1991.

[49] G. Willems, W. Y. Baek, and B. Grosswendt. Energy dependence of w values of protons in water. *Radiation Protection Dosimetry*, Vol. 99, No. 1-4, pp. 347–350, 2002.

[50] Japan Ship and Boat Manufacturers' Association. 通信教育造船科講座テキスト「船殻設計」学習指導書. 2000.

[51] D. Cook. The second virial coefficient of carbon dioxide at low temperatures. *Canadian Journal of Chemistry*, Vol. 35, No. 3, pp. 268–275, 1957.

[52] G. S. Kell, G. E. McLaurin, and E. Whalley. Second virial coefficient of helium from 0 to 500°C by the two-temperature gas-expansion method. *The Journal of Chemical Physics*, Vol. 68, No. 5, pp. 2199–2205, 1978.

[53] D. Sekiba *et al*. Installation of high-resolution ERDA in UTTAC at the University of Tsukuba: Determination of the energy resolution and the detection limit for hydrogen. *Nuclear Instruments and Methods in Physics Research Section B: Beam Interactions with Materials and Atoms*, Vol. 401, pp. 29 – 32, 2017.